Thermal Modeling and Characterization of Nanoscale Metallic Interconnects

A Thesis
Presented to
The Academic Faculty

by

Siva P. Gurrum

In Partial Fulfillment
of the Requirements for the Degree
Doctor of Philosophy

G. W. Woodruff School of Mechanical Engineering
Georgia Institute of Technology
May 2006

Thermal Modeling and Characterization of Nanoscale Metallic Interconnects

Approved by:

Dr. Yogendra K. Joshi, Co-Advisor
G. W. Woodruff School of Mechanical
Engineering
Georgia Institute of Technology

Dr. William P. King, Co-Advisor
G. W. Woodruff School of Mechanical
Engineering
Georgia Institute of Technology

Dr. Peter J. Hesketh
G. W. Woodruff School of Mechanical
Engineering
Georgia Institute of Technology

Dr. Suresh K. Sitaraman
G. W. Woodruff School of Mechanical
Engineering
Georgia Institute of Technology

Dr. James D. Meindl
School of Electrical and Computer En-
gineering
Georgia Institute of Technology

Dr. Alexei Marchenkov
School of Physics
Georgia Institute of Technology

Date Approved: 21 December 2005

ACKNOWLEDGEMENTS

I would like to thank my committee members Drs. Yogendra Joshi, William King, Peter Hesketh, Suresh Sitaraman, James Meindl, and Alexei Marchenkov for their valuable feedback on my work. I really enjoyed working with my co-advisors Dr. Joshi and Dr. King, who have always set high goals for me and continuously encouraged me to achieve them. I would also like to extend my sincere thanks to Dr. Koneru Ramakrishna from Freescale Semiconductor Inc., who has mentored my work throughout my stay at Georgia Tech.

I couldn't have finished my work without the help of my lab members, in particular, Tanya Wright, Brent Nelson, Adam Christensen, and Xiaojin Wei. I have thoroughly enjoyed my stay at Georgia Tech with other lab members.

I would like to thank my parents and sister who made so many sacrifices to help me achieve my goals. Without their support I could not dream to reach this juncture in my life. I would also like to thank my dear friends Sasi and Reddy for their personal support.

TABLE OF CONTENTS

LIST OF TABLES

LIST OF FIGURES

xi

SUMMARY

Temperature rise due to Joule heating of on-chip interconnects can severely affect performance and reliability of next generation microprocessors. Thermal predictions become difficult due to number of features on the order of a billion and the impact of electron size effects on electrical and thermal transport. It is thus necessary to develop efficient numerical approaches and accurate metal and dielectric thermal characterization techniques. In this research, analytical, numerical, and experimental techniques were developed to enable accurate and efficient predictions of temperature rise in an on-chip interconnect stack.

A finite element based compact thermal modeling methodology was developed to obtain temperature rise with lesser number of elements and acceptable accuracy (5 - 10 %). In this technique, the temperature drop across the interconnect cross-section was ignored. This approach was applied to two-dimensional uniformly spaced interconnects, three-dimensional interconnects terminated with vias, and a real world structure consisting of a long serpentine chain of about 500 interconnects and vias. In all the cases, the compact model performed better than standard finite elements. In some cases, the performance was improved by an order of magnitude. The compact model predictions agreed closely with experimentally measured temperature rise of the serpentine chain.

A numerical solution was developed for electron transport through complex interconnect structures based on the Boltzmann Transport Equation (BTE). This deterministic technique, based on the path integral solution of BTE within the relaxation time approximation, free electron model, and linear response, was applied to a constriction in a finite size thin metallic film. Effective conductance dropped over the

bulk value even with specular surface scattering for different constriction sizes and aspect ratios. An extension of the constriction results for a short metallic bridge was discussed. These simulations can provide effective resistances between two locations, and can then be used in a macroscale framework.

An Atomic Force Microscope (AFM) was used to develop a new technique to measure thermal conductivity of thin metallic films in the size effect regime. This technique uses Scanning Joule Expansion Microscopy (SJEM) to measure temperature expansion amplitude on the surface of a constriction in a thin film. It does not require complex microfabrication to obtain free-standing structures, and thus preserves the original metal interface and scattering characteristics. Using extensive thermal conduction modeling in the frequency space, thermal conductivity values for two film thicknesses were extracted from SJEM measurements. The thermal conductivities of 43 nm and 131 nm gold films were found to be 82 W/mK and 162 W/mK respectively at the smallest frequency investigated. These measurements were close to Wiedemann-Franz Law predictions and are significantly smaller than the bulk value of 318 W/mK due to electron size effects. The technique can potentially be applied to interconnects in the sub-100 nm regime.

A semi-analytical solution for the 3ω method was derived to account for thermal conduction within the metallic heater. Existing uniform heat flux approximation between the metal heater and substrate was replaced by a more realistic uniform heat generation condition within the metal heater. Although this correction does not affect thermal conductivity measurements in the original 3ω method, it is shown that significant errors can result when it is applied for anisotropy measurements. For small thermal conductivity films, the error in the anisotropy ratio can be as high as 50 %.

CHAPTER I

INTRODUCTION

The microelectronics industry is pursuing several architectural advances in order to sustain steady improvements in the performance of microprocessors. Most notably, copper has replaced aluminum for on-chip interconnects, and novel low dielectric constant materials (low-k materials) are being introduced to replace traditional inter layer dielectric (ILD) material TEOS (TetraEthylOrthoSilicate) [88]. Typical low-k dielectrics have up to an order of magnitude lower thermal conductivity than TEOS. According to the International Technology Roadmap for Semiconductors (ITRS 2004 [37]), electrical design requirements dictate higher current densities in the interconnects of next generation technology nodes. In addition, the number of interconnect layers is expected to increase in future technologies. These trends result in higher interconnect temperatures in the current and future technology nodes. Figure 1.1 shows a schematic cross-section of an interconnect stack in microprocessors based on [37]. Multi-stack interconnect architecture is characterized by wide range of length scales (from 10^{-9} m to 10^{-2} m) and significant material inhomogeneity (thermal conductivity variation from 0.1 W/mK to 400 W/mK). Different metal levels are connected through vias that provide electrical connections.

Traditionally, interconnect temperature was crucial in predicting median time to failure ($MTTF$) due to electromigration (Ho and Kwok [33]). $MTTF$ is commonly given by Black's equation [4]

$$MTTF = \frac{Ae^{E_a/kT}}{j^n} \tag{1.1}$$

where A is a constant, E_a is the activation energy, T is the temperature, k is the
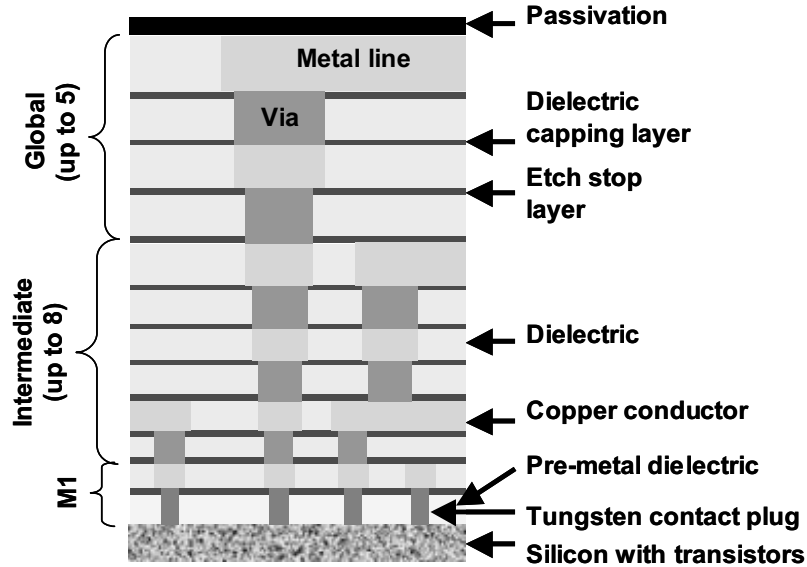
Figure 1.1: A schematic of interconnect stack with metal lines and vias adapted from [37].

Boltzmann constant, j is the current density, and n is the current exponent. Common practice is to use maximum junction temperature (temperature of the front-end transistors) for interconnect temperature in Black's equation to project field life from accelerated tests. Such a practice can lead to non-conservative field life estimates, as the interconnect temperature is higher than transistor temperature due to self-heating effects. Joule heating in the earlier generations resulted in only a small increment in interconnect temperature above the transistor/active device temperature. However, in the current and future technologies, temperature rise can be significant, and interconnect thermal issues have received considerable attention in recent times (Shen [79], Banerjee et al. [5], and Streiter et al. [85]). Due to increased temperatures in the interconnect stack, temperature dependence of clock signal delay (Kapur et al. [43]) and clock skew (Ajami et al. [2]) have also received considerable attention. The electrical resistivity of the metal line and electrical capacitance due to the surrounding dielectric cause a delay in the signal propagation through the circuit. Signal delay is directly proportional to interconnect resistance and is affected by the temperature

dependence of metal's electrical resistivity.

An accurate prediction of both performance (signal delay and clock skew) and reliability (MTTF due to electromigration) requires a detailed determination of temperature profile in the interconnect stack of a chip under system operating conditions. As interconnect dimensions decrease with each technology node, the effect of electron scattering with the walls of the interconnect plays an important role in electrical and thermal conduction. Figure 1.2 shows the predicted reduction in effective conductivity of interconnects if the walls are assumed to be perfectly diffuse (see Chapter 2 for references and description). These predictions are based on Fuchs-Sondheimer model for electron size effect ([27] and [82]). This plot shows that the conductivity may be reduced to half the bulk value in a decade. Similar reductions are expected for thermal conductivity, since in metals, both electrical and thermal conduction are dominated by electrons. It is thus important to also include electron size effects in predicting temperature rise.

The ITRS roadmap predicts that the number of transistors in a high performance microprocessor will exceed a billion in year 2007. The number of interconnects connecting these active devices will also increase in a similar manner. Predicting temperature rise within the interconnect stack is thus a formidable task. Figure 1.3 illustrates a big picture of various sub-tasks that may be necessary to enable accurate and efficient temperature rise predictions. This task involves three main components: macroscale modeling, nanoscale modeling, and electrical and thermal characterization, and various inter-relations between these sub-tasks. Macroscale modeling involves using analytical or numerical techniques, assuming either that continuum theory holds, or effective properties can be defined. Reduced microscopic models (either through theory or experiments) and thermal/electrical properties are necessary to perform such simulations. Nanoscale modeling involves simulating detailed electron and phonon transport through small structures where size effects are important.
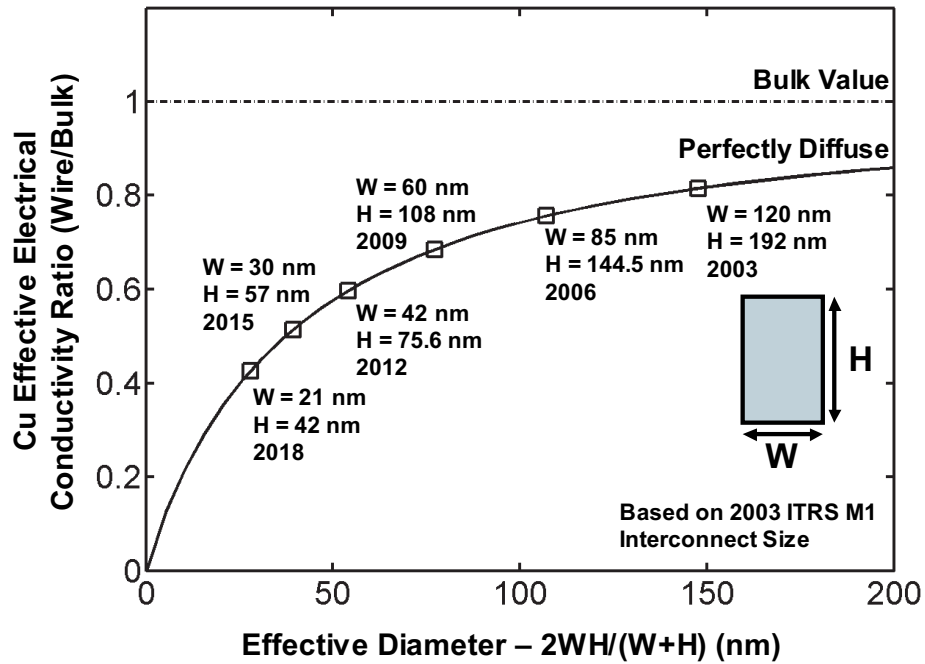
Figure 1.2: Electrical conductivity reduction predictions using Fuchs-Sondheimer model for size effect and using dimensions from ITRS 2004 [37].

Some techniques, such as ab-initio molecular dynamics, can predict physical properties by merely specifying the atomic composition. Other simulations may require some macroscopic properties. Nanoscale simulations can result in reduced models to be later used in macroscale modeling. In some instances, macroscale predictions are necessary to simulate far-field conditions in a nanoscale simulation. A more comprehensive approach is a simulation that simultaneously solves for all length scales. Such a multiscale modeling approach has received considerable attention recently [73]. It is also important to supplement nanoscale and macroscale modeling with experimental characterization. These measurements can validate the simulations and also provide valuable input to the simulations in the form of thermal and electrical properties, and empirical models. Many nanoscale phenomena are yet to be understood, and high resolution characterization is essential to make any progress towards predictive models.

Interconnect Thermal Modeling and Characterization
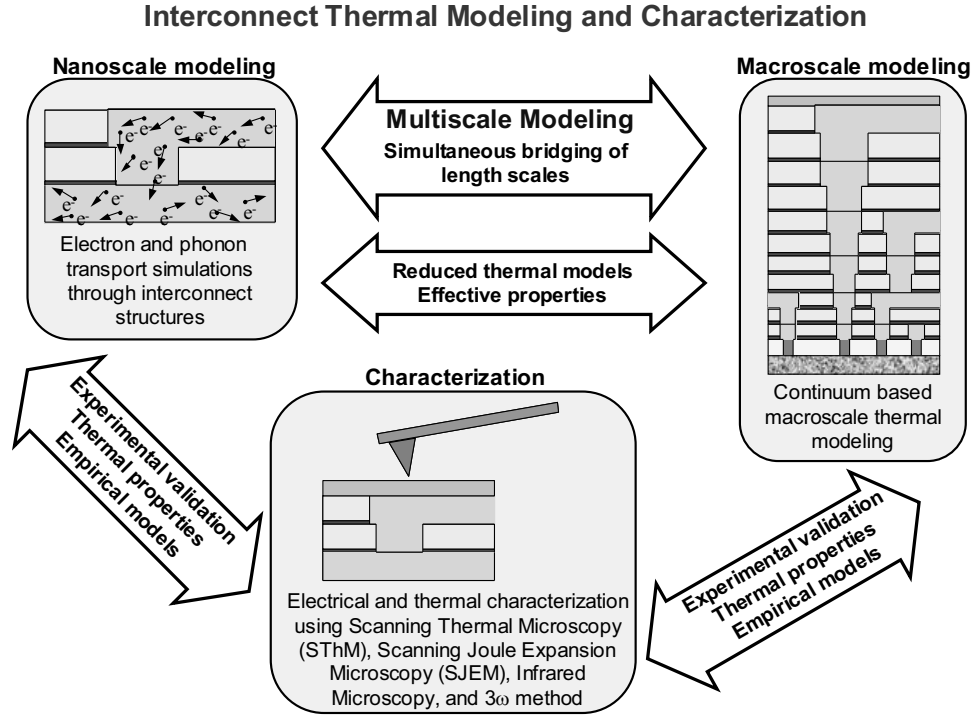
Figure 1.3: A big picture of various tasks that enable accurate interconnect thermal modeling and characterization including physics from the nanoscale to the macroscale.

Existing numerical techniques based on finite difference and finite element methods can be used for temperature prediction at the macroscale, assuming that the continuum theory holds. But the computational times are long even for a unit cell (micro-models). Any simpler approaches, mostly analytical, are restricted to simpler structures and cannot capture thermal interactions. It is thus essential to develop approaches that require less computational time and capture thermal interactions. Simulations of electron transport can be performed using the Monte Carlo technique, but such approaches are highly expensive for a complex interconnect structure. Simpler approaches that include the essential physics should be developed.

This work develops novel analytical, numerical, and experimental techniques, to facilitate accurate and efficient predictions of temperature rise in an on-chip interconnect stack. The unique contributions of this research are as follows.

- A Finite Element Method (FEM) based compact approach to simulate continuum based thermal transport that requires lesser number of finite elements has been developed.

- A path integral based approach to simulate electron transport through complex interconnect structures that provides effective conductance and heat generation variation has been implemented.

- A novel technique to extract thermal conductivity of sub-100 nm interconnects using Scanning Joule Expansion Microscopy (SJEM) that preserves original interface scattering characteristics has been developed.

- A new semi-analytical solution for the 3ω method including the effect of thermal conduction in the metallic heater that improves anisotropic dielectric thermal conductivity measurements has been obtained.

A brief description of these contributions is given in the following paragraphs. Chapter 2 provides a background on earlier Joule heating studies, electron transport theory and size effect models, high resolution thermal characterization, and existing approaches to measure in-plane thermal conductivity of metallic films.

The compact modeling approach described in Chapter 3 uses traditional finite element technique with the approximation that the temperature drop across an interconnect cross-section is negligible. Temperature drop along the length is appreciable and is retained, as it plays an important role in lateral heat conduction. The compact numerical solution methodology proposed in this work takes advantage of large metal-to-dielectric thermal conductivity ratio. The finite elements investigated here contain both metallic and dielectric regions in the same element. Such a compact thermal modeling approach reduces the number of nodes where temperature needs to be computed. Compact thermal models outside the chip, or at the package level have been studied in several investigations (Bar-Cohen et al. [6], Rosten et al. [72],

Boyalakuntla and Murthy [13], Adams et al. [1], and Sabry [74]). Most of the investigations have been directed towards obtaining an equivalent thermal resistance network. In this chapter, simple structures are first studied to evaluate the performance of the compact model. Error estimates are provided to guide mesh generation. Then, Joule heating effects in a commonly used 500-link test structure, consisting of two levels of metal lines (M1 and M2) connected by vias (V1) is studied using compact models, detailed finite element calculations and experimental measurements. Average temperature rise of this structure was measured by resistance thermometry and the results are compared with the predictions of compact model.

Chapter 4 describes a path integral based numerical approach to simulate electron transport through complex structures. This approach solves the Boltzmann Transport Equation (BTE) for free electrons, within the relaxation time approximation, and under linear response. Only electrons at the Fermi level are considered in the technique. This approach does not require a separate solution of Poisson's equation. Using this technique, reduction in conductance across a constriction in a thin film is predicted. A short metallic bridge is also considered, and it is shown that a simple series addition of independent constriction and bridge resistances can accurately predict overall conductance of the structure. The simulations also provide detailed variation of heat generation in the structures.

A novel approach to extract thermal conductivity of thin metallic films is proposed in Chapter 5. This technique uses Atomic Force Microscope (AFM) based Scanning Joule Expansion Microscopy (SJEM) developed by Varesi and Majumdar [90]. Through extensive SJEM characterization of a constriction, and numerical simulations in the complex domain, thermal conductivity of thin films in the size effect regime is measured. These measurements are close to the expected values.

In Chapter 6, a new semi-analytical solution to the 3ω method is derived and investigated. The 3ω method is a powerful technique to measure thermal properties

of films [15]. The present solution includes heat conduction within the metallic heater, which was ignored in earlier solutions. It is shown that this effect is significant in anisotropy measurements. Finally, Chapter 7 concludes and provides future directions to this research.

CHAPTER II

BACKGROUND AND LITERATURE SURVEY

In this chapter, relevant background and previous investigations are presented. Interconnect Joule heating studies, electron transport simulation techniques, in-plane metal thermal conductivity measurement techniques, high resolution temperature measurement techniques, and the 3ω method are reviewed. Electron transport theory is explained in considerable detail to facilitate subsequent explanations of approximations used in the present work.

2.1 Interconnect Joule heating studies

Several studies dealt with interconnect Joule heating at various levels of approximation. A set of long uniformly spaced interconnects is often approximated as a two-dimensional thermal spreading problem of an isothermal heat source shown in Figure 2.1. Bilotti [8] obtained analytical expressions for the heat spreading factor using double Schwarz-Christoffel conformational transformation. Schafft [76] and Chiang et al. [20] considered finite length interconnects using a fin type equation. Although heat conduction along the interconnect was considered, a length-wise constant two-dimensional spreading resistance through the dielectric was assumed. Such a fin equation can be solved for any specified temperature conditions near the ends. Chiang et al. [20] also considered multi-level interconnects by simply adding average contributions to temperature rise from each interconnect level. Teng et al. [87] developed an electromigration reliability predictive tool that accounts for Joule heating effects in active devices and the interconnects. The temperature profile on the substrate was calculated by a finite difference method after ignoring interconnect Joule
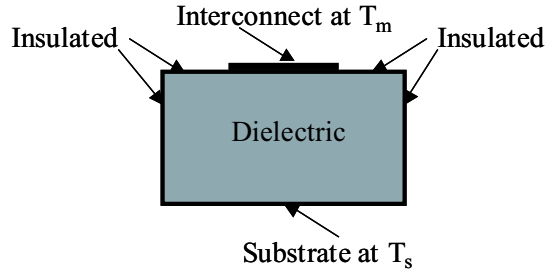
Figure 2.1: A common idealization of long uniformly spaced interconnects.

heating. This temperature profile was later used to determine the boundary conditions for interconnect heating simulation. Hunter [35] analyzed the self-consistent problem of determining allowed current density using Bilotti's expressions. Interconnect heating and electromigration were included in the analysis. Chen et al. [18] computed interconnect temperature rise using a commercially available finite element solver for more realistic structures. Expressions for temperature rise were provided for some of the structures using a combination of analytical and numerically fitted solutions. Using the thermal modeling methodology described in [18], Casu et al. [17] performed electro-thermal simulations and optimization of clock networks. Their study included electromigration and clock signal delay through the interconnect network. Stan et al. [83] and Huang et al. [34] developed a compact thermal model that included details at the microprocessor architecture level. Importance of temperature field at all stages of an IC design was noted, although interconnect temperature rise was considered only in an average sense.

2.2 Theory of electron transport in metals

Metals are characterized by large electron densities and are good conductors of heat and electricity. Due to an electric potential or a temperature gradient, electron currents are setup inside the metal, which lead to macroscopic electric and thermal currents. This flow of electrons is impeded at normal temperatures by the underlying

lattice of atoms. Atomic vibrations (a quantum of lattice vibration is termed *phonon*) scatter electrons and result in finite electrical and thermal conductivity. Other scattering mechanisms include those due to impurities, vacancies, and grain boundaries (See Ashcroft and Mermin [4] for an excellent treatment of condensed matter physics).

A general description of electron dynamics begins by defining a distribution function $f(\mathbf{k}, \mathbf{r}, t)$. The distribution function denotes the probability that a state specified by wavevector $\mathbf{k}$ is occupied at position $\mathbf{r}$ at time t. Strictly speaking, an electron state is specified by the wavevector as well as spin. The spin can be *up* or *down*. This is unimportant for the properties considered in this work. A factor of 2 that arises due to electron spin is included in the averaging over the distribution function. Once the distribution function is known, any property can be calculated by performing a weighted average over suitable variables. For example, the electron density $n(\mathbf{r}, \mathbf{t})$, electric current density $\mathbf{j}_e(\mathbf{r}, \mathbf{t})$, and heat flux $\mathbf{q}_e''(\mathbf{r}, t)$ are given by

$$n(\mathbf{r}, t) = \frac{1}{4\pi^3} \int d\mathbf{k} f(\mathbf{k}, \mathbf{r}, t) \tag{2.1}$$

$$\mathbf{j}_e(\mathbf{r}, t) = \frac{q}{4\pi^3} \int d\mathbf{k} \mathbf{v_k} f(\mathbf{k}, \mathbf{r}, t) \tag{2.2}$$

$$\mathbf{q}_e''(\mathbf{r}, t) = \frac{1}{4\pi^3} \int d\mathbf{k} \mathbf{v_k} \varepsilon_\mathbf{k} f(\mathbf{k}, \mathbf{r}, t) \tag{2.3}$$

where $\mathbf{v_k}$ is the velocity of electron, $\varepsilon_\mathbf{k}$ is the energy of the electron, q is the electron charge ($q = -e = -1.602$ x 10^{-19} C), $d\mathbf{k}$ is the differential volume element in $\mathbf{k}$-space ($dk_x dk_y dk_z$), and the integration is over entire $\mathbf{k}$-space. The subscript $'\mathbf{k}'$ on velocity and energy indicates that they are functions of the wavevector. This dependence will sometimes be denoted by $\mathbf{v}(\mathbf{k})$ and $\varepsilon(\mathbf{k})$. In these expressions, the factor 2 due to electron spin is included. At equilibrium, the distribution function is given by the Fermi-Dirac distribution

$$f_o(\varepsilon_\mathbf{k}) = \frac{1}{1 + \exp[(\varepsilon_\mathbf{k} - \mu)/k_B T]} \tag{2.4}$$

where μ is the chemical potential, k_B is the Boltzmann constant, and T is the temperature. This function shown in Figure 2.2 is quite different from Maxwell-Boltzmann

11
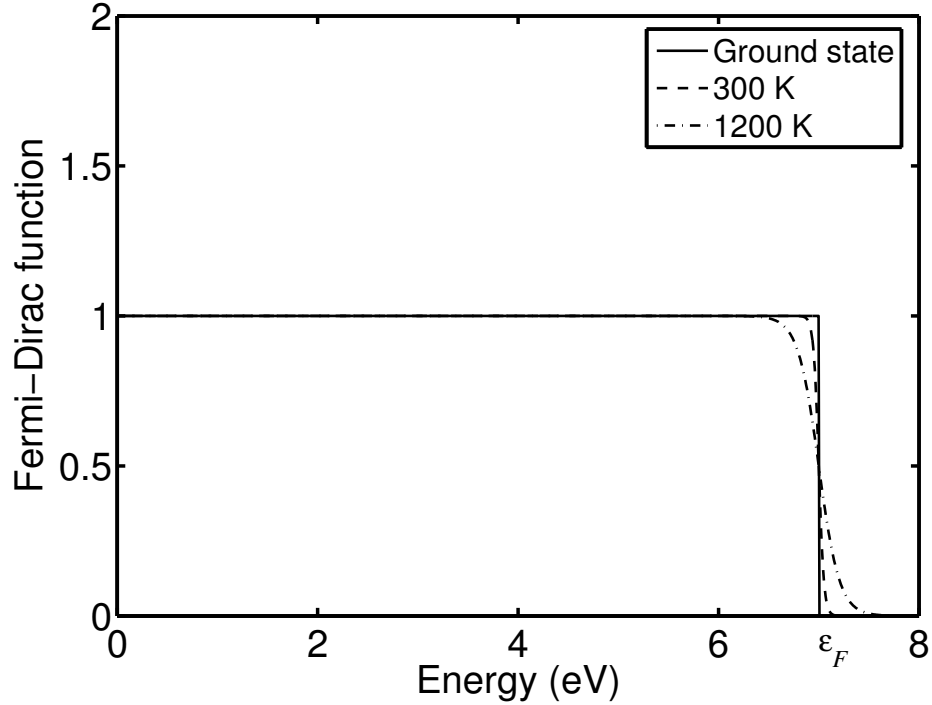
Figure 2.2: Evolution of Fermi-Dirac distribution function for copper as temperature increases. At equilibrium, all the states until the Fermi level ε_F are filled. As temperature increases, only the energy states in the range $\approx k_B T$ about the Fermi level are altered due to Pauli principle. It is electrons in these states that are important for conduction

distribution function, due to Pauli's exclusion principle. According to the Pauli principle, no two electrons can be in the same state (a state is characterized by the wavevector and spin). At the ground state ($T = 0$ K), all electrons up to the Fermi level ε_F are filled ($\mu = \varepsilon_F$ at $T = 0$ K). As temperature increases, electrons gain energy, but lower energy electrons cannot fill adjacent states as they are already occupied. Only electrons in the range $\approx k_B T$ below the Fermi level spill over to higher energies. For $k_B T << \varepsilon_F$ the electron gas is termed *degenerate* and the *degeneracy temperature* T_F equals ε_F / k_B. The effect of Pauli principle is similar when external fields interact with the electrons. Thus, in a degenerate electron gas, only electrons near the Fermi level play a role in electrical and thermal transport.

Nothing has yet been mentioned about the relationship between electron energy,

velocity and wavevector. The *Bloch theory of energy bands* solves for the quantum-mechanical energy states. In this model, electrons are assumed to be influenced by a periodic potential due to the underlying lattice with atomic cores (or ions) frozen at their equilibrium positions. Solution of the quantum-mechanical Schrodinger equation leads to energy bands $\varepsilon_n(\mathbf{k})$ of possible electron states indexed by $'n'$. The term bands is used to signify that there are forbidden energy levels in between them. The mean velocity of an electron with wavevector $\mathbf{k}$ in energy band n is given by

$$\mathbf{v}_n(\mathbf{k}) = \frac{1}{\hbar}\frac{\partial \varepsilon_n(\mathbf{k})}{\partial \mathbf{k}} \tag{2.5}$$

It turns out that within such a potential model, electrons travel unimpeded, and thus provide no explanation for the observed finite electrical or thermal conductivity. As mentioned earlier, the frozen lattice model is incorrect at normal temperatures and electrons are scattered due to phonons and other collision mechanisms.

External forces, such as electric and magnetic fields, and temperature gradient, lead to a non-equilibrium distribution function. In a *semiclassical* treatment of electron motion (See [4] for the details on assumptions involved), the following equations are valid in the absence of an external magnetic field.

$$\frac{d\mathbf{r}}{dt} = \mathbf{v}_n(\mathbf{k}) = \frac{1}{\hbar}\frac{\partial \varepsilon_n(\mathbf{k})}{\partial \mathbf{k}} \ ; \quad \hbar\frac{d\mathbf{k}}{dt} = q\mathbf{E}(\mathbf{r}) \tag{2.6}$$

where $\hbar = h/2\pi$ ($h = 6.626 \times 10^{-34}$ Js is the Planck's constant) and $\mathbf{E}(\mathbf{r})$ is the *external* electric field. It is semiclassical since only the periodic potential of ions (at the atomic scale) is treated quantum mechanically. External fields are treated classically. This assumption is justified as long as the external fields do not vary appreciably over atomic distances. The second equation above reminds of Newton's Second Law if $\hbar\mathbf{k}$ is interpreted as electron momentum ($\hbar\mathbf{k}$ is termed *crystal momentum*). The above expressions are valid only between collisions. Collisions are assumed to be instantaneous and change the electron state abruptly.

The general evolution of $f_n(\mathbf{k}, \mathbf{r}, t)$ is governed by the Boltzmann Transport Equation (BTE) which simply is a conservation law ($f_n(\mathbf{k}, \mathbf{r}, t)$ is now the probability that a state specified by wavevector $\mathbf{k}$ is occupied at position $\mathbf{r}$ in band n at time t). The total time derivative of $f_n(\mathbf{k}, \mathbf{r}, t)$ should be zero in the absence of any collisions. Collisions can cause an abrupt change in the wavevector or band. Thus the following equation can be written down (suppressing the arguments momentarily).

$$\frac{df_n}{dt} = \frac{\partial f_n}{\partial t} + \frac{d\mathbf{r}}{dt} \cdot \frac{\partial f_n}{\partial \mathbf{r}} + \frac{d\mathbf{k}}{dt} \cdot \frac{\partial f_n}{\partial \mathbf{k}} = \left(\frac{\partial f_n}{\partial t}\right)_{coll} \tag{2.7}$$

where the right hand side term denotes changes in the distribution function due to collisions. Using Eq. 2.6 one obtains the BTE:

$$\frac{\partial f_n(\mathbf{k}, \mathbf{r}, t)}{\partial t} + \mathbf{v}_n(\mathbf{k}) \cdot \frac{\partial f_n(\mathbf{k}, \mathbf{r}, t)}{\partial \mathbf{r}} + \frac{q\mathbf{E}(\mathbf{r})}{\hbar} \cdot \frac{\partial f_n(\mathbf{k}, \mathbf{r}, t)}{\partial \mathbf{k}} = \left(\frac{\partial f_n(\mathbf{k}, \mathbf{r}, t)}{\partial t}\right)_{coll} \tag{2.8}$$

There are seven independent dimensions in the above equation and the collision term is quite complicated for a general case. In the following section, a much simpler model is described that explains many of the transport properties in metals quite well.

2.2.1 Free electron model and relaxation time approximation

In the early 1900's, *free electron model* was proposed to account for transport properties in metals. Historically, this model precedes the Bloch theory of energy bands outlined in the previous section. In this model, electrons are assumed to travel freely (not influenced by any periodic potential) between scattering events. Accordingly, there is just one single continuous band of energy states (the band index n can then be omitted). The electron energy is purely kinetic and the following explicit relations are valid.

$$\frac{d\mathbf{r}}{dt} = \mathbf{v}_{\mathbf{k}} = \frac{\hbar \mathbf{k}}{m} \; ; \quad \varepsilon_{\mathbf{k}} = \frac{1}{2}mv_{\mathbf{k}}^2 = \frac{\hbar^2 k^2}{2m} \tag{2.9}$$

With these relations, Fermi velocity v_F and Fermi wavevector k_F are defined by

$$\varepsilon_F = \frac{1}{2}mv_F^2 = \frac{\hbar^2 k_F^2}{2m} \tag{2.10}$$

14

In the three-dimensional **k**-space, *Fermi sphere* is defined by a spherical region of radius k_F centered at the origin. The equilibrium number density n_o can now be easily evaluated from Eq. 2.1 using the above relations and the fact that at $T = 0$ K, $f_o = 1$ inside the Fermi sphere and zero outside (due to electron number conservation, the number density is also same at nonzero temperatures if thermal expansion is ignored):

$$n_o = \frac{k_F^3}{3\pi^2} \tag{2.11}$$

In the *Relaxation Time Approximation* (RTA), scattering events are phenomenologically described by a *relaxation time* τ. This relaxation time represents the average time between collisions. There is no reason for τ to be a constant. Nevertheless, a constant τ explains electrical and thermal transport in simple metals satisfactorily. The stationary BTE for free electrons within the RTA takes the following form.

$$\mathbf{v_k} \cdot \frac{\partial f(\mathbf{k}, \mathbf{r})}{\partial \mathbf{r}} + \frac{q\mathbf{E}(\mathbf{r})}{\hbar} \cdot \frac{\partial f(\mathbf{k}, \mathbf{r})}{\partial \mathbf{k}} = -\frac{f(\mathbf{k}, \mathbf{r}) - f_{le}(\mathbf{k}, \mathbf{r})}{\tau} \tag{2.12}$$

$$\frac{1}{4\pi^3} \int d\mathbf{k} \left[f(\mathbf{k}, \mathbf{r}) - f_{le}(\mathbf{k}, \mathbf{r}) \right] = 0 \tag{2.13}$$

where the local equilibrium distribution function $f_{le}(\mathbf{k}, \mathbf{r})$ is the Fermi-Dirac distribution in Eq. 2.4 with a spatially varying chemical potential $\mu(\mathbf{r})$ and has the same local charge density as $f(\mathbf{k}, \mathbf{r})$. The local equilibrium distribution function ensures that the number of electrons is conserved.

If there is no *net* electric charge in the metal, the BTE (2.12) is sufficient to calculate the response of electrons due to an external electric field. In a general case however, one has to also solve for the following Poisson's equation for electric potential $\phi(\mathbf{r})$ together with the BTE.

$$\nabla^2 \phi(\mathbf{r}) = -\frac{q\delta n(\mathbf{r})}{\epsilon} \tag{2.14}$$

$$\delta n(\mathbf{r}) = n(\mathbf{r}) - n_o = \frac{1}{4\pi^3} \int d\mathbf{k} \left[f(\mathbf{k}, \mathbf{r}) - f_o(\varepsilon_\mathbf{k}) \right] \tag{2.15}$$

where n_o is the equilibrium electron number density. At equilibrium, electron charge is canceled by the underlying equal and opposite ion charge. Only the deviations in

electron density enter the Poisson's equation. Depending on the particular problem, these equations have to be supplemented with appropriate boundary conditions.

While evaluating equilibrium properties such as number density or energy density, the following simplification to energy as an independent variable is convenient. This also leads to the definition of *density of states* $g(\varepsilon)$.

$$\frac{1}{4\pi^3}\int d\mathbf{k}F(\varepsilon_{\mathbf{k}}) = \frac{1}{\pi^2}\int_0^\infty k^2 dk F(\varepsilon_{\mathbf{k}}) = \int_0^\infty d\varepsilon g(\varepsilon)F(\varepsilon) \tag{2.16}$$

$$g(\varepsilon) = \frac{m}{\hbar^2\pi^2}\sqrt{\frac{2m\varepsilon}{\hbar^2}} \tag{2.17}$$

where $F(\varepsilon_{\mathbf{k}})$ is an arbitrary function of energy and the subscript $'\mathbf{k}'$ has been dropped to stress that energy is the independent variable.

2.2.2 Linear response and bulk conductivities

In bulk metals, Ohm's Law for electrical transport and Fourier's Law for heat conduction are examples of *linear response*. There is a linear relationship between the applied field and resulting currents. Consider a uniform bulk metal, with electric field E_x along the x–direction. The non-equilibrium distribution function is split as

$$f(\mathbf{k}) = f_o(\varepsilon_{\mathbf{k}}) + f_1(\mathbf{k}) \tag{2.18}$$

where $f_1(\mathbf{k})$ is the perturbation caused by the electric field and is independent of position. With this substitution in Eq. 2.12 and using the fact that $f_{le} = f_o$ since the electron density does not vary, the perturbation is given by,

$$f_1(\mathbf{k}) = \frac{eE_x\tau}{\hbar}\frac{\partial f_o}{\partial k_x} \tag{2.19}$$

where the term involving $E_x\partial f_1/\partial\mathbf{k}$ has been ignored to seek only the linear response, and $q = -e$ has been used. The current density can now be evaluated by using Eq. 2.2. After using $j_x = \sigma E_x$, the bulk electrical conductivity is given by,

$$\sigma_{bulk} = \frac{n_o e^2 \tau}{m} \tag{2.20}$$

16

In obtaining the above expression for electrical conductivity, it has been assumed that the electron gas is degenerate, which justifies the $T = 0$ K assumption for the equilibrium Fermi distribution. The error due to this approximation is on the order of $(k_B T / \varepsilon_F)^2$, which is 1.4×10^{-5} for copper at 300 K. Using similar approximations, the free electron result for bulk thermal conductivity κ_{bulk} is given by

$$\kappa_{bulk} = \frac{\pi^2 n_o k_B^2 T \tau}{3m} \tag{2.21}$$

Equation 2.20 is used to calculate the relaxation time and electron mean free path $\lambda = v_F \tau$ using bulk electrical conductivity data.

2.3 Size effects on electron transport

Size effects become important when at least one of the sample dimensions becomes comparable to the mean free path of transport. In the following sections, size effects on thin films, wires, and constriction are reviewed.

2.3.1 Size effect on thin film electrical conductivity

Fuchs [27] provided the first exact solution of size effect on the electrical conductivity of a thin film within the RTA and free electron model. A phenomenological specularity parameter p was introduced to describe the way electrons interact with the wall. Figure 2.3 shows two extreme cases of electron reflection with the walls of the thin film. In the *specular* case, the incident and reflected angles with respect to the wall are same. In the case of *diffuse* scattering, the electron has an equal probability to emerge in any direction. The specularity parameter p is the fraction of electrons scattered specularly.

The general approach to solve this and other size effect problems is similar to that used in the previous section for bulk electrical conductivity. The distribution function is split into the equilibrium and perturbation function, and only linear response is sought. The perturbation function f_1 now depends in addition on the z coordinate

17
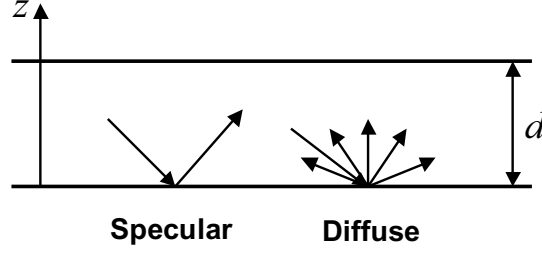
Figure 2.3: Two types of electron scattering by the wall of a thin film.

across the thin film. The solution is given by

$$f_1(\mathbf{k}, z) = \frac{eE_x\tau}{\hbar} \frac{\partial f_o}{\partial k_x} \left[1 - \frac{1-p}{1-p\exp(-d/v_z\tau)} \exp\left(-\frac{z}{v_z\tau}\right) \right] \quad (k_z > 0)$$

$$f_1(\mathbf{k}, z) = \frac{eE_x\tau}{\hbar} \frac{\partial f_o}{\partial k_x} \left[1 - \frac{1-p}{1-p\exp(d/v_z\tau)} \exp\left(-\frac{d-z}{v_z\tau}\right) \right] \quad (k_z < 0) \quad (2.22)$$

An effective film conductivity is defined by calculating the current density using the above expressions and averaging it over the film thickness. The final expression for film conductivity σ_{film} in terms of non-dimensional film thickness $\gamma_d = d/\lambda$ is given by (see Sondheimer [82] for these expressions)

$$\frac{\sigma_{film}}{\sigma_{bulk}} = 1 - \frac{3(1-p)}{2\gamma_d} \int_1^\infty \left(\frac{1}{\xi^3} - \frac{1}{\xi^5} \right) \frac{1 - e^{-\gamma_d\xi}}{1 - pe^{-\gamma_d\xi}} \, d\xi \quad (2.23)$$

Simpler expressions can be written down in the limiting cases

$$\frac{\sigma_{film}}{\sigma_{bulk}} \approx 1 - \frac{3(1-p)}{8\gamma_d} \quad (\gamma_d \gg 1) \quad (2.24)$$

$$\frac{\sigma_{film}}{\sigma_{bulk}} \approx \frac{3(1+p)}{4(1-p)}\gamma_d \ln\frac{1}{\gamma_d} \quad (\gamma_d \ll 1) \quad (2.25)$$

2.3.2 Size effect on circular wire electrical conductivity

The solution for the size effect on a circular wire of diameter D was obtained by Dingle [25] using similar procedures. The conductivity ratio with $\gamma_D = D/\lambda$ is given by

$$\frac{\sigma_{cwire}}{\sigma_{bulk}} = 1 - \frac{12(1-p)^2}{\pi} \sum_{\nu=1}^\infty \nu p^{\nu-1} \int_0^1 (1-\xi^2)^{1/2} L_4(\nu\gamma_D\xi)d\xi \quad (2.26)$$

$$L_n(u) = \int_0^{\pi/2} \exp\left(-\frac{u}{\sin\theta}\right) \cos^2\theta \sin^{n-3}\theta d\theta \quad (2.27)$$

18

and the limiting expressions are

$$\frac{\sigma_{cwire}}{\sigma_{bulk}} \approx 1 - \frac{3(1-p)}{4\gamma_D} + \frac{3(1-p)^2}{8\gamma_D^3} \sum_{\nu=1}^{\infty} p^{\nu-1}/\nu^2 \quad (\gamma_D \gg 1) \tag{2.28}$$

$$\frac{\sigma_{cwire}}{\sigma_{bulk}} \approx \frac{(1-p)\gamma_D}{(1+p)} - \frac{3\gamma_D^2}{8} \left[\frac{1+4p+p^2}{(1-p)^2} \left(\ln\frac{1}{\gamma_D} + 1.059 \right) - (1-p)^2 \sum_{\nu=1}^{\infty} \nu^3 p^{\nu-1} \ln\nu \right]$$
$$- \frac{2\gamma_D^3(1+11p+11p^2+p^3)}{15(1-p)^3} \qquad\qquad (\gamma_D \ll 1) \tag{2.29}$$

2.3.3 Size effect on rectangular wire electrical conductivity

A wire of square cross-section was solved for size effect by MacDonald and Sarginson [55]. A more general case of rectangular cross-section was later treated by Lu et al. [52] for the size effect on thermal conductivity. The expressions obtained for thermal conductivity ratio are identical to electrical conductivity ratio expression obtained by [55] when the sides of the wire are made equal (see the next section for a thorough discussion). The conductivity ratio for a wire of width a and thickness b in terms of non-dimensional parameters $\gamma_a = a/\lambda$ and $\gamma_b = b/\lambda$ is given by

$$\frac{\sigma_{rwire}}{\sigma_{bulk}} = 1 - \frac{3(1-p)}{8} \left(\frac{1}{\gamma_a} + \frac{1}{\gamma_b} \right) - \frac{4(1-p)^2 \ln(1-p)}{5\pi\gamma_a\gamma_b p}$$
$$- \frac{6(1-p)^2}{\pi} \sum_{\nu=1}^{\infty} p^{\nu-1} P(\nu, \gamma_a, \gamma_b) \tag{2.30}$$

$$P(\nu, \gamma_a, \gamma_b) = \int_0^{\pi/4} d\phi \left\{ \frac{1}{\gamma_a} \left[\sin\phi L_5 \left(\frac{\nu\gamma_b}{\cos\phi} \right) - \cos\phi L_5 \left(\frac{\nu\gamma_a}{\cos\phi} \right) \right] \right.$$
$$+ \frac{1}{\gamma_b} \left[\sin\phi L_5 \left(\frac{\nu\gamma_a}{\cos\phi} \right) - \cos\phi L_5 \left(\frac{\nu\gamma_b}{\cos\phi} \right) \right]$$
$$\left. + \frac{1}{\nu\gamma_a\gamma_b} \sin 2\phi \left[L_6 \left(\frac{\nu\gamma_b}{\cos\phi} \right) + L_6 \left(\frac{\nu\gamma_a}{\cos\phi} \right) \right] \right\} \tag{2.31}$$

where the functions L_5 and L_6 are given by Eq. 2.27. In the above expression, a small typo in the original paper by Lu et al. [52] in the coefficient multiplying the summation term has been corrected (the number should be 6 instead of 3).

2.3.4 Extensions to Fuchs-Sondheimer size effect model

Several investigators extended the Fuchs-Sondheimer model for thin metallic films. Ziman [102] argued that the specularity parameter p is a result of interface roughness, and that the diffuse nature of an interface is a direct result of outgoing electron wave interference. He provided an expression for the specularity parameter in terms of surface roughness and electron wavelength, by only treating normal incidence and reflection. Inspired by Ziman [102], Soffer [81] analyzed a more general case of oblique incidence, and obtained an expression for the specularity parameter as a function of angle of incidence. This specularity parameter was then used within the Fuchs-Sondheimer model to calculate effective electrical conductivity. Mayadas and Shatzkes [59] included grain boundary scattering by modeling them as parallel planes, with their normals along the in-plane direction of the thin film. A reflection parameter R was introduced to account for electron reflection with the grain boundaries. Carcia and Suna [16] derived expressions for conductivity of a metal superlattice composed of two different metals. The superlattice in this case is an array of one metal film on top of the other and repeated infinitely. A transmission parameter p was introduced to account for the coherence of electron passage from one metal to the other. Dimmich [24] extended this further by including grain boundary scattering within the Mayadas-Shatzkes model and using two different transmission parameters. He argued that the transmission from one metal to the other need not be same as the transmission *vice versa*.

An important extension to Fuchs model was given by Namba [60]. He assumed that the roughness of a thin film can be idealized by a sinusoidal variation in film thickness $d(x)$ given by

$$d(x) = \bar{d} + h_r \sin\left(\frac{2\pi x}{s}\right) \tag{2.32}$$

where $\bar{d}$ is the average film thickness, h_r is the roughness amplitude, and s is the

wavelength of surface roughness. The mean conductivity $\bar{\sigma}_{film}$ can then be obtained as

$$\frac{\bar{\sigma}_{film}}{\sigma_{bulk}} = \frac{L}{d} \left[\int_0^L \frac{\sigma_{bulk}}{\sigma_{film}[d(x)]d(x)} dx \right]^{-1} \tag{2.33}$$

where $\sigma_{film}[d(x)]$ is the conductivity given by Fuchs expression for a film of thickness $d(x)$, and L is the total length of the film. This expression is simply a series addition of resistances along the film, assuming Fuchs expression is valid over an infinitesimally short film length.

A sinusoidal voltage across a metal conductor at high frequencies results in increasing current densities near the surface. As the current concentration is within a few skin depths near the surface, the net DC resistance increases dramatically at large frequencies. Skin depth δ_s is given by ([38] and [28])

$$\delta_s = \sqrt{\frac{2\rho_e}{\mu\omega}} \tag{2.34}$$

where ω is the frequency of the input voltage signal, ρ_e is the electrical resistivity, and μ is the magnetic permeability. When the mean free path of electrons becomes comparable to skin depth, an anomalous skin effect arises (see [66]). For interconnects operating at gigahertz frequencies, these effects need to be considered. Sarvari and Meindl [75] performed an analysis of this effect for rectangular wires when the dimensions are comparable to mean free path and skin depth. Distribution of current density across the interconnect cross-section results in a distributed heat generation. Nevertheless, this distributed heat generation is unimportant since metals have much higher thermal conductivity and tend to even out the temperature distribution. Thus, for thermal predictions, only an average heat generation across the cross-section is necessary, which should be obtained by performing a detailed electromagnetic analysis of periodic voltage signals.

2.3.5 Wiedemann–Franz Law

According to Wiedemann–Franz Law, the ratio of thermal and electrical conductivity is directly proportional to temperature, with the proportionality constant almost same for all metals [4]. This is an empirical law discovered in 1853. Using expressions 2.20 and 2.21, it can be shown that

$$\frac{\kappa_{bulk}}{\sigma_{bulk}T} = \frac{\pi^2}{3}\left(\frac{k_B}{e}\right)^2 = L_o = 2.44 \times 10^{-8} \text{ W}\Omega/\text{K}^2 \tag{2.35}$$

where the constant L_o is called the Lorenz number. Thus the free electron model, within the relaxation time approximation under linear response, clearly satisfies the Wiedemann–Franz Law.

Deviations from the Wiedemann-Franz law are well known at intermediate temperatures (from few K to few hundred K). This is not a failure of free electron model, as the law can be derived even within semiclassical band theory of electrons. The relaxation time approximation, even with a relaxation time varying with position and wavevector, strictly holds, when the energy $\varepsilon_{\mathbf{k}}$ depends only on the magnitude k, and when the scattering is elastic (energy of the electron is conserved). The Wiedemann–Franz Law however, holds when the collisions are elastic, or at least the change in electron energy after a collision is small when compared with $k_B T$. The dominant scattering mechanism at low temperatures is due to static defects. These collisions are elastic and thus the law holds. At higher temperatures (room temperature and above), collisions with phonons are dominant. At these temperatures, electron-phonon collisions only cause a small change in electron's energy relative to $k_B T$ after a collision. Thus the law also holds at higher temperatures.

The above discussion is limited to bulk metals. It is not clear if the Wiedemann-Franz Law can also be applied for long straight wires and thin films. One might expect it to hold, since collisions with the wall are assumed to conserve electron's energy. Nevertheless, this has been a subject of several theoretical investigations.

Pichard et al. [65], and Kumar and Vradis [48] investigated the case for thin metallic films. Stewart and Norris [84] considered thin circular wires. The main conclusion of these investigations is that the law is essentially unaltered as long as $\varepsilon_F/k_B T \gg 1$. Kumar and Vradis [48] found it to be identically valid for $\varepsilon_F/k_B T > 100$, which is valid at room temperatures for most metals.

2.3.6 Measurements on thin film electrical conductivity

Several investigators measured the electrical conductivity of thin metallic films in the size effect regime (see Chopra [21] for many references). Some of the papers on the resistivity of copper films are reviewed here. Chen and Gardner [19] measured the resistance of interconnects down to 0.25 μm width. They found good agreement with Fuchs-Sondheimer model. Suri [86] analyzed copper thin films ranging from 10 nm to 100 nm in thickness. They were able to fit their data well to Fuchs-Sondheimer model when the thickness was greater than the mean free path. Neither the Fuchs-Sondhiemer model nor the Mayadas-Shatzkes model [59] provided satisfactory agreement for small thicknesses. Fenn et al. [26] investigated copper films from about 5 nm to about 1 μm. They used the Mayadas-Shatzkes model to fit their electrical resistivity measurements. They arbitrarily assumed the specularity parameter p to be 0.5. It was then found that the grain boundary reflection parameter R is almost constant for different thicknesses. Vancea et al. [89] performed an extensive investigation on thin films of various metals. They obtained a good fit with Fuchs-Sondheimer model for large thicknesses. At small thicknesses, significant deviations were reported, and neither the Fuchs-Sondhiemer model nor the Mayadas-Shatzkes model could explain them. They however obtained very good agreement with Fuchs-Namba model [60] over the entire range. They also discussed another model for electrical conductivity of bulk polycrystalline metals (see Reiss [70]). Liu et al. [50] also found good agreement only with Fuchs-Namba model in their measurements on 10 nm to 40 nm thick copper

films.

The main conclusion from these investigations appears to be that Fuchs-Sondheimer model cannot be used directly for very small thicknesses. When the film is very thin, macroscopic surface roughness amplitude becomes comparable to the thickness, which must then be taken into account. This is demonstrated by the success of Fuchs-Namba model in some of the studies. In the studies done by Suri et al. [86], the behavior of electrical conductivity at small thicknesses is very similar to that predicted by Fuchs-Namba model, although they did not compare their results with this model. These investigations do not invalidate Fuchs's original theory of size effect as it was assumed that the thin film is of uniform thickness.

2.3.7 Size effect on electron transport through a constriction

Size effects could be of a semi-classical nature arising at dimensions comparable to the carrier mean free path (described in the previous sections), or can arise due to quantum effects, which is important when dimensions are comparable to carrier wavelength. Carrier wavelength is given by

$$\lambda_F = \frac{2\pi}{k_F} = \frac{2\pi\hbar}{\sqrt{2m\varepsilon_F}} \tag{2.36}$$

which is about 4.63 $\mathring{A}$ in copper. Quantum effects can thus be ignored for on-chip interconnects. Semiclassical size effect described in the above sections arises due to diffuse nature of metal walls. Another size effect of semiclassical nature appears even with specular surfaces when the cross-section of a wire or thin film is not uniform. An ideal constriction or orifice can be modeled as two infinite half-spaces separated by an infinitesimally thin dielectric with a small aperture that connects the two spaces. Such structures are technologically significant since they closely approximate vias connecting metal lines of different dimensions. This size effect will remain even if perfectly specular interfaces are fabricated.

Several published works provided expressions for the resistance of constrictions

between semi-infinite spaces. Sharvin [78] gave an expression for the constriction resistance which is valid when the radius of the aperture is much smaller than the mean free path. Such structures are of fundamental significance since one can study scattering mechanisms through point contact spectroscopy [41]. In the other extreme of large radius when compared to mean free path, Maxwell provided a simple expression for the resistance through the solution of Poisson's equation [58]. Wexler [95] provided an approximate interpolation formula when the aperture radius and mean free path are comparable. Recently Nikolic and Allen [64] obtained an exact solution for the same problem. deJong [23] evaluated the conductance of a finite length constriction connected to electron reservoirs through perfect leads, and observed that a naive sum of Sharvin and Maxwell resistance of the constriction is within 3.5% of the exact results for the three-dimensional case.

2.4 Numerical approaches to simulate electron transport

The BTE for static cases (2.12) is a six-dimensional equation. Straightforward discretization in each dimension would lead to a huge model. In this regard, Monte Carlo techniques are quite popular to simulate electron transport in semiconductors. Excellent reviews of this technique are given by Price [68], and Jacoboni and Reggiani [39]. In a typical ensemble Monte Carlo routine, each electron undergoes a series of events involving free flights for a preselected duration, and a scattering event at the end of the free flight. The motion during free flight is governed by the semiclassical equations of motion (2.6). The duration of the free flight is chosen with a probability distribution determined by the scattering probabilities. At the end of the free flight, a scattering mechanism is chosen according to relative probabilities of all possible scattering mechanisms. A new wavevector resulting from this scattering mechanism is assigned to the electron. These steps are repeated until a steady state is reached. With an ensemble of electrons, one essentially obtains the distribution function, from

which other parameters of interest can be claculated.

One siginificant difficulty with Monte Carlo techniques is their inability to handle degenerate systems satisfactorily. Metals and some semiconductors (such a GaAs) are degenerate, where the Pauli principle for electrons must be respected to obtain a reasonable distribution function. Lugli and Ferry [53] developed a rejection procedure to account for Pauli principle in a Monte Carlo simulation. Romano and Dallacasa [71] implemented this technique for metallic systems and obtained bulk resistivity values with realistic phonon scattering. This procedure is computationally expensive. In metals at room temperature, only electrons at the Fermi level play a role. Pauli principle can be avoided, if one considers electrons only at the Fermi level. Luthi and Wyder [54] exploited this aspect and simulated size effect in a thin film. It has also been used by Bulashenko et al. [14] to calculate current fluctuations in a thin metal film. More recently, Boughton and Feng [12] included realistic phonon scattering to calculate size effect in a thin film using the Monte Carlo technique for electrons on the Fermi level.

In some instances, the BTE should be solved self-consistently with the Poisson's equation. In general, for degenerate systems, this is a very difficult task. It turns out that, in linear response, the BTE can be decoupled from the Poisson's equation. This fact is exploited in solving for electron transport through constriction or point contact (see [41] and [64]). This development is described in Chapter 4 and used in the numerical simulation.

2.5 Techniques to measure thin film thermal conductivity

There are several techniques to measure thin film thermal conductivity. In this section, experimental techniques to measure in-plane thermal conductivity of thin metallic films are reviewed. These techniques can be broadly classified among steady state

and transient techniques. Steady state techniques can directly yield the thermal conductivity. In contrast, transient techniques yield the thermal diffusivity. To deduce thermal conductivity, either the heat capacity is assumed to be the same as the bulk value, or is measured separately.

2.5.1 Steady state techniques

In almost all the steady state techniques, a suspended metal bridge, or a metal and low thermal conductivity substrate composite bridge, is used to measure the thermal conductivity of the metal film. Nath and Chopra [61] developed two techniques to measure thermal conductivity of thin metal films. Their technique is schematically shown in Figure 2.4. A large copper block with a heating element below acts as the heat source. The lead sheet wrapped near the other end of the structure acts a sink. The thermocouples measure the temperature difference. Heat flow through the structure is measured by calibrating the sink's heat transfer coefficient. A one dimensional heat transfer model is assumed to be valid along the metal film and mica double layer. A bare mica film and a metal deposited mica film are used to deduce the metal thermal conductivity. Their transient technique is similar to the steady state technique. The difference is in the way heat flow is measured. In the transient technique, the temperature change in the heat sink is measured, and the heat capacity is used to calculate the net flow of heat. Pompe and Schmidt [67] developed a technique similar to the steady state one described above. The variations are in the heat source and heat sink.

In the technique developed by Boiko et al. [10], the ends of a self-supporting metal film are fastened to a holder. This holder is large and maintains both the ends of the foil at room temperature. A current is passed through the foil, and Joule heating results in a temperature gradient along the metal line. Temperature distribution along the film is measured by an electron diffraction method. A one-dimensional fin
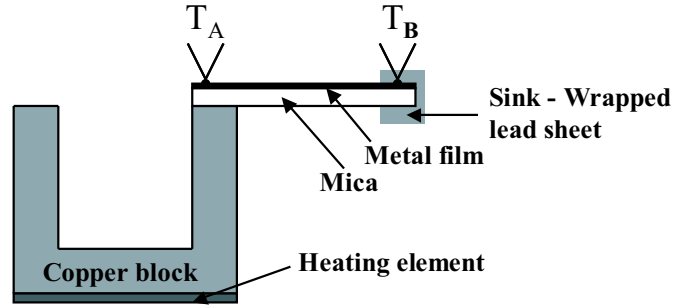
Figure 2.4: Experimental structure of Nath and Chopra [61] to measure the thermal conductivity of a thin metallic film.

equation model including radiation loss is used to obtain thermal conductivity and emissivity of the metal film by a least squares fit. Volklein and Kessler [92] developed a similar technique.

By using micromachining, it is possible to suspend a cantilever type of structure with heating and sensing elements patterned on the cantilever. Such a microstructure was used by Volkelin and Baltes [91] to measure the thermal conductivity of polysilicon films. One end of the cantilever has a heater and a temperature sensor (a metal line). The other end is attached to silicon and is assumed to be at room temperature. A one-dimensional model is used for heat conduction through all the parallel layers in the cantilever. The thermal conductivity of the film of interest is measured by using two cantilevers. One has all the layers, and the film of interest is absent in the other. This technique was used by von Arx et al. [3] for measuring thermal conductivity of silicon dioxide, silicon nitride, aluminum metal, and polysilicon, all used in a standard CMOS process.

Shojaei-Zadeh et al. [80] and Zhang et al. [101] used a suspended metal bridge and induced a temperature gradient by Joule heating. The average temperature rise of the metal line was measured by resistance thermometry. This was then correlated to the thermal conductivity using a one-dimensional heat conduction model. It was assumed that the ends of the line attached to silicon are at room temperature.

Kanthal wire to generate heat pulse

T_A T_B

Metal film

Copper block

Low thermal conductivity isolator block
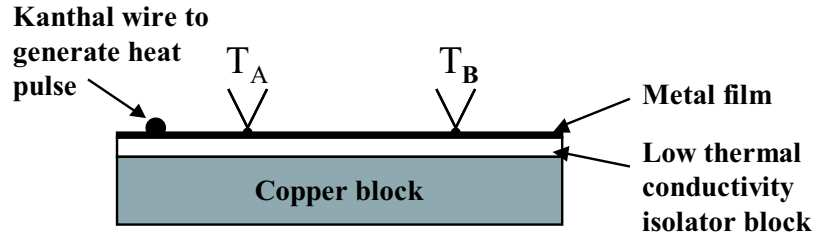
Figure 2.5: Experimental structure of Kelemen [45] to measure the thermal conductivity of a thin metallic film.

Main drawbacks of steady state techniques are heat loss due to radiation, or thermocouple and sensor errors. The Joule heated suspended metal bridge appears to be ideal for thermal conductivity determination of interconnects in the sub-100 nm range. These structures though require complex microfabrication to obtain suspended structures. In addition, there is no reason to believe that the interface quality does not change after these fabrication steps. Thermal conductivity is a strong function of interface scattering in thin films and every effort must be made to preserve the original interface.

2.5.2 Transient techniques

Kelemen [45] described a transient technique to measure thermal diffusivity of thin films. This technique is schematically shown in Figure 2.5. A heating element provides a pulse at one end of the film. The temperature is measured at two locations along the film. A one dimensional transient heat conduction model is used to extract the thermal diffusivity. Heat generation need not be measured since thermal diffusivity depends only on the temperatures at the two locations, the distance of these locations from the heat source, and time.

A technique similar in principle to that of Kelemen [45] was developed by Hatta [31]. This technique is shown in Figure 2.6. An AC light irradiation acts as the heat source. Lateral heat penetration can be quantified using a thermocouple, and
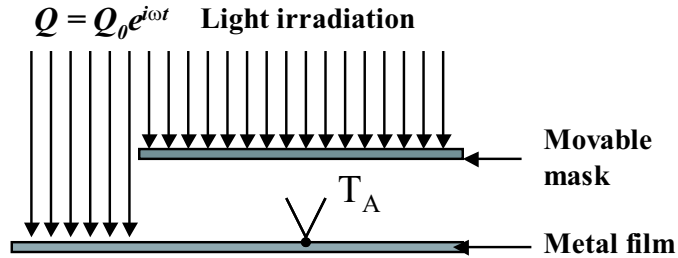
Figure 2.6: Experimental structure of Hatta [31] to measure the thermal conductivity of a thin metallic film.

by varying the mask position. Thermal diffusivity is calculated by using a one-dimensional model. Hatta [31] originally implemented the technique on very thick specimens. Yamane et al., [96] and [97], developed it further for multilayer films to enable measurements on much thinner films.

Kemp et al. [46] and Langer et al. [49] used AC laser irradiation and observed two-dimensional spreading of the thermal wave. Kemp [46] used a thermocouple fixed at one location to measure the temperature amplitude as the laser is moved on the foil. Langer [49] in turn used thermoreflectance from the film to deduce the temperature rise. Measurements at two locations yield the thermal diffusivity of the thin film.

Volklein and Starz [93] developed a microfabricated structure to enable in-situ thermal conductivity measurements of thin metallic films as they grow. The cross-section of their structure is schematically shown in Figure 2.7. The metal line heats up and causes lateral heat flow through the dielectric and metal films. The ends of the films are attached to silicon and are assumed to be at room temperature. The temperature rise of the metal line is measured by monitoring resistance change. By using steady state and transient measurements, Volklein and Starz [93] were able to measure heat capacity and thermal conductivity of thin metallic films.

Lu et al. [51] described a 3ω technique to measure specific heat and thermal conductivity of thin wires. AC heating in a wire results in a voltage component at 3ω due to resistance variation caused by temperature variation. The thin wire is
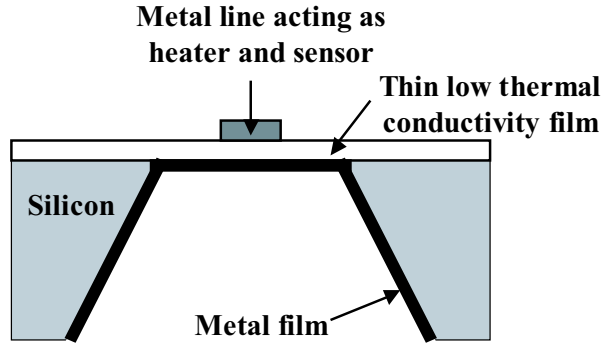
Figure 2.7: Experimental structure of Volklein and Starz [93] to measure the thermal conductivity of a thin metallic film.

suspended off of a substrate. The ends are attached to the substrate to provide a constant temperature boundary condition. Measuring the 3ω component at various frequencies yields thermal conductivity and specific heat of the wire. Yang and Ashegi [98] extended such a technique by eliminating the need for a suspended structure. They used extensive three-dimensional modeling to account for substrate effect.

Most of the techniques described above cannot be directly used for interconnects in the sub-100 nm regime. The 3ω technique by Yang and Ashegi [98] appears well suited for this purpose, although they calculated a very low sensitivity for this technique, primarily due to substrate effect. The length of the interconnect needs to be only a few microns for the best sensitivity. It should be noted that, in this technique, only an average temperature amplitude of the interconnect is measured. Any possible interfacial defects along the interconnect will go unnoticed.

2.6   High resolution temperature measurement

A high spatial resolution temperature measurement technique is necessary to characterize thermal transport in nanoscale interconnects. Resistance thermometry using sub-100 nm metal lines and nanowires does offer nanoscale resolution, but only an average temperature rise of the whole wire is accessible. In addition, this technique is plagued by large leads to enable resistance measurements. Infrared Microscopy

31

does offer thermal images of a large two-dimensional region, but the resolution is limited to few microns. Careful calibration and radiation from the surroundings pose a tremendous challenge towards obtaining accurate measurements.

The Atomic Force Microscope (AFM) is very popular in nanoscale characterization. Temperature measurements can be performed using cantilevers with built-in thermal sensors. These sensors can be simple resistors, thermistors, or thermocouples. An extensive review of this technique, Scanning Thermal Microscopy (SThM), is given by Majumdar [56]. In SThM, a tip with the thermal sensor is scanned over the surface of the sample and temperature signal is recorded. Simultaneously, the topography is also obtained by the regular functioning of the AFM. These two signals can be correlated to obtain a temperature map of the surface. There are several drawbacks to this technique. The measured temperature is a strong function of tip-sample heat transfer mechanisms. At small length scales, the interface quality severely affects the heat transport. Careful calibration on similar surfaces is necessary to obtain accurate measurements.

There exists another technique known as Scanning Joule Expansion Microscopy (SJEM), that uses the AFM to characterize thermal transport. This technique developed by Varesi and Majumdar [90], measures the expansion amplitude of the surface. Figure 2.8 adapted from [90] illustrates this technique. In a regular AFM scan in contact mode (tip in contact with the sample), tip deflection is continuously monitored by measuring the photodiode signal. As the sample is scanned in the x-y directions, topographical changes cause the cantilever to bend and alter the photodiode signal. A feedback is then sent to the piezoelectric scanner to adjust its position vertically until the earlier photodiode voltage is reached. The amount by which the piezoelectric scanner moves is then equal to the height variation in the sample. Typical feedback bandwidths go up to 100 kHz. Some AFMs allow you to vary this bandwidth. In SJEM, the sample is heated periodically. In the case of interconnects, metal lines
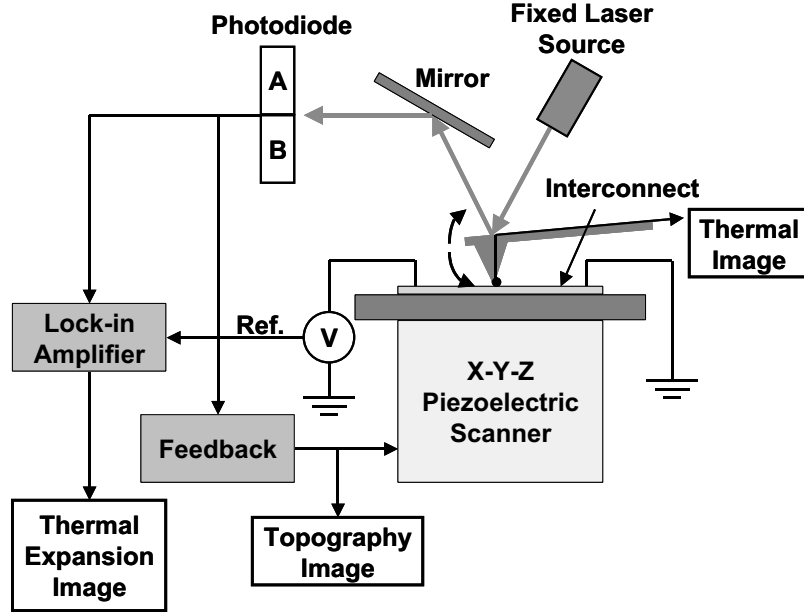
Figure 2.8: A schematic of Scanning Joule Expansion Microscopy (SJEM) and Scanning Thermal Microscopy (SThM) setup.

can be Joule heated using an AC voltage. This Joule heating causes both an AC temperature rise and DC temperature rise. Any temperature rise also causes expansion of the sample if the Coefficient of Thermal Expansion (CTE) is non-zero. The AC temperature rise thus makes the cantilever also oscillate at the heating frequency. The amplitude of this oscillation is simply measured by using a lock-in amplifier as shown in Figure 2.8. In order to differentiate topography from the expansion amplitude, the heating frequency is made higher than the bandwidth of the piezoelectric scanner. The expansion amplitude is then correlated with temperature amplitude. Varesi and Majumdar [90] reported a sub-100 nm resolution with this technique. The technique was also used to characterize temperature rise in vias [36]. One significant disadvantage of this technique is that only an AC temperature rise can be measured. In addition, expansion amplitude is a strong function of heating frequency, and underlying layers dimensions and thermal properties. CTE mismatches can cause significant errors in these measurements. Nevertheless, through careful modeling, it

can be shown that this is a powerful technique to measure temperature rise accurately on some structures.

2.7 The 3ω method

The 3ω method developed by Cahill [15] is a popular technique to measure thermal conductivity of bulk substrates as well as thin films. In this technique, a long metal line is deposited on top of the material of interest. This metal line is excited by a periodic current source $I(t)$ at frequency ω given by

$$I(t) = I_o \cos(\omega t) \tag{2.37}$$

This excitation results in a heat generation that consists of DC and AC components:

$$\dot{q}(t) = I^2(t)R_o = I_o^2 R_o \cos^2(\omega t) = \frac{I_o^2 R_o}{2}(1 + \cos(2\omega t)) \tag{2.38}$$

where R_o is the resistance of the line. Due to linearity of the heat conduction equation, such a heat generation will result in a temperature rise that again has a DC component ΔT_{DC} and an AC component with amplitude ΔT_{AC} at 2ω:

$$T(t) = \Delta T_{DC} + \Delta T_{AC} \cos(2\omega t + \phi) \tag{2.39}$$

where ϕ is the phase lag. This temperature rise then results in a change in the resistance of the line given by

$$R(t) = R_o(1 + \alpha_T \Delta T_{DC} + \alpha_T \Delta T_{AC} \cos(2\omega t + \phi)) \tag{2.40}$$

where α_T is the Temperature Coefficient of Resistivity (TCR) of the line. Thus the net voltage drop across the metal line is given by

$$V(t) = I(t)R(t) = I_o R_o \cos(\omega t)(1 + \alpha_T \Delta T_{DC} + \alpha_T \Delta T_{AC} \cos(2\omega t + \phi)) \tag{2.41}$$

One can split the product of ω and 2ω components using standard trigonometric identity, which results in the following expression for voltage across the metal line.

$$\begin{aligned} V(t) &= I_o R_o(1 + \alpha_T \Delta T_{DC}) \cos(\omega t) + \frac{I_o R_o \alpha_T \Delta T_{AC}}{2} \cos(\omega t + \phi) \\ &+ \frac{I_o R_o \alpha_T \Delta T_{AC}}{2} \cos(3\omega t + \phi) \end{aligned} \tag{2.42}$$

Thus a 3ω component appears in the voltage signal that is proportional to AC temperature amplitude. A lock-in amplifier is used to measure this particular component, and one can then calculate the temperature amplitude if other parameters are known.

The temperature amplitude ΔT_{AC} is mainly a function of the underlying film or substrate properties. Cahill [15] provided an analytical solution for this amplitude in the case of a semi-infinite substrate. This solution was later extended by Borca-Tasciuc et al. [11] to a multilayer stack with anisotropic properties. Although metal specific heat was taken into account by Borca-Tasciuc et al. [11], they ignored the effect of thermal conduction within the metal heater. Jacquot et al. [40] numerically solved the complete problem without any approximations. Even though metal thermal conduction was discussed, nothing was mentioned about its impact on anisotropic thermal conductivity measurements. They solved a transient problem using the finite volume method and extracted the temperature amplitude after the solution attained a quasi-steady state.

CHAPTER III

COMPACT INTERCONNECT THERMAL MODELING

In this chapter a compact approach to interconnect thermal modeling is proposed and investigated for representative interconnect architectures.

3.1   Compact thermal modeling in two dimensions

In a conventional finite element analysis, the spatial domain of interest is discretized into elements such that the region inside an element is homogeneous, although it can have anisotropic thermal conductivity. In the proposed compact approach, a given element is allowed to contain both metal and dielectric regions. For simplicity, the method is described only for a two-dimensional case since the three-dimensional development proceeds along similar lines. Both conventional and compact rectangular elements are contrasted in Figure 3.1. The compact element contains both metallic and dielectric regions. The element is normalized to 1×1 size and the metallic region occupies $a \times b$ size near the origin. Temperature within the element is interpolated from nodal temperatures using weighting functions. Assuming T_i to be the temperature at node i, and $N_i(x, y)$ to be the weighting function for node i, the temperature field within the element is given by

$$T(x, y) = \sum_{i=1}^{4} N_i(x, y) T_i \qquad (3.1)$$

36
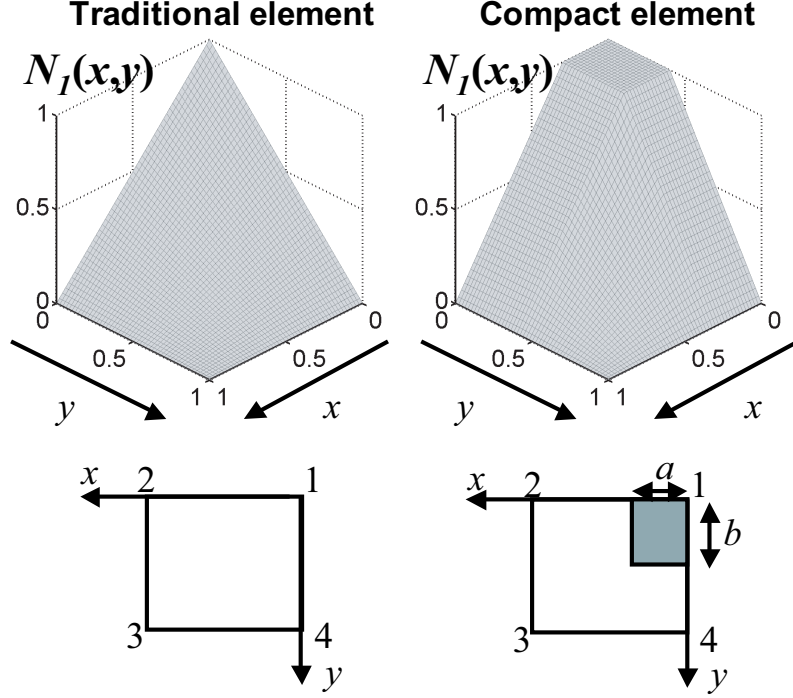
Figure 3.1: A conventional element and a compact element are contrasted at the bottom. The compact element has shaded metallic regions together with dielectric regions. The interpolating function for node 1 in both approaches is shown above. In the compact element case, this function ignores temperature drop across the metallic region.

The weighting functions in the general case can be written as

$$
\begin{aligned}
N_1(x, y) &= [1 - F(x; a)][1 - F(y; b)] \\
N_2(x, y) &= [F(x; a)][1 - F(y; b)] \\
N_3(x, y) &= [F(x; a)][F(y; b)] \\
N_4(x, y) &= [1 - F(x; a)][F(y; b)]
\end{aligned}
\tag{3.2}
$$

where $F(x; a)$ is defined using the Heaviside function $H(x)$ as

$$
F(x; a) = \frac{(x - a)H(x - a)}{(1 - a)} \tag{3.3}
$$

$$
\begin{aligned}
H(x - a) &= 0 \text{ if } x < a \\
H(x - a) &= 1 \text{ if } x > a
\end{aligned}
\tag{3.4}
$$

Weighting function $N_1(x, y)$ for node 1 is shown in Figure 3.1 for both approaches (making $a = b = 0$ in the above expressions leads to conventional bilinear weighting functions). These functions approximate the metallic region to have infinite thermal conductivity.

In conventional Finite Element Method (FEM), a weaker formulation is first derived from the heat conduction equation (see Segerlind [77] for details of the FEM):

$$\frac{\partial}{\partial x}\left(k\frac{\partial T(x, y)}{\partial x}\right) + \frac{\partial}{\partial y}\left(k\frac{\partial T(x, y)}{\partial y}\right) + \dot{q}''' = 0 \tag{3.5}$$

The above equation is multiplied by a weighting function and integrated over the whole domain resulting in

$$\int_{\Omega} w(x, y)\left(\frac{\partial}{\partial x}\left(k\frac{\partial T(x, y)}{\partial x}\right) + \frac{\partial}{\partial y}\left(k\frac{\partial T(x, y)}{\partial y}\right) + \dot{q}'''\right) d\Omega = 0 \tag{3.6}$$

where Ω is the domain and $w(x, y)$ is an arbitrary weighting function. Using Gauss theorem, the left hand side can be split into a boundary and area integral as

$$\int_{\Gamma} w(x, y)\vec{q}'' \cdot \hat{n} d\Gamma - \int_{\Omega}\left(k\frac{\partial w(x, y)}{\partial x}\frac{\partial T(x, y)}{\partial x} + k\frac{\partial w(x, y)}{\partial y}\frac{\partial T(x, y)}{\partial y}\right) d\Omega$$
$$+ \int_{\Omega} w(x, y)\dot{q}''' d\Omega = 0 \tag{3.7}$$

The integral around Γ in Eq. 3.7 is evaluated using the boundary conditions. The weighting functions can be chosen to be the same nodal weighting functions that are used to interpolate for the temperature field. If there are N nodes with unknown temperatures, N equations can be derived by replacing $w(x, y)$ with the weighting functions $N_i(x, y)$. For convenience, the area integral is split into individual element integrals. Consider an element of size $L_x \times L_y$ with the metal occupying a fraction a in the x-direction and fraction b in the y-direction near the origin. Substituting for the temperature field within this element and weighting functions for the four nodes in the second term of the above expression results in the following integrals

$$[KX]^{(e)}_{ij} = \int_0^{L_x}\int_0^{L_y} k_d\frac{\partial N_i}{\partial x}\frac{\partial N_j}{\partial x}dxdy \; ; \quad [KY]^{(e)}_{ij} = \int_0^{L_x}\int_0^{L_y} k_d\frac{\partial N_i}{\partial y}\frac{\partial N_j}{\partial y}dxdy \tag{3.8}$$

They are represented in matrix form by defining conductance matrices $[KX]^{(e)}$ and $[KY]^{(e)}$. Here k_d is the thermal conductivity of the dielectric. Note that the contribution from metallic regions to these integrals is zero, and thus the use of dielectric thermal conductivity in these expressions does not lead to any contradiction. The resulting 4×4 symmetric conductance matrices are given as

$$[KX]^{(e)} = \frac{k_d L_y}{L_x} \begin{bmatrix} \frac{(1+2b)}{3(1-a)} & -\frac{(1+2b)}{3(1-a)} & -\frac{(1-b)}{6(1-a)} & \frac{(1-b)}{6(1-a)} \\ . & \frac{(1+2b)}{3(1-a)} & \frac{(1-b)}{6(1-a)} & -\frac{(1-b)}{6(1-a)} \\ . & . & \frac{(1-b)}{3(1-a)} & -\frac{(1-b)}{3(1-a)} \\ . & . & . & \frac{(1-b)}{3(1-a)} \end{bmatrix} \qquad (3.9)$$

$$[KY]^{(e)} = \frac{k_d L_x}{L_y} \begin{bmatrix} \frac{(1+2a)}{3(1-b)} & \frac{(1-a)}{6(1-b)} & -\frac{(1-a)}{6(1-b)} & -\frac{(1+2a)}{3(1-b)} \\ . & \frac{(1-a)}{3(1-b)} & -\frac{(1-a)}{3(1-b)} & -\frac{(1-a)}{6(1-b)} \\ . & . & \frac{(1-a)}{3(1-b)} & \frac{(1-a)}{6(1-b)} \\ . & . & . & \frac{(1+2a)}{3(1-b)} \end{bmatrix} \qquad (3.10)$$

Furthermore, if $\dot{q}_o'''$ is a uniform heat generation in the metallic region, the column vector of elemental source terms is given as

$$[Q]^{(e)} = \dot{q}_o''' L_x L_y \begin{bmatrix} ab \\ 0 \\ 0 \\ 0 \end{bmatrix} \qquad (3.11)$$

The rest of the procedure is similar to conventional finite element analysis. Global conductance matrix is assembled from the element conductance matrix $[K]^{(e)} = [KX]^{(e)} + [KY]^{(e)}$, and the global source vector $[Q]$ is assembled from elemental source vectors (Eq. 3.11) and other boundary conditions (see Segerlind [77] for handling various types of boundary conditions). The resulting set of linear equations can be solved using a variety of iterative and direct linear equation solvers. The final form of these

equations is

$$[K]_{N\times N}\,[T]_{N\times 1} = [Q]_{N\times 1} \tag{3.12}$$

where $[K]_{N\times N}$ is the global conductance matrix, $[T]_{N\times 1}$ is a column vector of nodal temperatures, $[Q]_{N\times 1}$ is the column vector due to sources terms (arises due to heat generation, as well as boundary conditions) and N is the number of nodes where temperature is computed.

3.2   Compact thermal modeling in three dimensions

In three dimensions the derivation proceeds in a manner similar to two dimensions. A typical compact element with the interconnect along z-direction between nodes 1 and 5 is shown in Figure 3.2. The temperature field is approximated from nodal temperatures and weighting functions as

$$T(x,y) = \sum_{i=1}^{8} N_i(x,y)T_i \tag{3.13}$$

where the weighting functions for the compact element in Figure 3.2 are given by

$$
\begin{aligned}
N_1(x,y) &= [1 - F(x;a)][1 - F(y;b)][1 - z] \\
N_2(x,y) &= [F(x;a)][1 - F(y;b)][1 - z] \\
N_3(x,y) &= [F(x;a)][F(y;b)][1 - z] \\
N_4(x,y) &= [1 - F(x;a)][F(y;b)][1 - z] \\
N_5(x,y) &= [1 - F(x;a)][1 - F(y;b)][z] \\
N_6(x,y) &= [F(x;a)][1 - F(y;b)][z] \\
N_7(x,y) &= [F(x;a)][F(y;b)][z] \\
N_8(x,y) &= [1 - F(x;a)][F(y;b)][z]
\end{aligned}
\tag{3.14}
$$

The global conductance matrix is now a sum of three matrices:

$$[K]^{(e)} = \frac{k_d L_y L_z}{L_x}\,[kx]^{(e)} + \frac{k_d L_x L_z}{L_y}\,[ky]^{(e)} + \frac{k_d L_x L_y}{L_z}\,[kz]^{(e)} \tag{3.15}$$
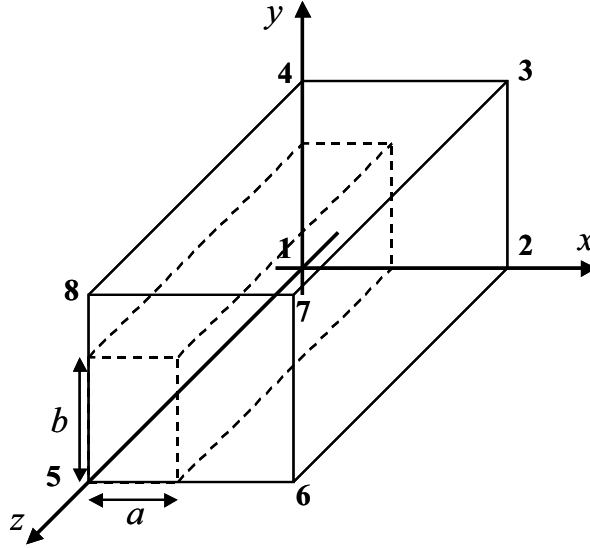
Figure 3.2: A compact element in 3D is shown along with node numbers. The dashed line marks the interconnect aligned along z-direction.

where the elements of individual matrices $[kx]^{(e)}$, $[ky]^{(e)}$ and $[kz]^{(e)}$ are tabulated in Table 3.1. Other elements can easily be deduced from the symmetric property of these matrices. The elemental source vector is given by

$$[Q]^{(e)T} = \dot{q}_o''' \frac{L_x L_y L_z}{2} \begin{bmatrix} ab & 0 & 0 & 0 & ab & 0 & 0 & 0 \end{bmatrix} \qquad (3.16)$$

where T stands for transpose of the matrix.

3.3 Compact model evaluation

In this section, simple two and three dimensional case studies of interconnect temperature rise are performed to evaluate the performance of the compact model. The approach described in the earlier section is implemented in a FORTRAN and MAT-LAB environment. Due to lack of analytical solutions for the case studies performed in this work, detailed finite element simulations were performed. Predictions from these simulations are termed "exact" when quantifying error in the predictions using the compact model.

41

Table 3.1: Elements of the conductance matrices

(i,j)	$[kx]^{(e)}$	$[ky]^{(e)}$	$[kz]^{(e)}$
(1,1)	$\frac{(1)(1+2b)(1)}{(1-a)(3)(3)}$	$\frac{(1+2a)(1)(1)}{(3)(1-b)(3)}$	$\frac{(1+2a)(1+2b)(1)}{(3)(3)(1)} + \frac{(k_m-k_d)ab}{k_d}$
(2,2)	$\frac{(1)(1+2b)(1)}{(1-a)(3)(3)}$	$\frac{(1-a)(1)(1)}{(3)(1-b)(3)}$	$\frac{(1-a)(1+2b)(1)}{(3)(3)(1)}$
(3,3)	$\frac{(1)(1-b)(1)}{(1-a)(3)(3)}$	$\frac{(1-a)(1)(1)}{(3)(1-b)(3)}$	$\frac{(1-a)(1-b)(1)}{(3)(3)(1)}$
(4,4)	$\frac{(1)(1-b)(1)}{(1-a)(3)(3)}$	$\frac{(1+2a)(1)(1)}{(3)(1-b)(3)}$	$\frac{(1+2a)(1-b)(1)}{(3)(3)(1)}$
(5,5)	(1,1)	(1,1)	(1,1)
(6,6)	(2,2)	(2,2)	(2,2)
(7,7)	(3,3)	(3,3)	(3,3)
(8,8)	(4,4)	(4,4)	(4,4)
(1,2)	$\frac{(-1)(1+2b)(1)}{(1-a)(3)(3)}$	$\frac{(1-a)(1)(1)}{(6)(1-b)(3)}$	$\frac{(1-a)(1+2b)(1)}{(6)(3)(1)}$
(1,3)	$\frac{(-1)(1-b)(1)}{(1-a)(6)(3)}$	$\frac{(1-a)(-1)(1)}{(6)(1-b)(3)}$	$\frac{(1-a)(1-b)(1)}{(6)(6)(1)}$
(1,4)	$\frac{(1)(1-b)(1)}{(1-a)(6)(3)}$	$\frac{(1+2a)(-1)(1)}{(3)(1-b)(3)}$	$\frac{(1+2a)(1-b)(1)}{(3)(6)(1)}$
(1,5)	$\frac{(1)(1+2b)(1)}{(1-a)(3)(6)}$	$\frac{(1+2a)(1)(1)}{(3)(1-b)(6)}$	$\frac{(1+2a)(1+2b)(-1)}{(3)(3)(1)} - \frac{(k_m-k_d)ab}{k_d}$
(1,6)	$\frac{(-1)(1+2b)(1)}{(1-a)(3)(6)}$	$\frac{(1-a)(1)(1)}{(6)(1-b)(6)}$	$\frac{(1-a)(1+2b)(-1)}{(6)(3)(1)}$
(1,7)	$\frac{(-1)(1-b)(1)}{(1-a)(6)(6)}$	$\frac{(1-a)(-1)(1)}{(6)(1-b)(6)}$	$\frac{(1-a)(1-b)(-1)}{(6)(6)(1)}$
(1,8)	$\frac{(1)(1-b)(1)}{(1-a)(6)(6)}$	$\frac{(1+2a)(-1)(1)}{(3)(1-b)(6)}$	$\frac{(1+2a)(1-b)(-1)}{(3)(6)(1)}$
(2,3)	$\frac{(1)(1-b)(1)}{(1-a)(6)(3)}$	$\frac{(1-a)(-1)(1)}{(3)(1-b)(3)}$	$\frac{(1-a)(1-b)(1)}{(3)(6)(1)}$
(2,4)	$\frac{(-1)(1-b)(1)}{(1-a)(6)(3)}$	$\frac{(1-a)(-1)(1)}{(6)(1-b)(3)}$	$\frac{(1-a)(1-b)(1)}{(6)(6)(1)}$
(2,5)	$\frac{(-1)(1+2b)(1)}{(1-a)(3)(6)}$	$\frac{(1-a)(1)(1)}{(6)(1-b)(6)}$	$\frac{(1-a)(1+2b)(-1)}{(6)(3)(1)}$
(2,6)	$\frac{(1)(1+2b)(1)}{(1-a)(3)(6)}$	$\frac{(1-a)(1)(1)}{(3)(1-b)(6)}$	$\frac{(1-a)(1+2b)(-1)}{(3)(3)(1)}$
(2,7)	$\frac{(1)(1-b)(1)}{(1-a)(6)(6)}$	$\frac{(1-a)(-1)(1)}{(3)(1-b)(6)}$	$\frac{(1-a)(1-b)(-1)}{(3)(6)(1)}$
(2,8)	$\frac{(-1)(1-b)(1)}{(1-a)(6)(6)}$	$\frac{(1-a)(-1)(1)}{(6)(1-b)(6)}$	$\frac{(1-a)(1-b)(-1)}{(6)(6)(1)}$
(3,4)	$\frac{(-1)(1-b)(1)}{(1-a)(3)(3)}$	$\frac{(1-a)(1)(1)}{(6)(1-b)(3)}$	$\frac{(1-a)(1-b)(1)}{(6)(3)(1)}$
(3,5)	$\frac{(-1)(1-b)(1)}{(1-a)(6)(6)}$	$\frac{(1-a)(-1)(1)}{(6)(1-b)(6)}$	$\frac{(1-a)(1-b)(-1)}{(6)(6)(1)}$

Table 3.1 (continued).

(i,j)	$[kx]^{(e)}$	$[ky]^{(e)}$	$[kz]^{(e)}$
(3,6)	$\frac{(1)(1-b)(1)}{(1-a)(6)(6)}$	$\frac{(1-a)(-1)(1)}{(3)(1-b)(6)}$	$\frac{(1-a)(1-b)(-1)}{(3)(6)(1)}$
(3,7)	$\frac{(1)(1-b)(1)}{(1-a)(3)(6)}$	$\frac{(1-a)(1)(1)}{(3)(1-b)(6)}$	$\frac{(1-a)(1-b)(-1)}{(3)(3)(1)}$
(3,8)	$\frac{(-1)(1-b)(1)}{(1-a)(3)(6)}$	$\frac{(1-a)(1)(1)}{(6)(1-b)(6)}$	$\frac{(1-a)(1-b)(-1)}{(6)(3)(1)}$
(4,5)	$\frac{(1)(1-b)(1)}{(1-a)(6)(6)}$	$\frac{(1+2a)(-1)(1)}{(3)(1-b)(6)}$	$\frac{(1+2a)(1-b)(-1)}{(3)(6)(1)}$
(4,6)	$\frac{(-1)(1-b)(1)}{(1-a)(6)(6)}$	$\frac{(1-a)(-1)(1)}{(6)(1-b)(6)}$	$\frac{(1-a)(1-b)(-1)}{(6)(6)(1)}$
(4,7)	$\frac{(-1)(1-b)(1)}{(1-a)(3)(6)}$	$\frac{(1-a)(1)(1)}{(6)(1-b)(6)}$	$\frac{(1-a)(1-b)(-1)}{(6)(3)(1)}$
(4,8)	$\frac{(1)(1-b)(1)}{(1-a)(3)(6)}$	$\frac{(1+2a)(1)(1)}{(3)(1-b)(6)}$	$\frac{(1+2a)(1-b)(-1)}{(3)(3)(1)}$
(5,6)	(1,2)	(1,2)	(1,2)
(5,7)	(1,3)	(1,3)	(1,3)
(5,8)	(1,4)	(1,4)	(1,4)
(6,7)	(2,3)	(2,3)	(2,3)
(6,8)	(2,4)	(2,4)	(2,4)
(7,8)	(3,4)	(3,4)	(3,4)
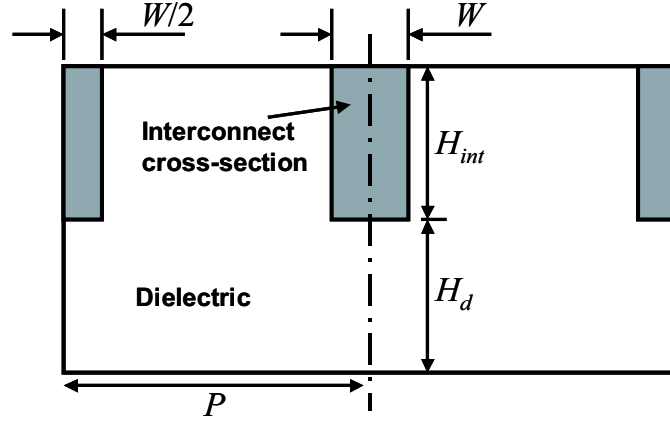
Figure 3.3: A set of uniformly spaced interconnects embedded in the dielectric.

3.3.1 Two-dimensional uniformly spaced interconnects

The simulated domain is shown in Figure 3.3 along with the nomenclature of dimensions. Such a structure closely approximates long uniformly spaced interconnects. Interconnect aspect ratio is close to 2 for structures found in microprocessors, and therefore, H_{int} is fixed at $2W$ [1]. Dielectric thickness H_d is approximately equal to interconnect height and is also fixed at $2W$. Interconnect pitch P though is allowed to vary. The bottom surface is fixed at constant temperature and all other surfaces are assumed to be adiabatic. The detailed model contains 2304 elements. Maximum temperature changes by about 0.2 % when the number of elements is increased from 576 to 2304 (grid size is halved in each direction). The prediction error in using the standard finite element meshes and compact elements (Figure 3.4) is shown in Figure 3.5 as the pitch increases. The error is computed by comparing with detailed simulations. It is assumed that all the interconnects are carrying the same current density. The element count is on a per-pitch basis. The 4-element FEM mesh is the coarsest mesh possible with regular finite elements. This element number is equal to the maximum number of elements in the compact meshes. The solid lines (compact model errors) fall below the 4-element FEM mesh line, which clearly proves the superiority of the

Standard Finite Element Meshes

4 elements   8 elements   12 elements   16 elements

Compact Model Meshes

2 elements   3 elements   4 elements
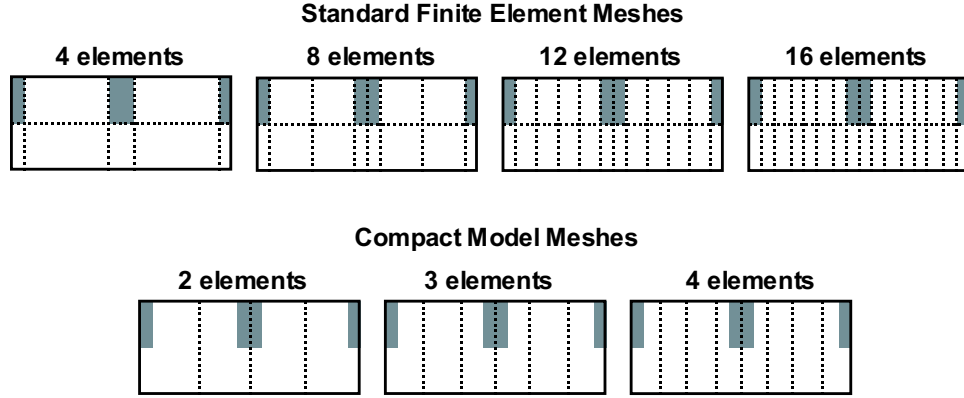
Figure 3.4: Different meshes used in evaluating the performance of compact model when compared with a standard finite element analysis. The number of elements is on a per pitch basis. Percentage errors for these meshes are shown in Figure 3.5.

proposed compact modeling approach. The error in compact model based predictions generally increases as the pitch is increased, although one additional element between the interconnects reduces the error significantly. The simulations suggest that more elements are necessary for large pitches.

Similar set of results are shown in Figures 3.6 and 3.7 but with four elements in the vertical direction for the FEM meshes. Once again, compact modeling predicts the temperature rise as good as the regular finite element mesh while still requiring very few elements. These case studies demonstrate the performance gains obtained by using a compact model mesh in two-dimensions.

A key advantage of the present approach is that it can also capture interactions between adjacent interconnects. In Figure 3.8, temperature rise from detailed and compact model are compared when only the leftmost interconnect is carrying a current of 10 MA/cm² (heat generation is calculated using a resistivity of 2.2 $\mu\Omega$-cm). Metal and dielectric thermal conductivity were fixed at 400 W/mK and 0.17 W/mK respectively. The structure is same as in Figure 3.3. Compact model predicts temperature rise in the middle and right most interconnects quite well for several different pitches when compared with the detailed simulations. The 2-element compact mesh is
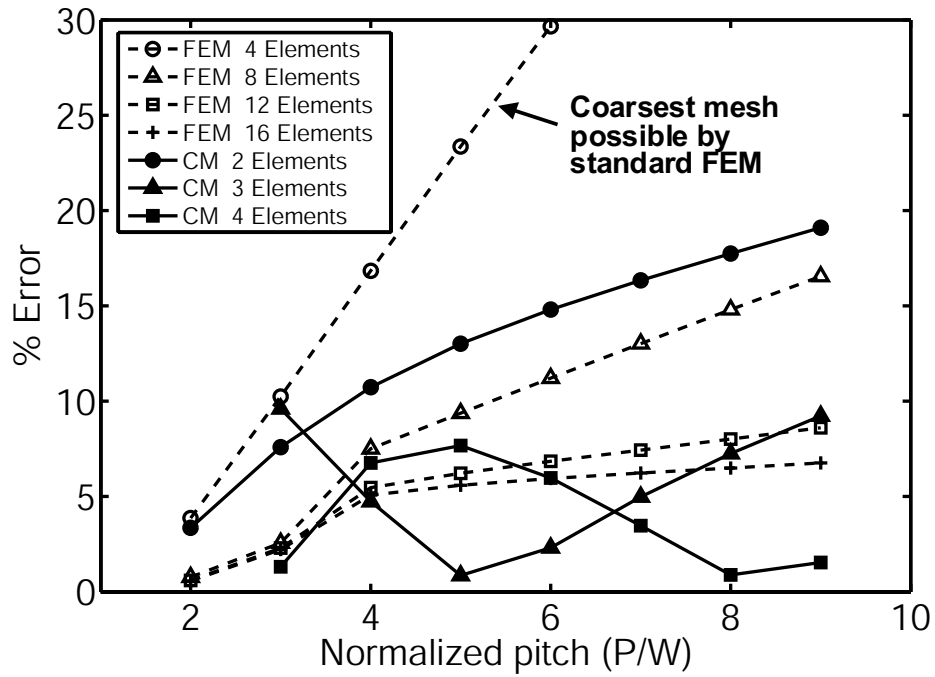
Figure 3.5: Percentage error in predictions using various meshes shown in Figure 3.4.
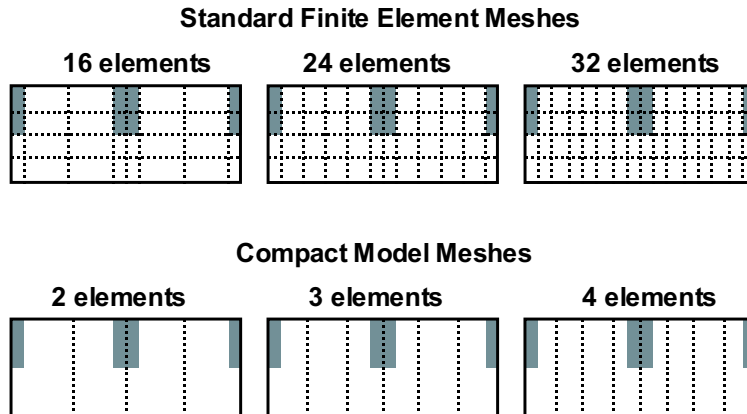
Figure 3.6: Different meshes used in evaluating the performance of compact model when compared with a standard finite element analysis. The number of elements is on a per pitch basis. Percentage errors for these meshes are shown in Figure 3.7.

46
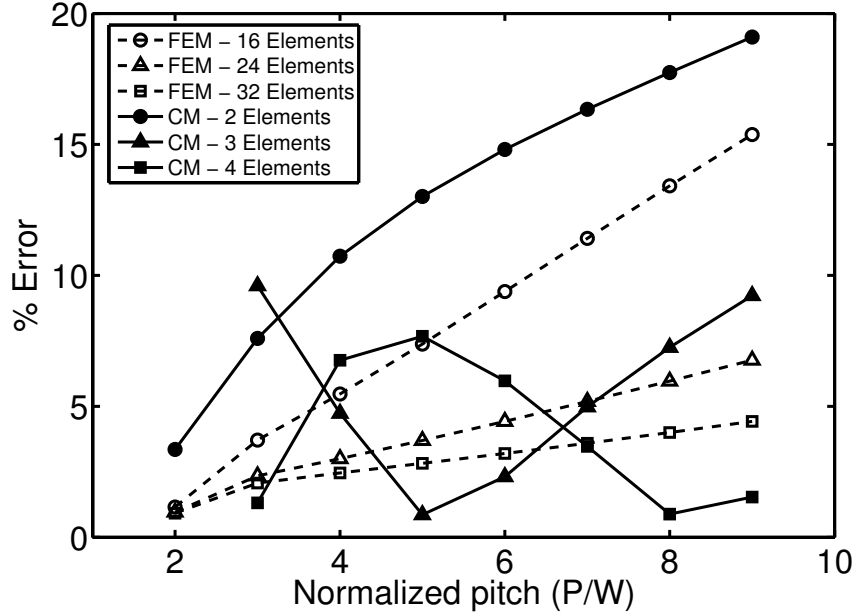
Figure 3.7: Percentage error in predictions using various meshes shown in Figure 3.6.

used for these set of simulations. Such a capability is necessary to accurately predict effective resistance of lines for electric signal time delay calculations.

3.3.2 Three-dimensional interconnects with vias

For three-dimensional studies, interconnects were terminated by vias near the ends as shown schematically in Figure 3.9. This structure reduces to that studied in Section 3.3.1 above when the interconnects are infinitely long. Grid in the cross-sectional region is the same as in the above case. Element length L_e is fixed at 4 μm for different lengths of the interconnects. Temperature rise along the interconnect is shown in Figure 3.10 for several different lengths. Comparison with the detailed model is performed for different interconnect lengths L_{int} and it is found that compact model predictions are within 10 % of the detailed model. Detailed model simulation for 16 μm length interconnects took 57 s while the compact model took only 0.1 s. As the interconnect length becomes very large compared to the characteristic length for temperature gradient (Characteristic length $\lambda = \sqrt{k_m H_{int} H_d / k_d}$ which is equal

47
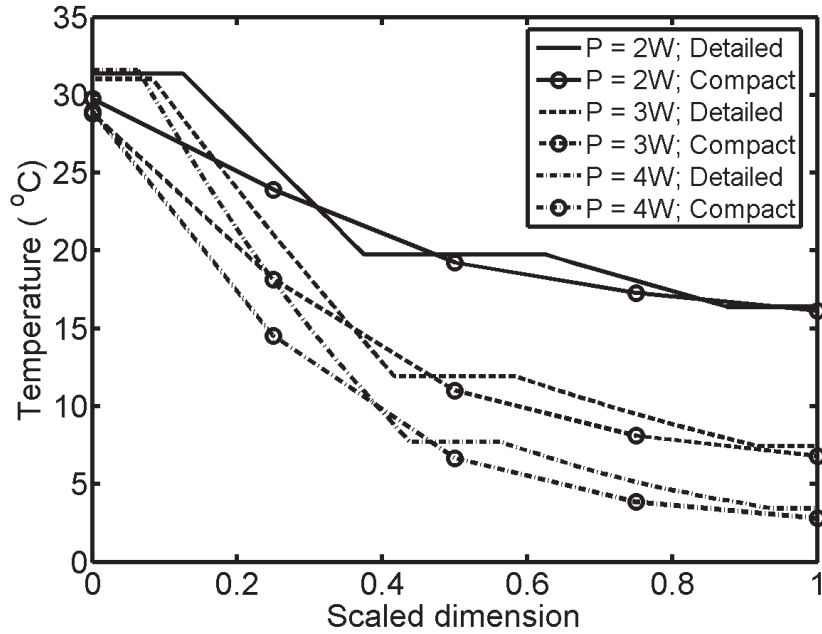
Figure 3.8: Temperature profile for the structure shown in Figure 3.3 when only the left most interconnect is generating heat for various pitches. The flat regions in the detailed model profiles correspond to interconnects and are a result of high metal thermal conductivity.
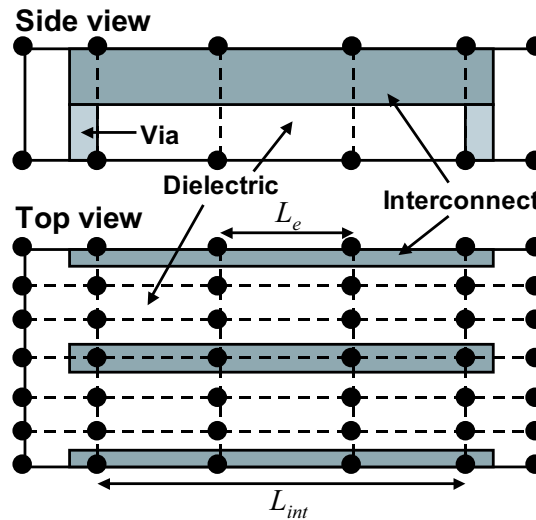
Figure 3.9: A schematic of the three-dimensional interconnect with vias near the ends along with the location of nodes.
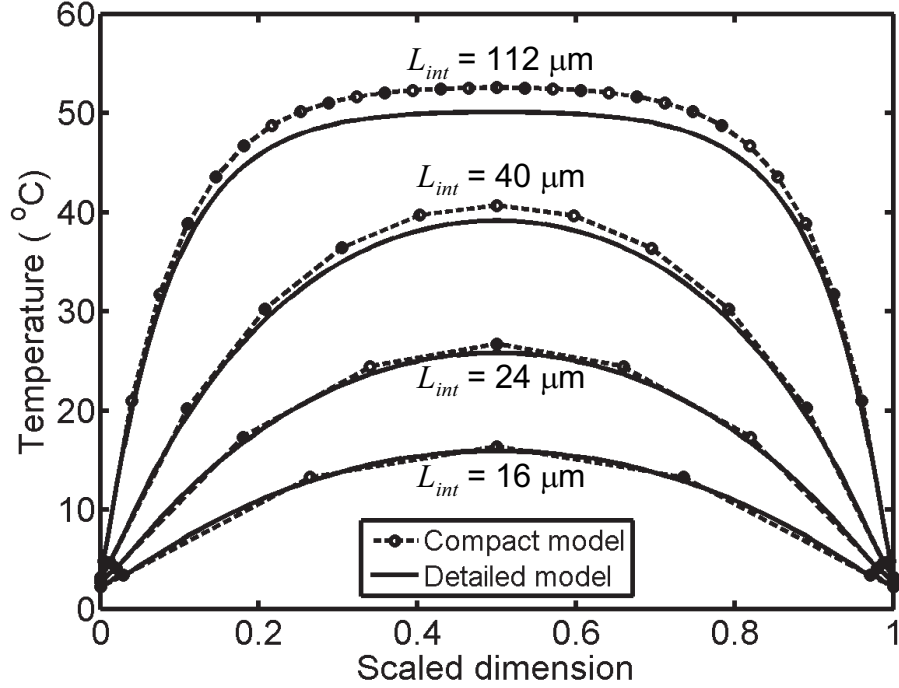
Figure 3.10: Temperature profiles along the interconnect for different lengths. Pitch $P = 4W$ for these simulations.

to 17.47 μm for the structure studied here), temperature near the middle flattens and approaches the two-dimensional value [20]. This trend is clearly captured by the compact model.

3.3.3 Long serpentine interconnect and via chain

The compact thermal modeling approach is implemented for a 500-link M1/V1/M2 serpentine test structure, which is shown in Figure 3.11. This structure has single damascene copper lines at metal 1 (M1) and metal 2 (M2) levels connected by via 1 (V1). In a single damascene process, vias and lines are deposited separately, whereas in a dual damascene process they are filled simultaneously. The length of each interconnect and spacing between the rows is 7 μm. The metal lines are 180 nm wide and 350 nm thick. A cross-sectional view of various layers is shown in Figure 3.12 from the bottom of silicon to the first metal level. Interconnect temperature rise was measured by Ramakrishna et al. [69] by monitoring the resistance change at different
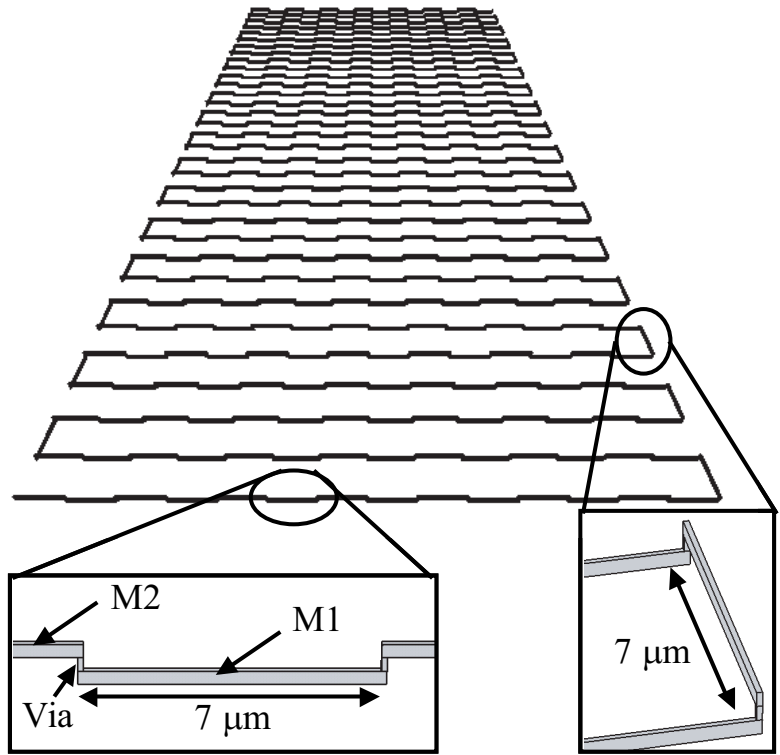
Figure 3.11: A schematic of the long chain of interconnects and vias.

current densities, while maintaining the bottom surface of a 200 mm diameter silicon wafer, which is vacuum clamped to a chuck at room temperature.

The entire test structure consisting of 500 interconnects and 500 vias is modeled by suitably choosing the domain. It is not necessary to model the entire 8-inch diameter silicon wafer, since the heat-generating region is localized to an area of 98 x 224 μm on the wafer. The lateral size of the domain is fixed by comparing its thermal spreading resistance to that of infinite-extent geometry. Based on a closed form solution by Yovanovich et al. [100], a gap of 900 mm on each side (1898 mm x 2024 mm is the total domain size) of the heated region results in a spreading resistance within 1 % of that of an infinite-extent region. Since the heat generating region and domain are rectangular, an area-equivalent radius of a circle is used in the spreading resistance expressions. Temperature dependent calculations are performed using the material properties listed in Tables 3.2 and 3.3. PEN (Plasma Enhanced Nitride) layers in

Table 3.2: Thermal properties used for via chain simulation

Material	Temperature (^oC)	Thermal conductivity (W/mK)
Silicon[a]	− 23.15	191
	26.85	148
	76.85	119
PEN[b] (Plasma Enhanced Nitride)	46.85	1.921
	66.85	2.047
TEOS[c] (Tetraethylorthosilicate)	–	1.31
Copper[d]	− 23.15	328
	26.85	335
	76.85	341
Tantalum[e]	–	57.5
PSG[f] (Phosphosilicate Glass)	–	0.286

a) Ho et al. [32].
b) Griffin et al. [30].
c) Thermal conductivity of TEOS is known to vary considerably [42]. A typical value is chosen and a variation from 1.2 to 1.4 W/mK has been considered in the sensitivity analysis.
d) Assuming Wiedemann-Franz Law holds true [94].
e) Dean [22].
f) Goodson [29]

Table 3.3: Electrical properties used for via chain simulation

Material	Temperature (^oC)	Electrical resistivity ($\mu\Omega$–cm)
Copper	− 23.0	1.726
	27.0	2.066
	77.0	2.405
Tantalum	–	175
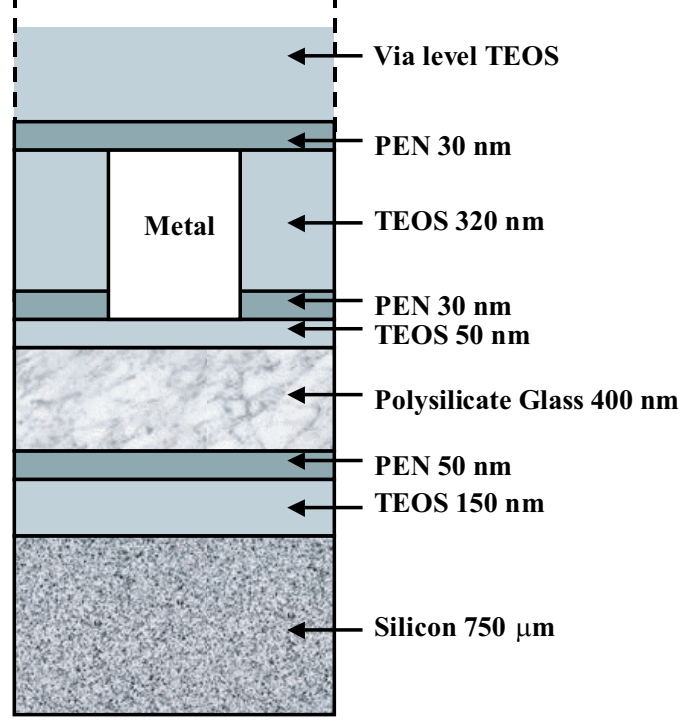
Figure 3.12: Schematic of different layers from the bottom of silicon wafer until metal level 1.

metal and via levels are assumed to be same as TEOS to result in fewer elements. This is justified since their thickness is very small and their thermal conductivity is not very different from that of TEOS. Since the line includes copper as well as tantalum based barrier layer, a one-dimensional electrical model is used to calculate heat generation. The current density through each one of them is given by

$$
j_{Cu} = \left(\frac{I}{A_{Cu}}\right)\left(\frac{\rho_{Ta}/A_{Ta}}{\rho_{Cu}/A_{Cu} + \rho_{Ta}/A_{Ta}}\right)
$$
$$
j_{Ta} = \left(\frac{I}{A_{Ta}}\right)\left(\frac{\rho_{Cu}/A_{Cu}}{\rho_{Cu}/A_{Cu} + \rho_{Ta}/A_{Ta}}\right) \tag{3.17}
$$

where, ρ is electrical resistivity, A is cross-sectional area and I is total current. The heat dissipated in a line of length L is then given by

$$
\dot{Q} = L\left(j_{Cu}^2\rho_{Cu}A_{Cu} + j_{Ta}^2\rho_{Ta}A_{Ta}\right) \tag{3.18}
$$

In order to reduce the number of nodes, the metal line is assumed to be a homogeneous material with its effective thermal conductivity derived from two parallel resistances

for copper line and barrier layer. This can be justified since the thermal conductivity of metal is much higher than the surrounding dielectric and the thickness of tantalum is much smaller in comparison to the line cross-section.

The simulated region consists of about 200,000 elements. A preconditioned conjugate gradient solver is used to solve the large set of linear equations. The preconditioner is a diagonal matrix formed from the values in the main diagonal of the coefficient matrix. The iterations are terminated until a relative residual of 1×10^{-6} is reached. The results change negligibly when the iterations are terminated at a residual of 1×10^{-7}. Each simulation takes about 30 minutes on a 2.8 GHz Pentium Xeon processor running on Windows XP.

The temperature map of the heat generating region is shown in Figure 3.13 for a current density of 23.8 MA/cm^2. Both the top and cross-sectional views clearly show the complex heat flow through the via chain. Although precise periodicity is absent in the present structure due to the end effects, it appears that most of the inner interconnect temperature rises are same. A unit cell model may then be used to calculate the temperature rise to good accuracy.

The average temperature rise and maximum temperature at different current density values is shown in Figure 3.14 along with the measured temperature rise. The average temperature rise is calculated by averaging along the whole chain and is thus expected to be closer to the measured values. Predictions from a detailed finite element model of a unit cell performed by Ramakrishna et al. [69] are also shown in the figure. The unit cell shown in the inset of Figure 3.14 consists of an M1 line, two vias at its ends, and two halves of M2 line on either side of the M1 line. An effective thermal resistance is prescribed on the sides to account for lateral heat loss. Temperature rise from all the simulations are within 5 % of the measurements. Simulations are also performed to include uncertainty in thermal properties. A 10 % uncertainty in silicon properties, 11 % uncertainty in PSG property, and 1.2 - 1.4 W/mK variation
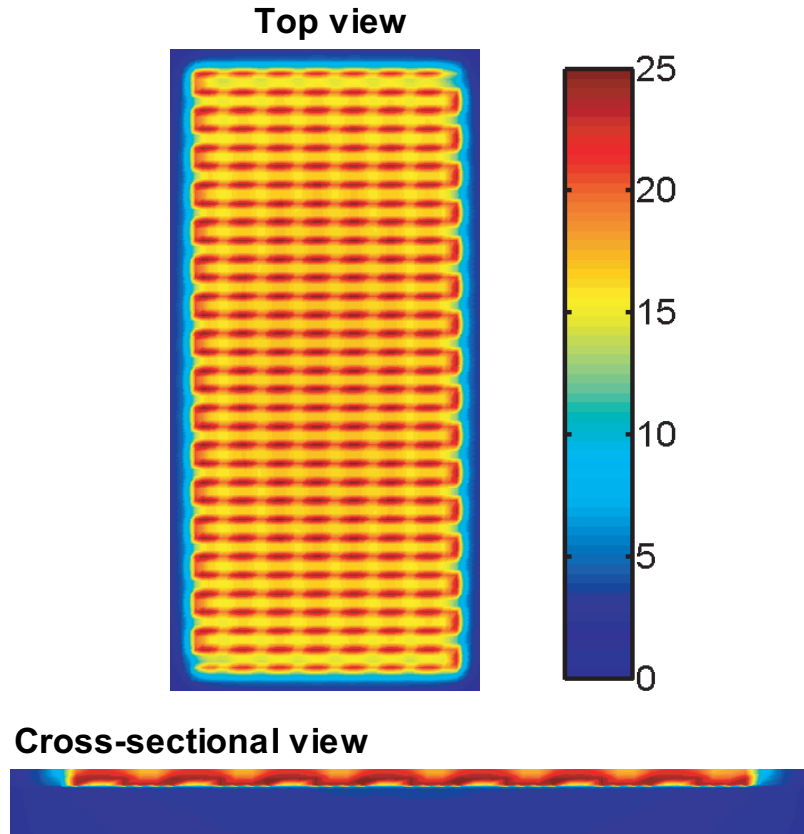
Figure 3.13: Temperature map of the heat generating region for a current density of 23.8 MA/cm^2.

of TEOS thermal conductivity results in the error bars shown for the largest current density data point. Average temperature rise is within 5 % of that predicted by baseline thermal properties listed in Tables 3.2 and 3.3. This study demonstrates the usefulness of the proposed compact approach to model large number of interconnects with sufficient accuracy. Detailed temperature profile along the interconnects is important for calculating critical performance metrics such as time delay and clock skew.
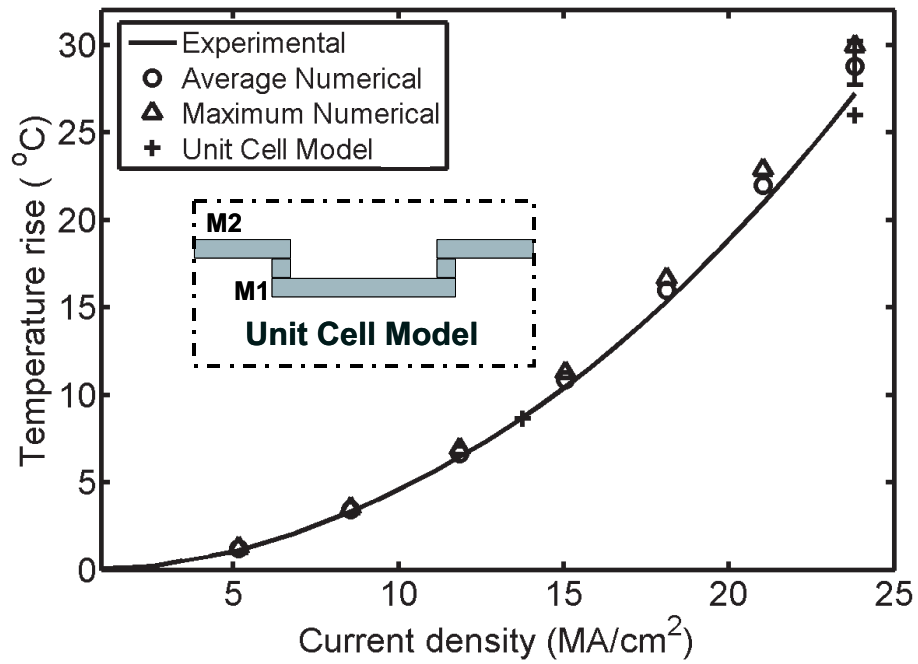
Figure 3.14: Experimental and numerical temperature rise of the interconnect/via chain shown in Figure 3.11. The error bars for the highest current density data point are obtained by including property uncertainties. The unit cell model from Ramakrishna et al. [69] is described in the text.

CHAPTER IV

ELECTRON TRANSPORT AND SIZE EFFECTS

Electron transport through interconnect structures can be described by the Boltzmann Transport Equation (BTE) for electrons. In this chapter, a path integral formulation of BTE is first derived, and a numerical approach to solve this equation is presented. This formulation is then applied on a constriction in a thin metallic film and a short metallic bridge.

4.1 Mathematical Formulation

The steady state Boltzmann Transport Equation (BTE) for the distribution function $f(\mathbf{k}, \mathbf{r})$ of electrons within the relaxation time approximation is given as (electron charge $e < 0$)

$$\mathbf{v_k} \cdot \frac{\partial f(\mathbf{k}, \mathbf{r})}{\partial \mathbf{r}} - \frac{e\nabla\phi}{\hbar} \cdot \frac{\partial f(\mathbf{k}, \mathbf{r})}{\partial \mathbf{k}} = -\frac{f(\mathbf{k}, \mathbf{r}) - f_{le}(\mathbf{k}, \mathbf{r})}{\tau} \tag{4.1}$$

where $\mathbf{k}$ is the wavevector, $\mathbf{r}$ is the position vector, $\mathbf{v_k}$ is the velocity vector as function of wavevector, ϕ is the electric potential and τ is the relaxation time. The local equilibrium distribution function $f_{le}(\mathbf{k}, \mathbf{r})$ is the Fermi-Dirac distribution with a spatially varying chemical potential $\mu(\mathbf{r})$ corresponding to the local density:

$$f_o(\varepsilon_\mathbf{k}) = \frac{1}{1 + \exp[(\varepsilon_\mathbf{k} - \mu)/k_B T]} \tag{4.2}$$

For low external fields, it is convenient to linearize the BTE by defining deviation functions $\Psi(\mathbf{k}, \mathbf{r})$ and $\delta\mu(\mathbf{r})$ such that [64]

$$f(\mathbf{k}, \mathbf{r}) = f_o(\varepsilon_\mathbf{k} - \Psi(\mathbf{k}, \mathbf{r}))$$

$$f_{le}(\mathbf{k}, \mathbf{r}) = f_o(\varepsilon_\mathbf{k} - \delta\mu(\mathbf{r})) \tag{4.3}$$

To first order in deviation functions we have

$$f_o(\varepsilon_{\mathbf{k}} - \Psi(\mathbf{k}, \mathbf{r})) \approx f_o(\varepsilon_{\mathbf{k}}) - \Psi(\mathbf{k}, \mathbf{r})\frac{\partial f_o}{\partial \varepsilon_{\mathbf{k}}}$$

$$f_o(\varepsilon_{\mathbf{k}} - \delta\mu(\mathbf{r})) \approx f_o(\varepsilon_{\mathbf{k}}) - \delta\mu(\mathbf{r})\frac{\partial f_o}{\partial \varepsilon_{\mathbf{k}}} \tag{4.4}$$

The above approximation leads to a linear relationship between voltage drop and current. The deviation $\delta\mu(\mathbf{r})$ in chemical potential is given by the angular average of $\Psi(\mathbf{k}, \mathbf{r})$ at the Fermi level.

$$\delta\mu(\mathbf{r}) = \langle \Psi(\mathbf{k}, \mathbf{r}) \rangle \equiv \frac{1}{4\pi} \int \Psi(\mathbf{k}, \mathbf{r}) d\Omega_{\mathbf{k}} \tag{4.5}$$

where $d\Omega_{\mathbf{k}}$ is differential solid angle. An additional function $u(\mathbf{k}, \mathbf{r})$ can be introduced, which would decouple the solution of Poisson's equation from the BTE. Assuming $\Psi(\mathbf{k}, \mathbf{r}) = u(\mathbf{k}, \mathbf{r}) - e\phi(\mathbf{r})$, the BTE reduces to

$$\mathbf{n_k} \cdot \frac{\partial u(\mathbf{k}, \mathbf{r})}{\partial \mathbf{r}} = \frac{\langle u(\mathbf{k}, \mathbf{r}) \rangle - u(\mathbf{k}, \mathbf{r})}{\tau v_{\mathbf{k}}} \tag{4.6}$$

where $\mathbf{n_k}$ is the unit vector in the direction of $\mathbf{k}$. The above equation can be solved formally, and the solution can be expressed as a path-integral along a given straight line in the direction of $\mathbf{k}$. Denoting variables with subscripts $'i'$ as initial, and subscripts $'f'$ as final, the path-integral solution is given by

$$u(\mathbf{k}, \mathbf{r}_f) = u(\mathbf{k}, \mathbf{r}_i)\exp(-(t_f - t_i)/\tau) + \int_{t_i}^{t_f} \langle u(\mathbf{k}, \mathbf{r}) \rangle \exp(-(t_f - t)/\tau)\frac{dt}{\tau} \tag{4.7}$$

Equation 4.7 is the basis for the iterative numerical scheme described below.

4.2   Numerical Method

Figure 4.1 shows the geometry of the constriction in a thin film. The structure is assumed to be infinite along the normal to the page. When the dimensions a, b, and L are much larger compared to the mean free path, one can calculate the resistance by solving Poisson's equation under space charge neutrality. When spatial dimensions are comparable to mean free path, continuum theory is not appropriate

57
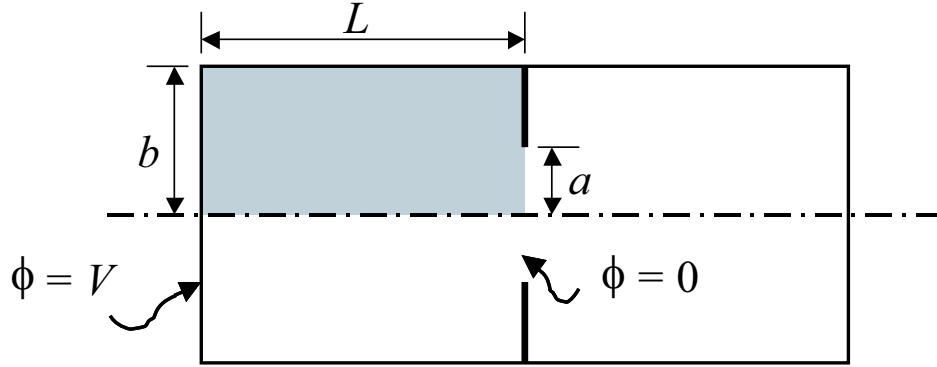
Figure 4.1: Constriction in a finite size thin film. The solution is obtained only for the shaded region.

and BTE solution is necessary to provide accurate results. Only the shaded region needs to be simulated owing to symmetry about the center-line plane perpendicular to the plane of the paper, and antisymmetry about the plane of the constriction opening perpendicular to the plane of the paper. In the numerical approach, the entire simulation region is divided into a rectangular grid. This uniform grid is shown in Figure 4.2. All the variables are defined at nodes, which are points of intersection of the grid lines in this spatial grid. In the **k**-space, only wavevectors near the Fermi level are considered, since for metals, the degeneracy temperature is much higher than normal room temperatures. The Fermi sphere is divided into equal area regions as shown in Figure 4.2. Additional weighting factors are thus not necessary while computing quantities such as current density. Electric current density $\mathbf{j}(\mathbf{r})$ at a given location is then given by

$$\mathbf{j}(\mathbf{r}) = eg(\varepsilon_F)\langle \mathbf{v_k} u(\mathbf{k}, \mathbf{r})\rangle \approx \frac{eg(\varepsilon_F)}{N_{FS}} \sum_i \mathbf{v}_{\mathbf{k}_i} u(\mathbf{k}_i, \mathbf{r}) \tag{4.8}$$

where $g(\varepsilon_F)$ is the density of states at the Fermi level, N_{FS} is the number of regions into which the Fermi sphere is divided, and subscript $'i'$ denotes the ith cell. The numerical solution begins by guessing an initial value for $\langle u(\mathbf{k}, \mathbf{r})\rangle$. The following iterative procedure is employed.

Spatial grid

Fermi sphere grid
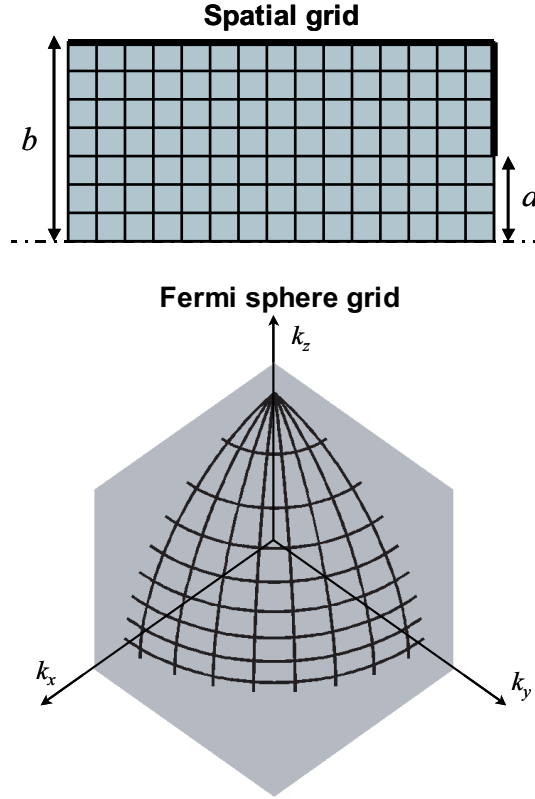
Figure 4.2: Numerical grid in physical and **k**–space. In a free electron model, Fermi surface is spherical.

- Apply the boundary conditions based on the initial guess.

- Evaluate new values for $u(\mathbf{k}, \mathbf{r})$ in the whole region by numerically integrating Eq. 4.7 and performing iterations.

- Evaluate new $\langle u(\mathbf{k}, \mathbf{r}) \rangle$ by averaging $u(\mathbf{k}, \mathbf{r})$ over the Fermi sphere.

- Repeat the above procedure until current continuity is satisfied.

For each spatial location and each Fermi wavevector, in order to evaluate Eq. 4.7, one evaluates a suitable initial time t_i by tracing back in time. A limit for the time backwards is specified for all variables. If within this time the path intersects a boundary, t_i is made equal to the time of intersection. This procedure can be applied for all the values inside the region. At the boundaries though, not all wavevectors originate from

within the domain. Thus $u(\mathbf{k}, \mathbf{r})$ is computed for only those wavevectors that strike the surface. Boundary conditions described later in the section enable the evaluation of $u(\mathbf{k}, \mathbf{r})$ for reflected wavevectors.

A constant potential difference is maintained between the left and right ends. The constriction plane is maintained at zero potential. The solution of Poisson's equation is an initial guess for $\langle u(\mathbf{k}, \mathbf{r}) \rangle$. On the left boundary, an analytical expression for $u(\mathbf{k}, \mathbf{r})$ is applied, as it corresponds to the case of a homogenous medium in a constant electric field, if far from the constriction. For the homogenous case the distribution function is given by

$$f(\mathbf{k}, \mathbf{r}_b) = f_o(\varepsilon_{\mathbf{k}}) - e\mathbf{E}(\mathbf{r}_b).\mathbf{v}_{\mathbf{k}}\tau\frac{\partial f_o}{\partial \varepsilon_{\mathbf{k}}} \tag{4.9}$$

where $\mathbf{E}$ is the electric field and subscript $'b'$ denotes boundary. From the definition of $u(\mathbf{k}, \mathbf{r})$ one obtains

$$u(\mathbf{k}, \mathbf{r}_b) = e(\phi(\mathbf{r}_b) + \mathbf{E}(\mathbf{r}_b).\mathbf{v}_{\mathbf{k}}\tau) \tag{4.10}$$

for the boundary condition on left end. If the walls are diffuse, then the boundary condition is given as

$$u(\mathbf{k}, \mathbf{r}_b) = e(\phi(\mathbf{r}_b) + \mathbf{E}(\mathbf{r}_b).\mathbf{v}_{\mathbf{k}}\tau)\left[1 - \exp\left(\frac{-b-y}{\tau v_{\mathbf{k}y}}\right)\right] \text{ for } v_{\mathbf{k}y} > 0$$

$$u(\mathbf{k}, \mathbf{r}_b) = e(\phi(\mathbf{r}_b) + \mathbf{E}(\mathbf{r}_b).\mathbf{v}_{\mathbf{k}}\tau)\left[1 - \exp\left(\frac{b-y}{\tau v_{\mathbf{k}y}}\right)\right] \text{ for } v_{\mathbf{k}y} < 0 \tag{4.11}$$

Here, the y coordinate is zero on the centerline, and increases in the upward direction. The above expressions are valid only for left boundary when it is far from the constriction. For the walls, specular or diffuse reflection conditions can be applied. If $\mathbf{k}_{inc}$ is the incident wavevector, and $\mathbf{k}_{ref}$ is the specularly reflected wavevector, then $u(\mathbf{k}_{ref}, \mathbf{r}_b) = u(\mathbf{k}_{inc}, \mathbf{r}_b)$ for a specular surface. If the surface is diffuse, then

$$u(\mathbf{k}_{ref}, \mathbf{r}_b) = -\frac{\sum_{\mathbf{k}_i.\mathbf{n}<0} \mathbf{v}_{\mathbf{k}_i} u(\mathbf{k}_i, \mathbf{r}_b)}{\sum_{\mathbf{k}_i.\mathbf{n}>0} \mathbf{v}_{\mathbf{k}_i}} \tag{4.12}$$

60
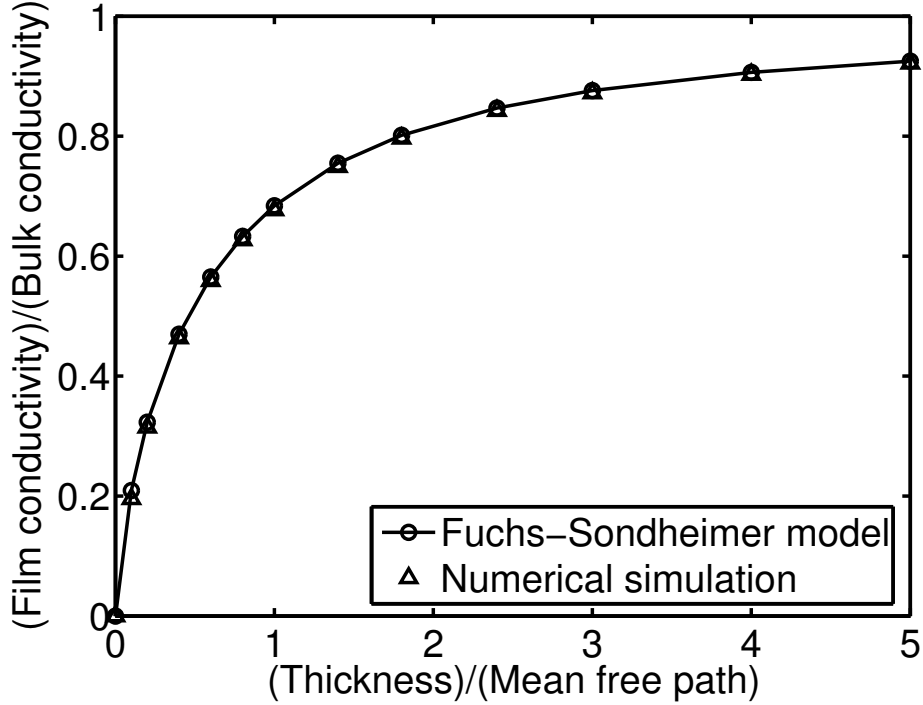
Figure 4.3: Comparison of analytical and numerical effective electrical conductivity reduction as the thickness of a thin film reduces.

where $\mathbf{n}$ is the unit vector normal to the surface directed into the domain. On the right end over the plane of constriction, reflection antisymmetry of $\Psi(\mathbf{k}, \mathbf{r})$ implies $u(\mathbf{k}_{ref}, \mathbf{r}_b) = -u(\mathbf{k}_{inc}, \mathbf{r}_b)$ since the potential is specified as zero.

4.3 Size effect on constriction in a thin film

The numerical approach outlined in the previous section is first validated for a thin metallic film for which an analytical solution is available. Figure 4.3 shows the reduction in effective conductivity as the thin film thickness reduces. Numerical approach predicts this reduction well for several thicknesses. For the case with a constriction, several cases are simulated with a constant constriction size and increasing aspect ratio. These results are compared with that obtained by Nikolic and Allen [64] for a circular constriction. The results in [64] are presented as

$$R_c = R_S + \gamma(l/a)R_M \tag{4.13}$$
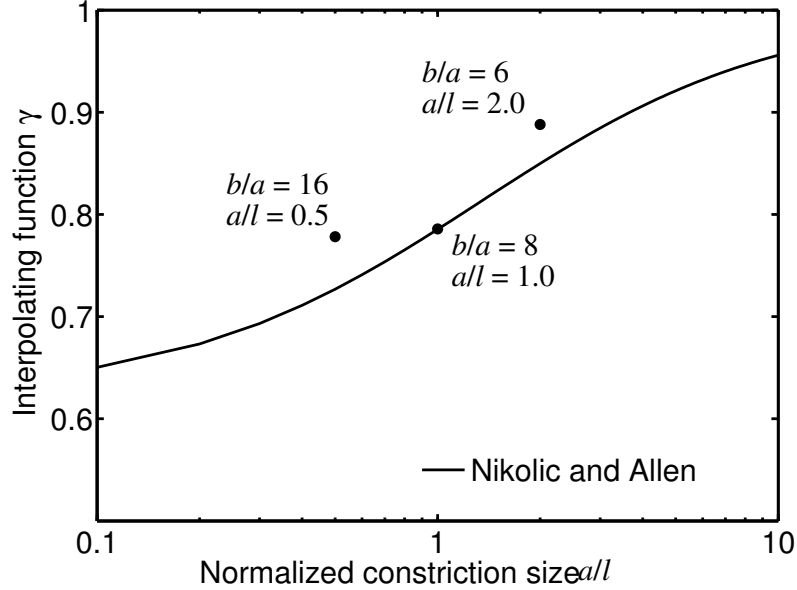
Figure 4.4: Interpolating function evaluated numerically (dots) is compared with the expression from Nikolic and Allen [64]. l is the mean free path. Reference [64] studied a circular constriction in the limit when b/a becomes infinite whereas the results of current study are for a constriction in a thin film. The agreement need not be exact, though at large b/a, the interpolating function for both studies should be comparable which is evident from the shown data points.

where R_c is the constriction resistance, R_S is the Sharvin resistance and R_M is the Maxwell resistance. Sharvin resistance arises purely due to ballistic nature of electrons near the constriction when the constriction size is much smaller than the mean free path. Maxwell resistance is based on continuum theory and involves no microscopic phenomena. The interpolating function $\gamma(l/a)$ signifies the contribution of Maxwell resistance to overall resistance. For a circular constriction of radius a [95],

$$R_M = \frac{\rho}{2a} \; ; \quad R_S = \frac{4\rho l}{3\pi a^2} \tag{4.14}$$

An approximate expression (within 1% fit) was provided by Nikolic and Allen for the interpolating function:

$$\gamma(l/a) = \frac{1 + 0.83(l/a)}{1 + 1.33(l/a)} \tag{4.15}$$

Since in the geometry considered, one has a thin film of finite thickness instead

X - direction current density

Specular walls   Diffuse walls
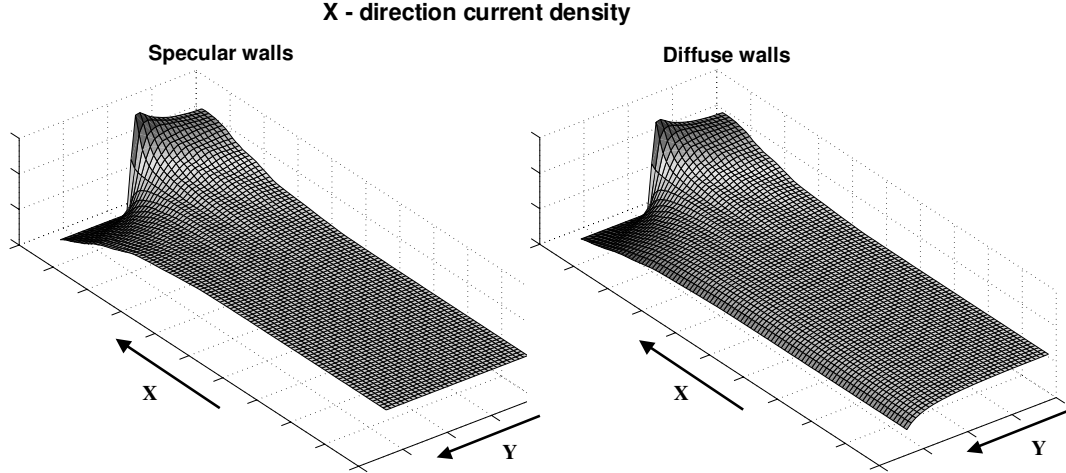
Figure 4.5: Current density through a constriction for specular and diffuse walls. Note the curving of profile near the walls for diffuse surface scattering

of infinite half-spaces, constriction resistance is calculated by subtracting the film resistance without constriction from the calculated resistance. Since all the walls are assumed specular, film resistance is simply $\rho L/2bW$, where W is the width into the plane. W is assumed to be much larger than the mean free path, as the structure is two-dimensional. Figure 4.4 shows the interpolating function evaluated through simulations for high aspect ratios along with that given in [64]. It should be expected that numerical predictions should be comparable with that of [64], but there is no reason for them to be identical since [64] considered a circular constriction while the computations reported here are for a two-dimensional geometry. A schematic of current density over the entire region is contrasted in Figure 4.5 for specular and diffuse walls. With diffuse walls, the current density drops near the walls due to diffuse surface scattering as seen by the curving of the profile. These results substantiate the numerical approach in its ability to capture size effect in complex structures.

Some interesting deviations are found when the aspect ratio b/a is small. The interpolating function calculated from the simulations is shown in Figure 4.6 for $(a/l) = 1.0$ and 0.5 as b/a increases. Note that at low aspect ratios the interpolating
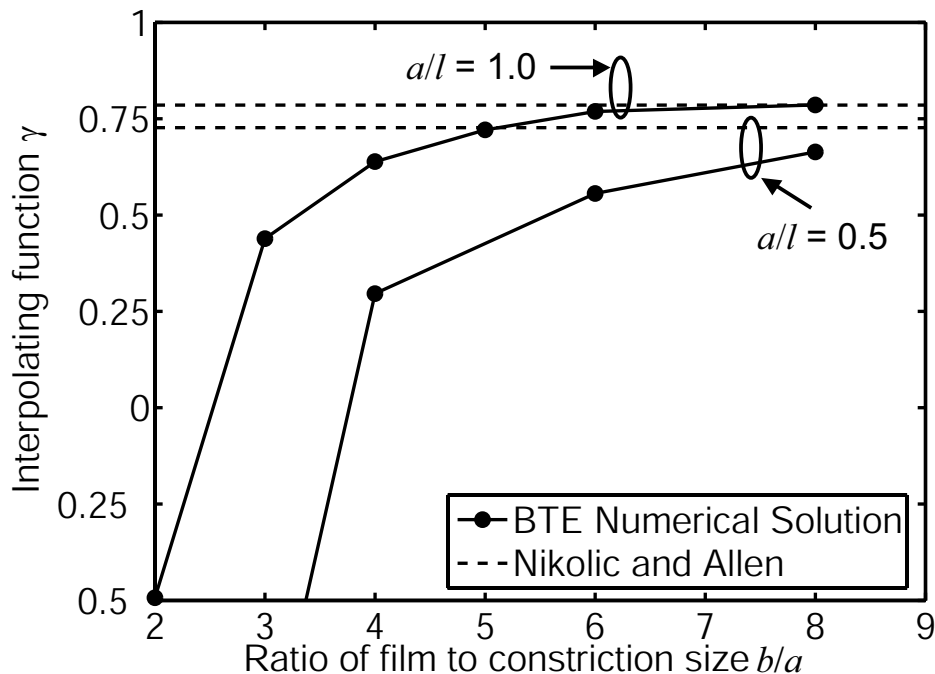
Figure 4.6: Comparison of interpolating function as the thin film width is varied, keeping the constriction size constant. Significant deviations are observed when the aspect ratio b/a is small.

function is negative, which merely states that the constriction resistance is smaller than the Sharvin resistance. Sharvin resistance arises due to electron focusing from an *infinite* region towards the small orifice. A lower Sharvin contribution can thus be expected for finite aspect ratios. As the width $2b$ increases and approaches closer to infinite half-spaces, the results come very close to the circular constriction case. The results suggest that significant deviations should be expected at small aspect ratios. In order to obtain a simple expression for the resistance increase due to the size effect, several cases with varying a/l and b/a were simulated. In particular, small values of a/l and b/a are more important for next generation interconnects. The set of simulation points are plotted in Figure 4.7 along with the fitted curve. A simple expression of the form

$$R_M/R_c = \frac{a/l}{a/l + C(b/a)}; \quad C(b/a) = \exp\left[0.34\left(\frac{b}{a}\right)^2 - 2.21\left(\frac{b}{a}\right) + 3.55\right] \quad (4.16)$$

64
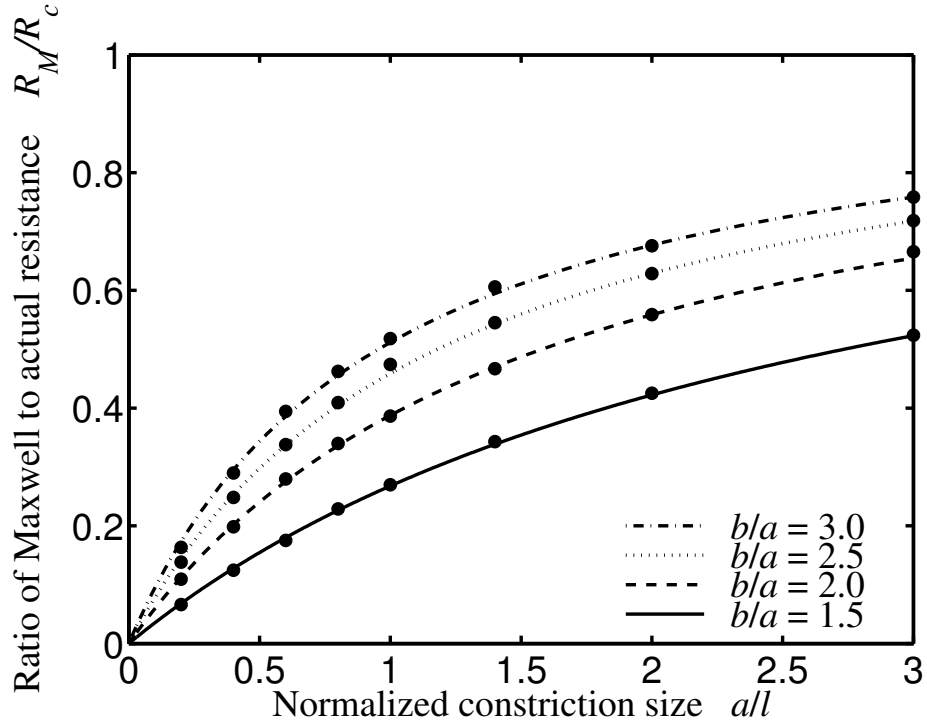
Figure 4.7: Ratio of Maxwell resistance to actual resistance as a function of a/l for several aspect ratios. The filled dots are simulated results for the infinitesimally thin dielectric region and the curves are evaluated from the correlation developed in the current study. The correlation is applicable for small constriction sizes and small aspect ratios.

agrees very well with the calculated values. Here, $C(b/a)$ is a function of the aspect ratio b/a. The maximum deviation is 6.25% with an average deviation within 2% for the simulated 32 numerical data points when compared with that obtained from the above correlation. The above correlation is applicable only within the range $0 < (a/l) < 3.0$ and $0 < (b/a) < 3.0$.

4.4 Size effect on a short metallic bridge

It is of interest to consider a more general validity of the constriction resistance. Instead of an infinitesimally long constriction, a constriction of length $(2a)$ was also simulated for $b/a = 2.0$. The effective conductance of this bridge type structure is shown in Figure 4.8 as the constriction size varies. For this particular case, a simple
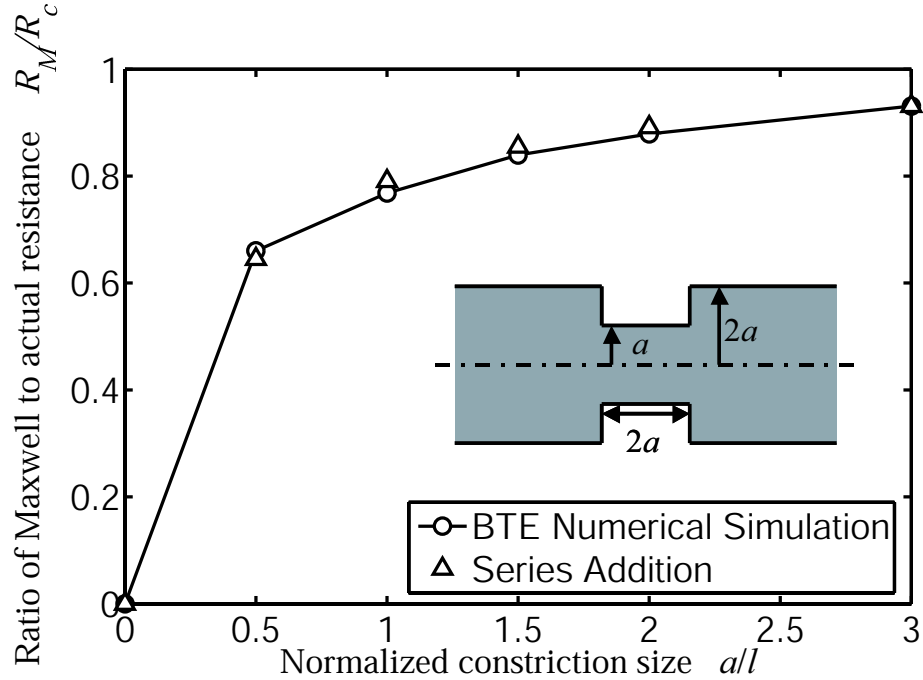
Figure 4.8: Comparison of total resistance obtained using a full BTE simulation and a simple series addition of bridge resistance and constriction resistance.

addition of the zero length constriction resistance and Maxwell resistance was found to be within 3 % of the actual results, which suggests a more general applicability of the present study.

Figure 4.9 illustrates that detailed variation of current density and heat generation can also be obtained from these simulations. As in a classical case, heat generation peaks near the corners [99]. Such high rates of heat generation and current density near the corners are critical for reliability.

In summary, a numerical approach to predict electron transport through BTE within the relaxation time approximation under linear response conditions was developed. Resistance values for a constriction in a thin metallic film were predicted and compared with earlier works. Significant deviations from the ideal constriction case occur at small aspect ratios. A simple expression was fit to the numerical predictions when constriction sizes were comparable to the mean free path. The approach

66
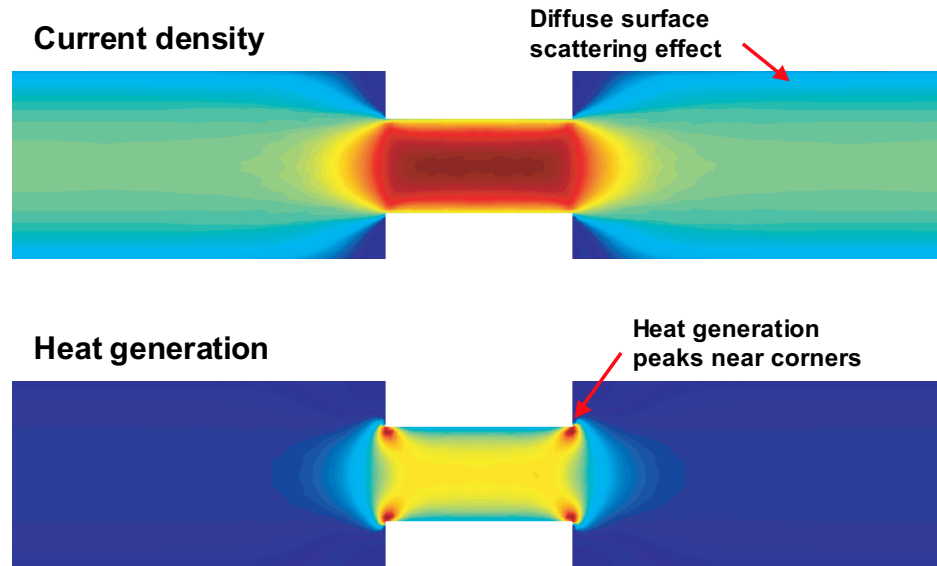
Figure 4.9: Current density and heat generation map of a bridge. The current density is smaller near the edges due to diffuse surface scattering. As with a classical solution of Poisson's equation, heat generation peaks near the corners even in the size effect regime.

outlined here could be a useful technique to predict resistance values for on-chip interconnects.

CHAPTER V

THERMAL CHARACTERIZATION OF THIN METALLIC FILMS USING SCANNING JOULE EXPANSION MICROSCOPY (SJEM)

In this chapter, a constriction in a thin metallic film is excited by an AC voltage source, and the resulting current crowding, heat generation, and temperature rise are investigated. Numerical predictions in the frequency space are compared with experimental measurements made using Scanning Joule Expansion Microscopy (SJEM). A novel technique is proposed to extract the thermal conductivity of thin films, whose thickness is in the electron size effect regime. This technique is then used to measure in-plane thermal conductivities of gold thin films of two different thicknesses. This chapter is organized as follows. After describing preliminary measurements on a constriction in a thin film, the numerical approach in frequency space is described in detail. The effect of electromagnetic skin depth on heat generation is discussed and followed by a detailed description of the thermal conductivity extraction procedure. This procedure assumes linearity between the temperature amplitude and the expansion amplitude, which is justified by a coupled thermomechanical analysis of the structure. Finally, uncertainties in the measurements are quantified.

5.1   SJEM on a constriction

This section describes SJEM measurements on a constriction in a thin metallic film. Current crowding and the associated heat generation non-uniformity result in a significant variation in temperature amplitude near the constriction.
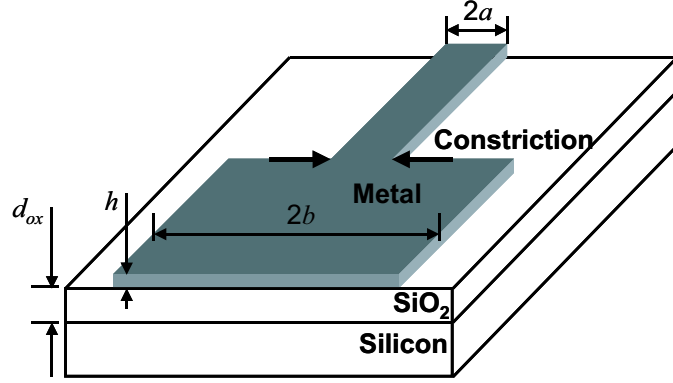
Figure 5.1: A schematic of the constriction in a metal thin film

5.1.1 Constriction test structures

Figure 5.1 shows a schematic of the constriction and the different layers underneath the metal film. Both the shorter ($2a$) and longer ($2b$) width lines extend to more than 2 mm in length. End effects do not affect the electrical and thermal transport near the constriction since the widths are much smaller than the lengths. The metal line was deposited using electron beam evaporation of gold and patterned by the lift-off technique. The silicon dioxide layer underneath was deposited by PECVD process. Two structures, Constriction - A and Constriction - B, of different thicknesses were investigated. All the dimensions of these structures are given in Table 5.3.

Table 5.1: Dimensions of constrictions investigated in the present work

	Constriction - A	Constriction - B
Shorter width ($2a$)	7.01 μm	6.2 μm
Longer width ($2b$)	200 μm	200 μm
Metal thickness (h)	43.4 nm	131.3 nm
Oxide thickness (d_{ox})	849 nm	7.72 μm
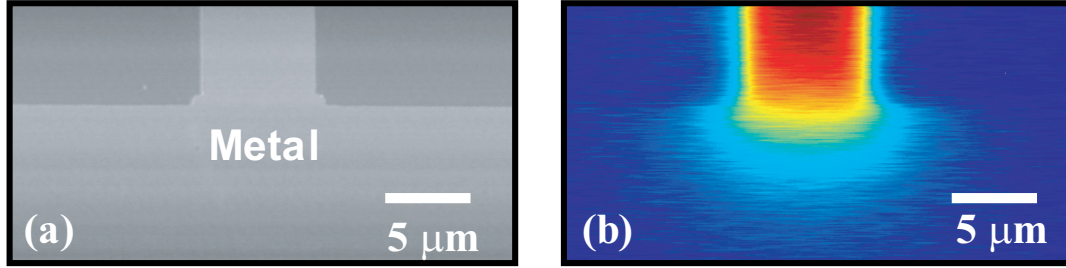
Figure 5.2: Topography (a), and expansion signal (b), of a constriction obtained using the Atomic Force Microscope (AFM) based Scanning Joule Expansion Microscopy (SJEM).

5.1.2 Heat generation and temperature rise

In this work, a closed-loop AFM (Asylum Research - MFP-3D) was used along with a digital and an RF lock-in amplifier (Stanford Research Systems - SR830 and SR844). The AFM scan rates were adjusted such that for each data point, at least 10 surface oscillations were detected by the AFM tip. This allows sufficient time for the lock-in to detect the particular frequency component.

Figure 5.2 shows the topography and the expansion signal on the constriction at 20 kHz heating frequency. Due to current continuity, the current density is much higher near the constriction and in the narrow line than in the wider line. Higher current density causes higher heat generation per unit volume, and if the thermal conductivity of the metal film is not too high, this heat generation variation results in a sensible temperature amplitude gradient near the constriction. Current crowding and the associated Joule heating is clearly captured in the present experiments. The following sections describe the numerical procedure to predict temperature amplitude variation near the constriction.

5.2 Thermal modeling in frequency space

A sinusoidal voltage signal in an interconnect results in a steady (DC), and a periodic (AC) heat generation. Since SJEM measures only the AC temperature amplitude,

significant computational effort can be saved by transforming the heat conduction equation into frequency or complex space. Consider the transient heat conduction equation

$$\rho c_P \frac{\partial T(\mathbf{r}, t)}{\partial t} = k\nabla^2 T(\mathbf{r}, t) + \dot{q}'''(\mathbf{r}, t) \tag{5.1}$$

with a time varying volumetric heat generation. If ω_h is the frequency of heat generation ($\omega_h = 2\omega$ where ω is the frequency of input voltage signal), periodic components of heat generation and temperature can be written as

$$T(\mathbf{r}, t) = (X(\mathbf{r}) + iY(\mathbf{r}))e^{i\omega_h t} \; ; \quad \dot{q}'''(\mathbf{r}, t) = q_o(\mathbf{r})e^{i\omega_h t} \tag{5.2}$$

where $X(\mathbf{r})$ and $Y(\mathbf{r})$ are respectively the real and imaginary parts of temperature amplitude, $q_o(\mathbf{r})$ is the spatially varying heat generation amplitude and $i = \sqrt{-1}$. With these substitutions, Eq. 5.1 leads to two steady coupled partial differential equations:

$$k\nabla^2 X(\mathbf{r}) + \rho c_P \omega_h Y(\mathbf{r}) + q_o(\mathbf{r}) = 0$$

$$k\nabla^2 Y(\mathbf{r}) - \rho c_P \omega_h X(\mathbf{r}) = 0 \tag{5.3}$$

These equations are solved using the traditional Finite Element Method (FEM).

A layout view of the computational domain along with the numerical grid is shown in Figure 5.3. The lengths L_a and L_b along the metal line are made long enough so that the results near the constriction are independent of these lengths. The temperature amplitude reaches a constant value corresponding to a two-dimensional case near the ends.

5.3 Effect of skin depth on heat generation

In steady state conditions, electric field can be obtained from a solution of the Poisson's equation for electric potential with a zero space charge. Ohm's law gives a relationship between electric field and current density once the electrical resistivity is
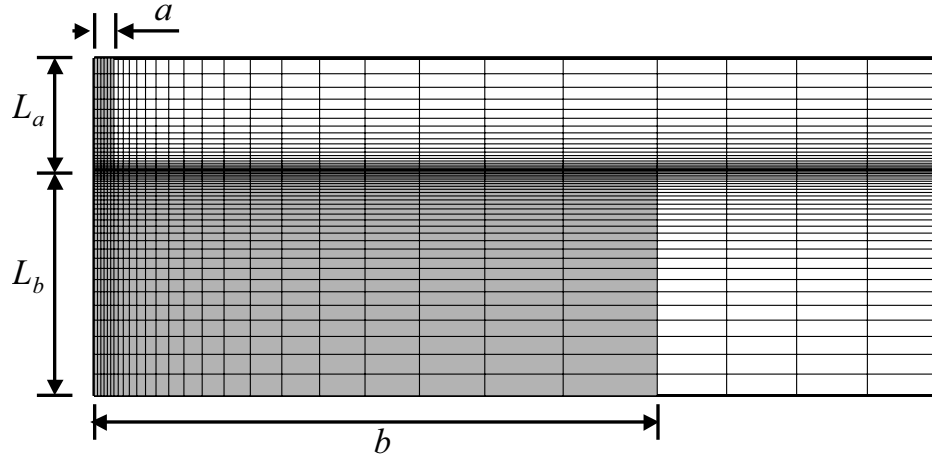
Figure 5.3: A schematic of computational domain and numerical grid.

known (see Jackson [38] for a good description of electrostatics and electrodynamics). Heat generation can then be calculated using the electric field and current density. The following set of equations fully describe a steady state scenario:

$$
\begin{aligned}
\nabla^2 V(\mathbf{r}) &= 0 \\
\mathbf{E}(\mathbf{r}) &= -\nabla V(\mathbf{r}) \\
\mathbf{j}(\mathbf{r}) &= \mathbf{E}(\mathbf{r})/\rho_e \\
\dot{q}'''(\mathbf{r}) &= j^2(\mathbf{r})\rho_e
\end{aligned} \tag{5.4}
$$

where V is the electric potential, $\mathbf{E}$ is the electric field, $\mathbf{j}$ is the current density, and ρ_e is the electrical resistivity. For an accurate description of transient cases, the complete set of Maxwell's electromagnetic equations should be considered [38]. These equations are coupled and are difficult to solve for an arbitrary conductor. For small frequencies this may not be necessary, as the skin depth becomes very large. Skin depth δ_s is given by ([38] and [28])

$$
\delta_s = \sqrt{\frac{2\rho_e}{\mu\omega}} \tag{5.5}
$$

where ω is the frequency of the input voltage signal. The effect of magnetic fields on current density and heat generation are negligible if the skin depth is much larger

than the conductor diameter. For a typical $\rho_e = 2.2\ \mu\Omega$-cm for gold, the skin depth is 333.8 μm at $\omega = 50$ kHz and 105.6 μm at $\omega = 500$ kHz. Skin effect may then be neglected for the smaller line width interconnect (7 μm wide) but it is not clear if it is negligible in the wider line (200 μm wide).

Ney [63] obtained an analytical solution for a constriction type structure including skin effect. The geometry is shown in the inset of Figure 5.4. It is assumed that the thickness into the plane of the paper is much smaller than all other dimensions and skin depth, which allows for a two-dimensional analysis. Normalized heat generation profiles for this structure are plotted in Figure 5.4 for several frequencies. Due to the fitting procedure used in thermal property extraction, normalized heat generation is sufficient for analysis. It is clear that significant deviations appear at very high frequencies but there is little difference between the profiles for 100 kHz and 1.0 MHz. The maximum frequency used in the present work is 500 kHz and it can thus be concluded that the effects of skin depth can be ignored.

Heat generation can now be calculated by assuming that the amplitudes of various quantities are given by Eq. 5.4. A typical heat generation profile and the associated temperature amplitude near the constriction are shown in Figure 5.5. The heating frequency is 150 kHz and the thermal conductivity of the metal film is assumed to be 82 W/mK. This value for the thermal conductivity is extracted by using the fitting procedure described in later sections. The figure shows two temperature profiles obtained using two different heat generation profiles. In the one-dimensional model, current density is assumed to be constant in each line but the total current is kept the same. This results in a heat generation profile with a step change near the constriction. The current crowding model involves solving the Poissons equation for voltage and calculating the heat generation using the electric field and current density 5.4. The temperature profiles in both cases are smooth near the constriction but are significantly different. The drop is much steeper for the one-dimensional model. In
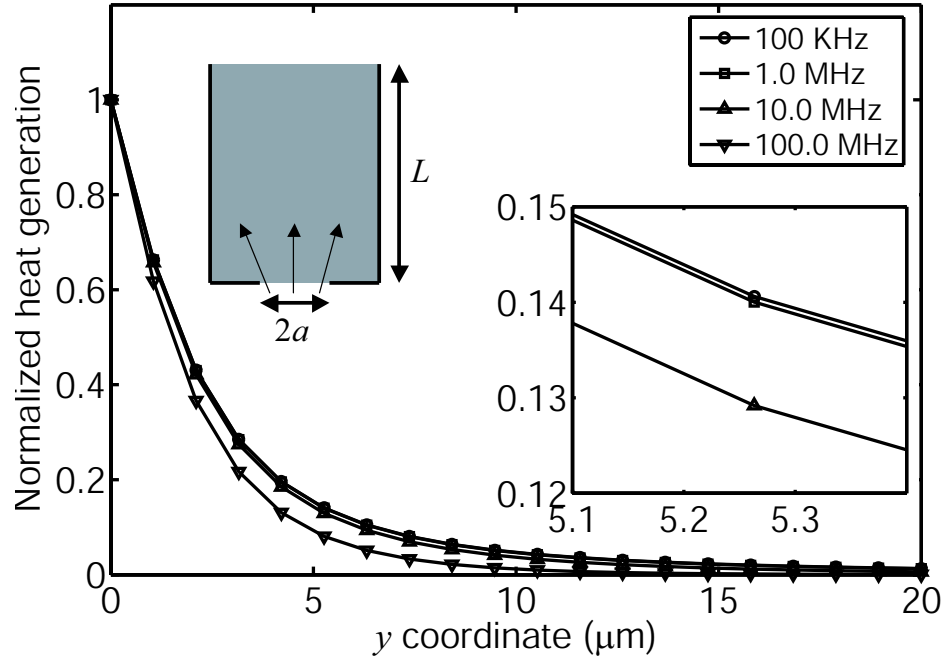
Figure 5.4: Effect of skin depth on heat generation profiles is shown for different frequencies. The inset zooms a portion of the plot to resolve lower frequencies. For the frequencies considered in this work, the skin effect can be neglected. It is assumed that $L \to \infty$.

both cases, far from the constriction, temperature amplitude reduces to that of a two-dimensional geometry with an infinitely long metal line of the same width. This study demonstrates that a detailed solution of Poisson's equation is necessary to obtain accurate temperature amplitude profiles.

5.4 Thermal conductivity extraction procedure

This section describes the thermal conductivity extraction procedure, using temperature amplitude profiles obtained at different heating frequencies. The thermal conductivity of silicon dioxide underneath the metal lines is important in the numerical model, and was measured using the 3ω method. Figure 5.6 shows the measured and predicted values for the temperature amplitude in the 3ω method. The thermal conductivity of silicon dioxide was measured in constriction - A wafer to be 1.16 ± 0.035
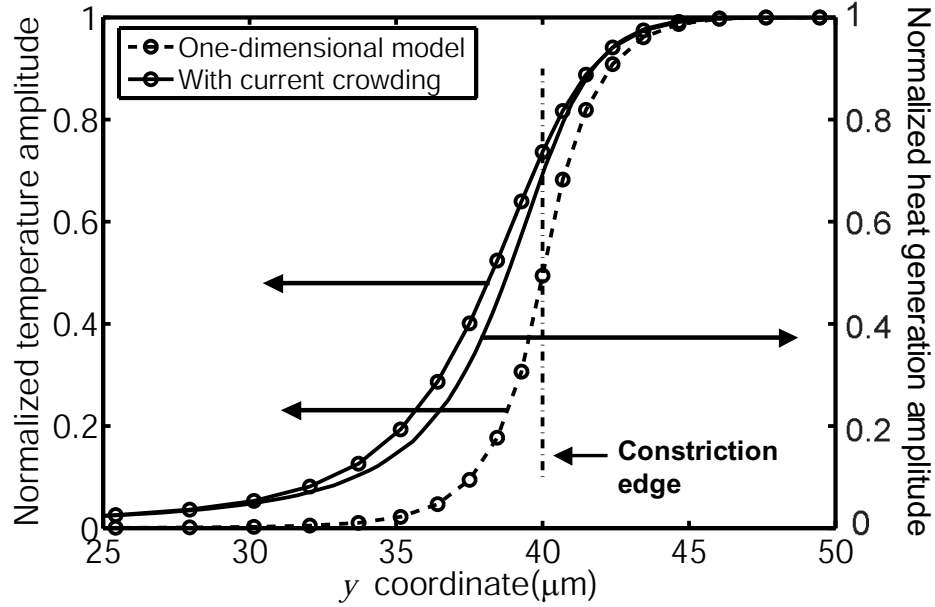
Figure 5.5: Temperature amplitude profiles along the centerline near the constriction. Normalized heat generation amplitude obtained from Poisson's equation for electric potential is also shown (current crowding model). Effect of current crowding is shown to significantly alter the profile near the constriction. In the one-dimensional model, current density is assumed to be constant in each line but the total current is kept the same.

W/mK, and in constriction - B wafer to be 1.00 ± 0.019 W/mK. These values are typical for chemical vapor deposited silicon dioxide films [42].

5.4.1 Effect of heating frequency

In a periodic heating case, as the frequency of heating is varied, the effect of thermal penetration depth appears. If the measurements are sufficiently accurate to observe this effect, thermal penetration depth, or the thermal conductivity can be extracted using appropriate analytical or numerical models, assuming the heat capacity is known. This effect is shown in Figure 5.7 in the constriction as the frequency is increased. Even though the spatial variation in heat generation is same for all the cases, both predicted and measured amplitudes clearly show a frequency dependent
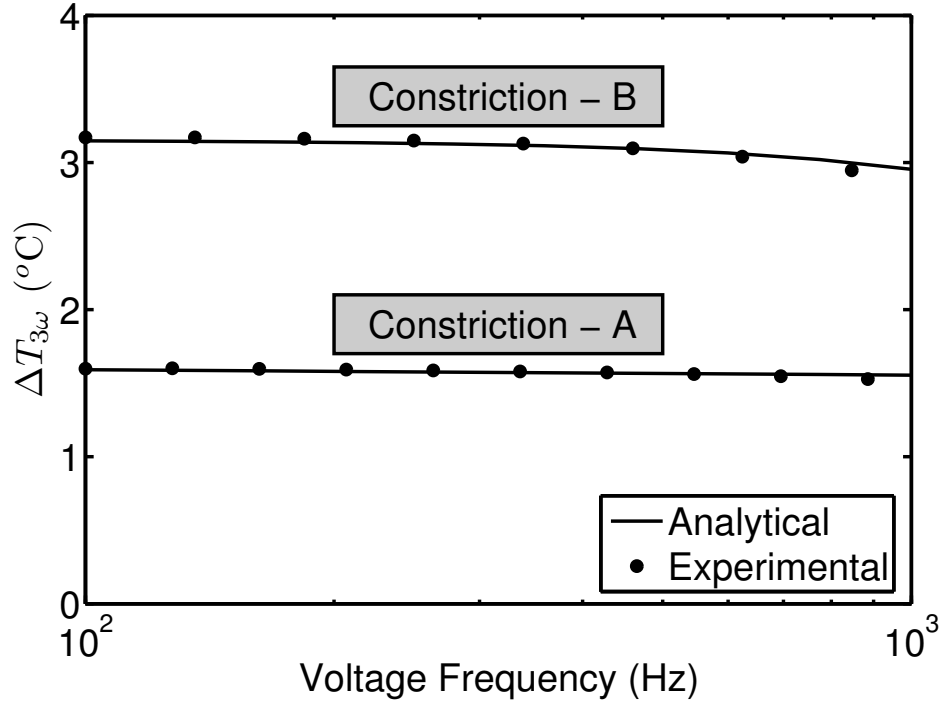
Figure 5.6: Temperature amplitude in the 3ω experiments, which is used to measure thermal conductivity of silicon dioxide.

structure. As the frequency increases, thermal penetration depth within the film reduces, and the amplitude drops much more steeply near the constriction. In the limit that the penetration depth is zero, the expansion amplitude will be similar to the heat generation amplitude. This effect is clearly seen at 1000 kHz. Noise levels gradually increase as the frequency is increased to 1000 kHz. Thermal expansion amplitude continuously reduces as the frequency increases.

This investigation shows that frequency dependent structure can be captured by SJEM on a constriction. This can allow for thermal conductivity extraction of thin films. This procedure is described in the following section.

5.4.2 Numerical fit to measurements

Calculation of temperature amplitude from the expansion signal requires considerable information about the underlying layers. In order to deduce temperature amplitude
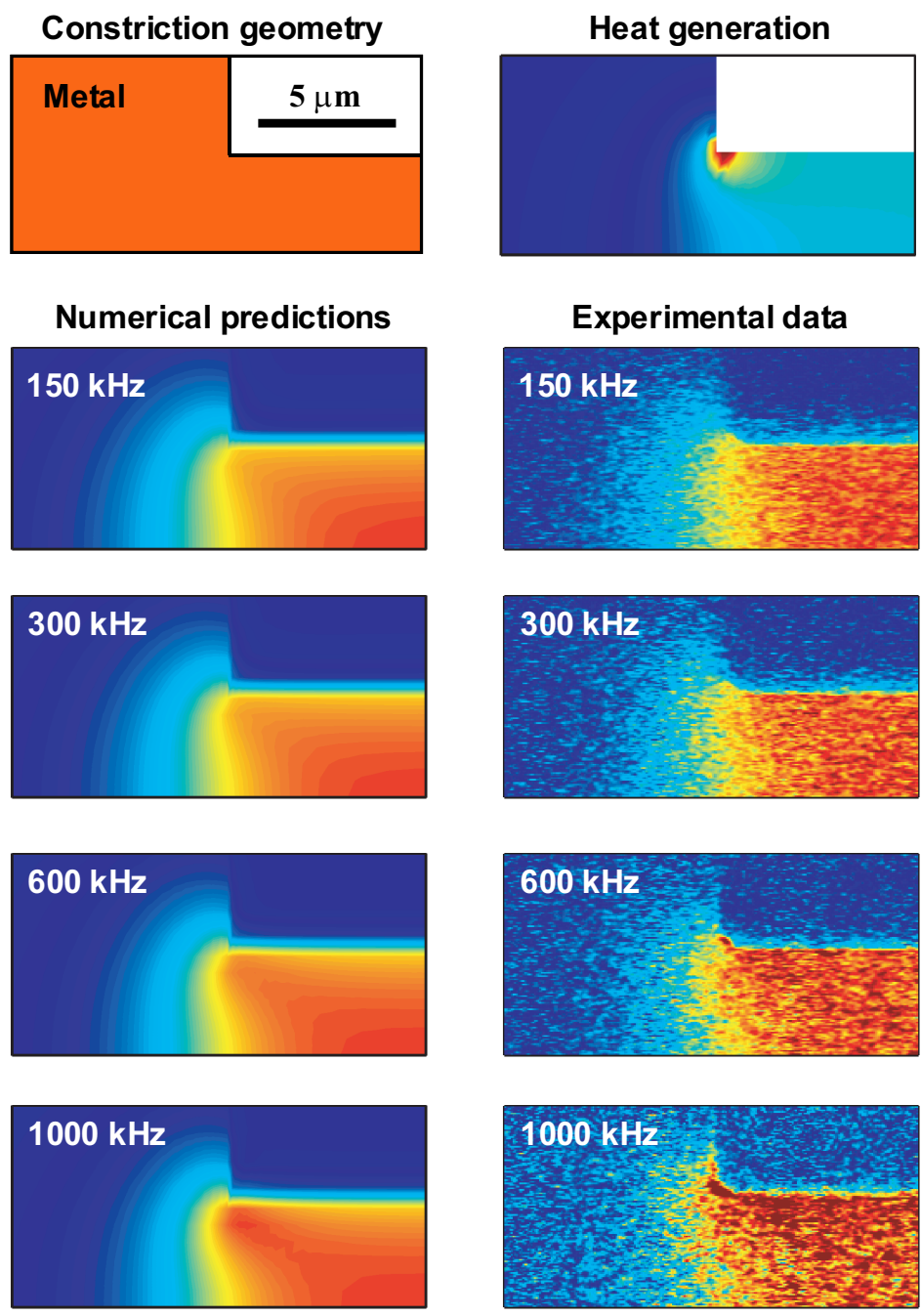
Figure 5.7: A comparison of numerical and experimental expansion amplitudes as the frequency is varied. The effect of penetration depth is clearly seen in the images

from the expansion amplitude, the coefficient of thermal expansion (CTE) and thickness of all the underlying layers that contribute to the expansion signal must be known. In the present structure, the CTEs of metal line and parylene are much larger than the underlying oxide and silicon substrate. Since the thermal conductivity of gold is high, temperature across the thickness of the metal line is constant. It can be assumed that the temperature across parylene is also constant, since the thickness is much smaller than the thermal penetration depth. If one ignores temperature dependence of properties, then the temperature amplitude and expansion signal are linearly proportional. The contribution of the underlying layers (silicon dioxide and silicon substrate) to the expansion signal diminishes as the frequency increases. Higher frequencies diminish the effect of far-field conditions. Detailed comparison of numerical and experimental results are made for 100, 150, and 200 kHz heating frequencies, and a technique to measure metal thermal conductivity is briefly outlined in the following paragraphs.

A simple minimization procedure is used to find the proportionality constant between the expansion signal and temperature amplitude. If $E(x, y)$ is the expansion signal, then $T_{exp}(x, y) = \alpha E(x, y)$, where α is the unknown proportionality constant. For a given temperature amplitude $T_{num}(x, y)$ obtained from numerical simulations, α is obtained by minimizing the mean square error. Temperature amplitude profile on the centerline of metal lines is averaged over a micron across the width and is used in this fitting procedure.

The error after obtaining the best α for different values of metal thermal conductivity is shown in Figure 5.8 for 100, 150, and 200 kHz heating frequency. It is clear that a good fit is obtained for metal thermal conductivity near 82.0 W/mK. The numerical and experimental temperature amplitude profiles for the best fit for $k_m = 82$ W/mK are shown in Figure 5.9. The agreement appears good over almost the entire region. Although gold has a bulk thermal conductivity of 318 W/mK at
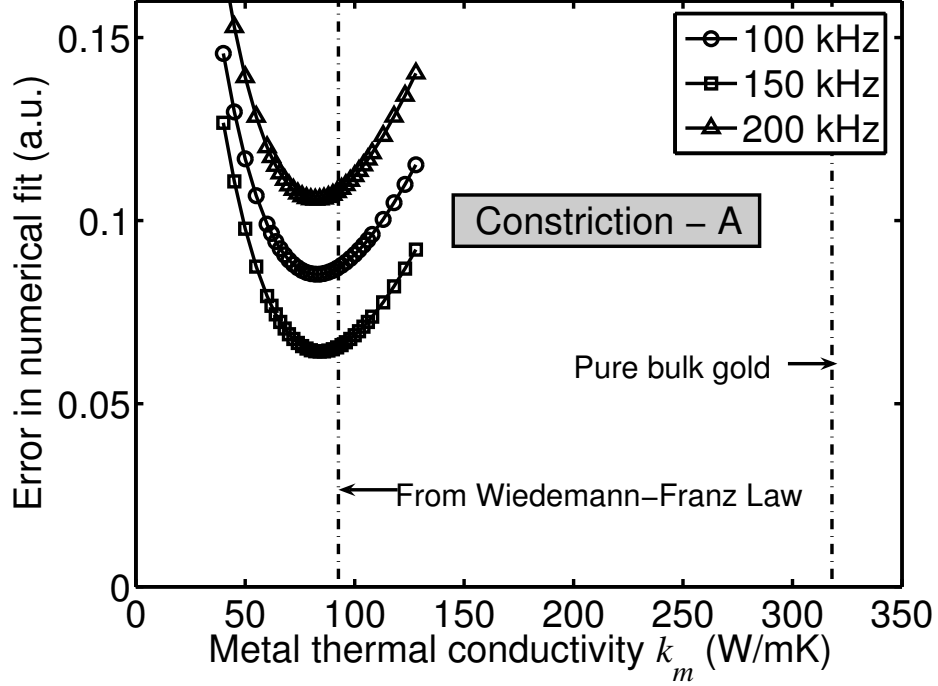
Figure 5.8: Error in numerical fit at different frequencies as the thermal conductivity of metal film is varied for constriction - A.

room temperature, thin films of thickness comparable to mean free path are known to have much lower thermal conductivity due to enhanced electron surface scattering [27]. The fit value of thermal conductivity thus appears reasonable for the 43 nm thick film (constriction - A) used in the present investigation.

It is well known that electrical and thermal conductivity of bulk metals are approximately related by the Wiedemann-Franz Law [4], according to which,

$$\frac{\kappa_{film}}{\sigma_{film}T} = L_o \tag{5.6}$$

where σ_{film} is the electrical conductivity, κ_{film} is the thermal conductivity, T is the temperature and L_o is the Lorenz number [4] (see the discussion in Chapter 2). Based on electrical resistance measurements, the electrical resistivity of the line was found to be 7.52 mW-cm. Using 2.32×10^{-8} WΩ/K^2 for the Lorenz number of gold results in a thermal conductivity of 92.55 W/mK for the metal line. This value is close to the extracted value of 82 W/mK as it should be expected. It thus appears that a
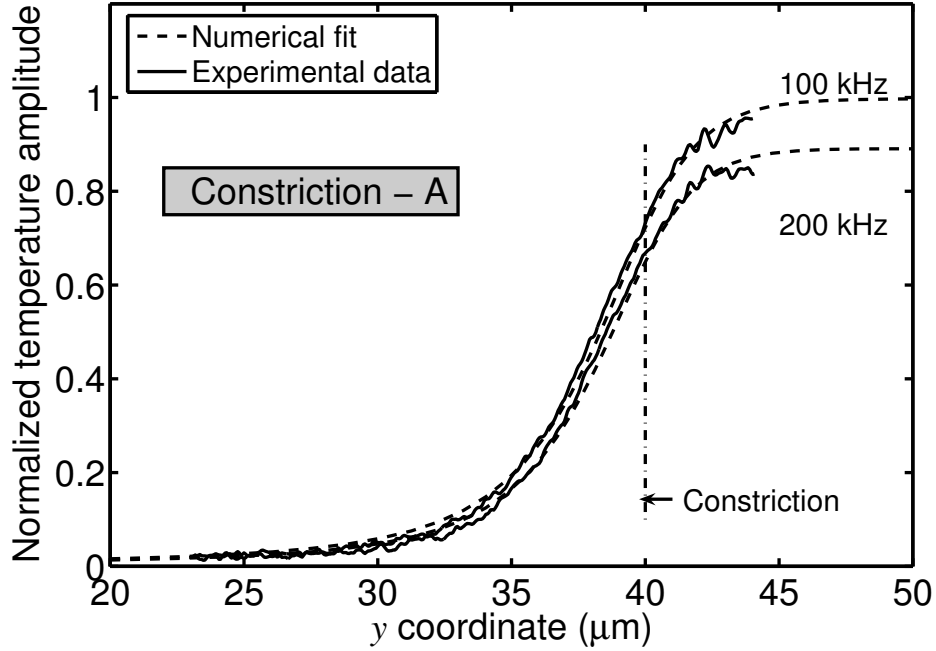
Figure 5.9: Comparison of experimental and numerical temperature amplitude profiles along the centerline near the constriction after minimizing the error in numerical fit.

constriction in a thin metal film characterized through SJEM in conjunction with the 3ω method, can enable in-plane thermal conductivity measurements of thin films and interconnects in the sub-100 nm range. The technique does not require extensive microfabrication since freestanding metal films are not necessary.

Measurements were also made on constriction - B and are summarized in Figures 5.10 and 5.11. This structure lacks parylene coating, but the signal-to-noise ratio is still good due to large oxide layer underneath the metal layer. Thicker oxide results in larger temperature amplitude. The thickness of this structure is 131 nm and is about three times the mean free path of electrons. The thermal conductivity is about twice that of the constriction - A film. Once again, the extracted thermal conductivity is close to that predicted by Wiedemann-Franz Law. The obtained temperature profiles at the best fit follow the measurements very closely. Thicker metal film implies lesser surface scattering effect, and the temperature profiles are much flatter than in the
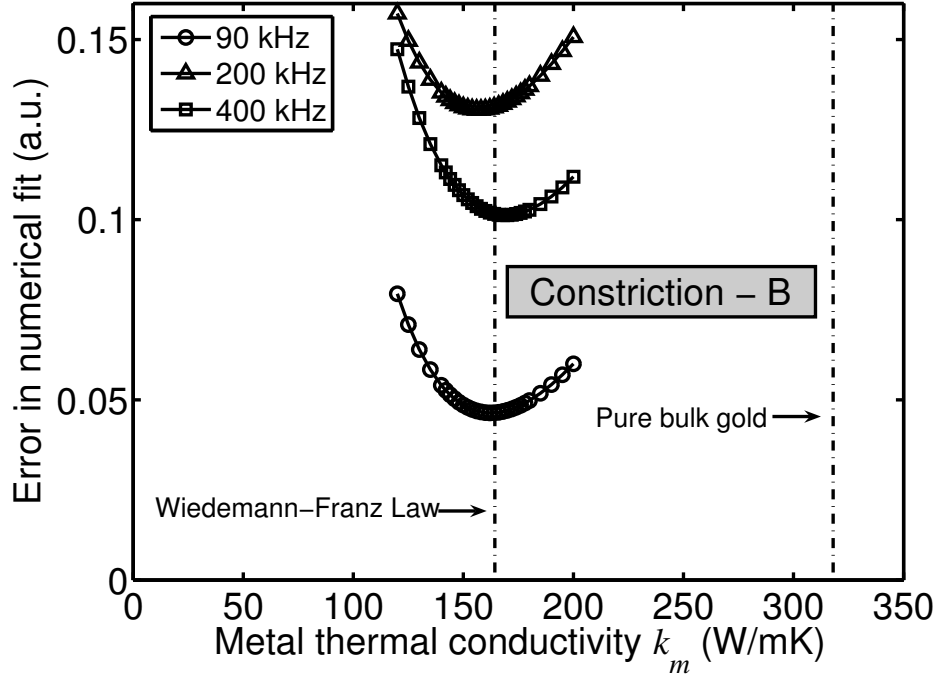
Figure 5.10: Error in numerical fit at different frequencies as the thermal conductivity of metal film is varied for constriction - B.

constriction - A case. This investigation further demonstrates the proposed technique.

5.5 Thermomechanical analysis of expansion amplitude

SJEM measures only the expansion amplitude of the surface. This amplitude is in general a complex function of temperature, thermophysical, and mechanical properties. It is assumed in the thermal conductivity extraction procedure, that the expansion amplitude is linearly proportional to temperature amplitude. This assumption is examined by performing a detailed deformation analysis of a two-dimensional structure.

It is convenient to use Einstein notation to describe the governing dynamical equation (see [57] for a detailed derivation of the equations). Let u_i be the displacement vector (i takes the values 1, 2 and 3 corresponding to x, y and z directions). The
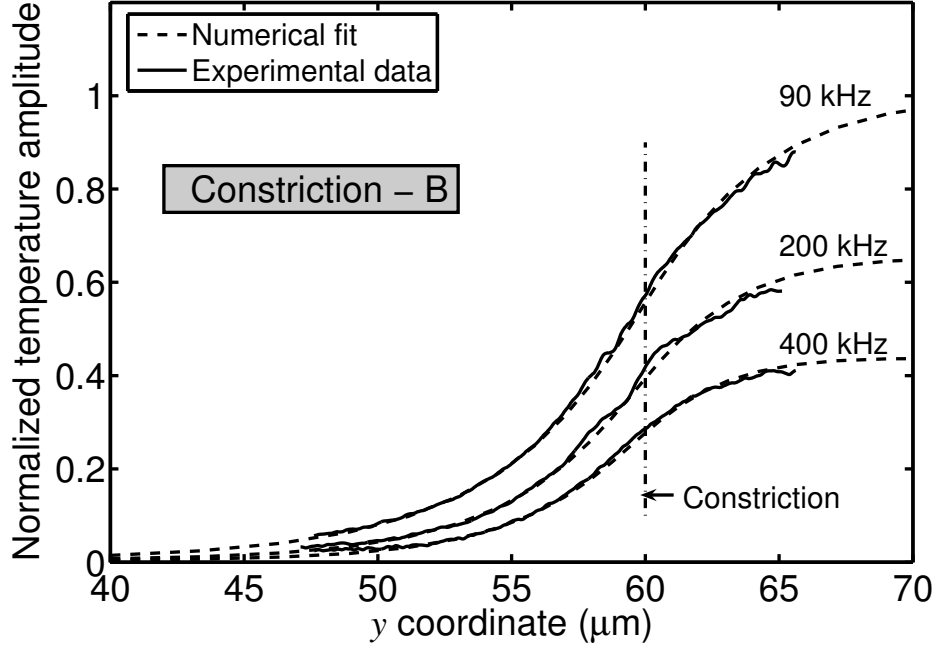
Figure 5.11: Comparison of experimental and numerical temperature amplitude profiles along the centerline near the constriction after minimizing the error in numerical fit.

strain tensor components ϵ_{ij} are given as

$$\epsilon_{ij} = \frac{1}{2}(u_{i,j} + u_{j,i}) \tag{5.7}$$

where $u_{i,j}$ stands for the partial derivative of u_i with respect to j coordinate. Within the framework of linear thermoelasticity, a constitutive equation between the stress tensor σ_{ij} and strain tensor is given by

$$\sigma_{ij} = \frac{E}{(1+\nu)(1-2\nu)}\left[\nu\delta_{ij}\epsilon_{kk} + (1-2\nu)\epsilon_{ij}\right] - \frac{E}{(1-2\nu)}\alpha(T-T_o)\delta_{ij} \tag{5.8}$$

where E is the Young's modulus, ν is the Poisson's ratio, α is the Coefficient of Thermal Expansion (CTE), T is the temperature, T_o is the reference temperature, and δ_{ij} is the Kronecker delta. The dynamical equation is derived by applying Newton's second law to a differential volume element:

$$\rho\ddot{u}_i = \sigma_{ij,j} + \rho b_i \tag{5.9}$$

where ρ is the density, b_i is a volumetric body force such as that due to gravity, and the dots denote second order partial derivative with respect to time. Using Eq. 5.8 for the stress tensor results in the following dynamical equation, known as the *Navier's equation*.

$$\rho\ddot{u}_i = \frac{E}{2(1+\nu)}u_{i,jj} + \frac{E}{2(1+\nu)(1-2\nu)}u_{j,ij} - \frac{E\alpha}{(1-2\nu)}T_{,i} + \rho b_i \qquad (5.10)$$

The above equation is transformed into frequency space since only the expansion amplitude is required. Assuming $u_i = u_i^* e^{i\omega_h t}$ and $T = T^* e^{i\omega_h t}$, where the superscript '*' implies a complex function of space, and ignoring body forces results in

$$-\rho\omega_h^2 \ddot{u}_i^* = \frac{E}{2(1+\nu)}u_{i,jj}^* + \frac{E}{2(1+\nu)(1-2\nu)}u_{j,ij}^* - \frac{E\alpha}{(1-2\nu)}T_{,i}^* \qquad (5.11)$$

If the temperature field is known, this equation can be solved for the expansion amplitude u_i^*.

A two-dimensional analysis of a long metal line is performed to verify the validity of a linear relation between the expansion amplitude and temperature amplitude. In this case, a plane strain assumption is made to reduce the computational cost. In a plane strain assumption, ϵ_{zz}, ϵ_{yz}, and ϵ_{zx} are assumed to be zero. A schematic of the simulated half metal line structure is shown in the inset of Figure 5.12 (half metal line is sufficient due to symmetry). The vertical plane at $x = 0$ is allowed to move only in the vertical direction. The problem is solved in FEMLAB which allows for easy coupling of different equations. The temperature amplitude is calculated by the solution of heat conduction equation in the frequency space, which is then used as an input for deformation modeling. The mechanical properties used for the simulation are shown in Table 5.2. These are typical values available from the literature.

Expansion amplitude and temperature amplitude on the surface of the structure until the edge of metal width is plotted in Figure 5.12 for $\omega_h = 100$ kHz. If the relationship between them is linear, the two curves should coincide. It is apparent that the linearity assumption fails as one approaches the edges of the metal line. This
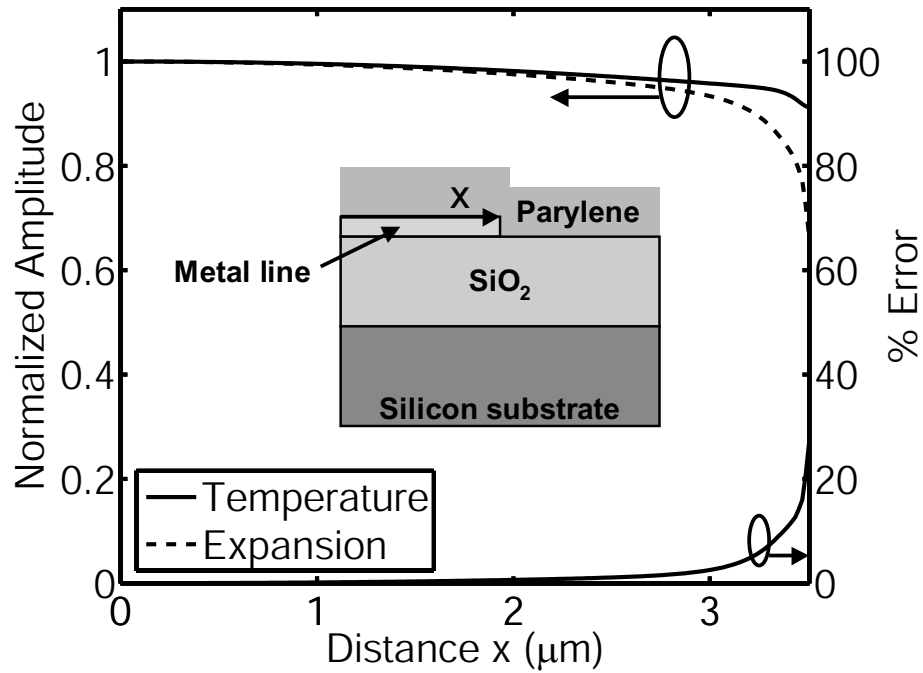
Figure 5.12: Comparison of expansion amplitude and temperature amplitude over the metal line. The two-dimensional structure modeled under the plane strain assumption is shown in the inset.
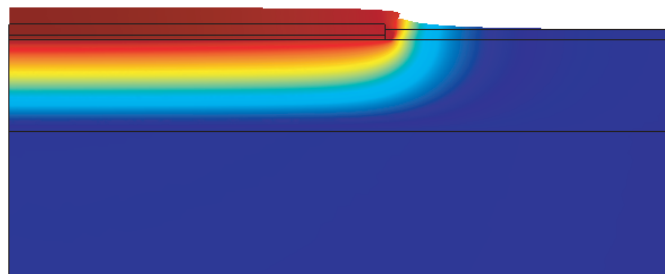
Figure 5.13: Deformation amplitude is shown by the displaced structure. Temperature amplitude is plotted using color shading. The deformation is artificially scaled by a large factor for clarity.

Table 5.2: Mechanical properties used for thermomechanical simulation

Material	Young's modulus E (GPa)	Poisson's ratio ν	CTE α (ppm/K)	Density ρ (kg/m^3)
Silicon	97.68	0.278	2.62	2329
Silicon dioxide	59.0	0.24	1.0	2185
Gold	80.12	0.423	14.29	18880
Parylene	3.2	0.4	35.0	1289

is primarily due to large CTE mismatch between the metal and underlying oxide layer. The percentage error is also shown in the same plot. This is not a serious concern since the thermal conductivity extraction procedure uses expansion amplitude only along the center line of the metal line. The deformation of the structure is depicted in Figure 5.13 along with the temperature amplitude over the cross-section. The deformation is arbitrarily scaled to a much larger value for clarity. Due to large heating frequency, the temperature amplitude is appreciable only in the oxide layer close to the metal line.

5.6 Uncertainty analysis

The thermal conductivity values extracted in this chapter depend on several parameters such as, metal line width, metal thickness, oxide thermal conductivity and so on. Uncertainties in these parameters propagate into the measured thermal conductivity of the metal line. A general procedure to account for these uncertainties was given by Kline and McClintock [47]. Let the final measured value y be a function of N parameters $(x_1, x_2, ..., x_N)$. These parameters in turn have uncertainties $(u_1, u_2, ..., u_N)$. The final uncertainty u_y in the parameter y is then given by

$$u_y = \sqrt{\left(\frac{\partial y}{\partial x_1}u_1\right)^2 + \left(\frac{\partial y}{\partial x_1}u_2\right)^2 + \ldots + \left(\frac{\partial y}{\partial x_N}u_N\right)^2} \qquad (5.12)$$

Table 5.3: Uncertainty analysis for oxide thermal conductivity in Constriction - A

Parameter	Nominal value	Deviation	% change in k_{ox} for $+ u_i$
Metal half width (a)	3.5 μm	$\pm$ 0.05 μm	$-$ 1.3
Oxide thickness (d_{ox})	849 nm	$\pm$ 5 nm	$+$ 0.5
TCR (α_T)	1.678×10^{-3} /^{o}C	$\pm$ 0.035×10^{-3} /^{o}C	$+$ 2.3
Input voltage (V_{in})	4.246 V	$\pm$ 1 mV	$+$ 0.1
Silicon thermal conductivity (k_{Si})	148 W/mK	$\pm$ 7.4 W/mK	$-$ 0.4
Silicon heat capacity (C_{Si})	1.66×10^6 J/m^3	$\pm$ 0.08×10^6 J/m^3	$-$ 0.1
3ω voltage $(V_{3\omega})$	2.68 mV	$\pm$ 0.03 mV	$-$ 1.1
Oxide thermal conductivity k_{ox}	**1.16 W/mK**	**$\pm$ 0.035 W/mK**	**$\pm$ 3 %**

This expression is used in arriving at the uncertainties in the oxide thermal conductivity and extracted metal thermal conductivity. Tables 5.3 and 5.4 list the uncertainties in various parameters and their effect on the measured oxide thermal conductivity for the structures. Extracted metal thermal conductivity in turn depends on oxide thermal conductivity as well as other parameters. An analysis of these uncertainties for Constriction - A structure at 100 kHz heating frequency and Constriction - B structure at 90 kHz heating frequency are shown in Tables 5.5 and 5.6 respectively. The uncertainty in both cases is about $\pm$ 10 %.

A summary of all the measurements is shown in Figure 5.14. In both the structures, measured values are close to that obtained from Wiedemann-Franz Law for the same structures. These are much smaller than bulk values. Also, as expected, the 43 nm film has much smaller conductivity than the 131 nm film. These results demonstrate the applicability of the proposed technique.

Table 5.4: Uncertainty analysis for oxide thermal conductivity in Constriction - B

Parameter	Nominal value	Deviation	% change in k_{ox} for $+ u_i$
Metal half width (a)	3.1 μm	$\pm$ 0.07 μm	$-$ 1.1
Oxide thickness (d_{ox})	7.72 μm	$\pm$ 10 nm	$+$ 0.1
TCR (α_T)	2.176×10^{-3} /^{o}C	$\pm$ 0.022×10^{-3} /^{o}C	$+$ 1.1
Input voltage (V_{in})	4.05 V	$\pm$ 1 mV	$+$ 0.1
Silicon thermal conductivity (k_{Si})	148 W/mK	$\pm$ 7.4 W/mK	$-$ 0.4
Silicon heat capacity (C_{Si})	1.66×10^6 J/m^3	$\pm$ 0.08×10^6 J/m^3	$< -$ 0.1
3ω voltage $(V_{3\omega})$	6.985 mV	$\pm$ 0.07 mV	$-$ 1.0
Oxide thermal conductivity k_{ox}	**1.00 W/mK**	**$\pm$ 0.019 W/mK**	**$\pm$ 1.9 %**

Table 5.5: Uncertainty analysis for extracted metal thermal conductivity in Constriction - A at 100 kHz heating frequency

Parameter	Nominal value	Deviation	% change in k_m for $+ u_i$
Metal half width (a)	3.5 μm	$\pm$ 0.05 μm	4.9
Metal thickness (h)	43.4 nm	$\pm$ 1.2 nm	2.4
Oxide thermal conductivity k_{ox}	1.16 W/mK	$\pm$ 0.035 W/mK	2.4
Constriction location	-	$\pm$ 0.06 μm	7.3
Metal thermal conductivity k_m	**82 W/mK**	**$\pm$ 7.7 W/mK**	**$\pm$ 9.4 %**

Table 5.6: Uncertainty analysis for extracted metal thermal conductivity in Constriction - B at 90 kHz heating frequency

Parameter	Nominal value	Deviation	% change in k_m for $+ u_i$
Metal half width (a)	3.1 μm	$\pm$ 0.07 μm	8.6
Metal thickness (h)	131.3 nm	$\pm$ 3.5 nm	4.9
Oxide thermal conductivity k_{ox}	1.00 W/mK	$\pm$ 0.019 W/mK	1.2
Constriction location	-	$\pm$ 0.04 μm	2.5
Metal thermal conductivity k_m	**162 W/mK**	**$\pm$ 16.7 W/mK**	**$\pm$ 10.3 %**
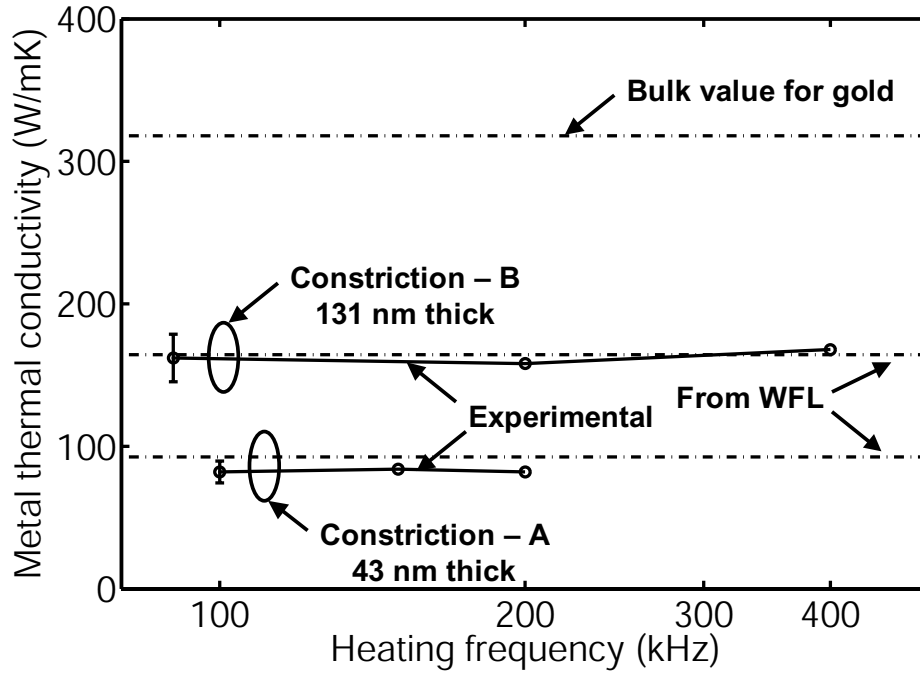
Figure 5.14: A summary of the extracted thermal conductivities for two constrictions and their comparison with bulk value and Wiedemann-Franz Law (WFL) predictions.

CHAPTER VI

AN IMPROVED SOLUTION FOR THE 3ω METHOD OF THERMAL CONDUCTIVITY MEASUREMENTS

In this chapter, a new semi-analytical solution for the 3ω method is derived and investigated. Thermal conduction within the metal heater is resolved. This solution can be applied for a general multilayer anistropic stack.

6.1   Earlier boundary conditions

In the earlier 3ω solutions [15], it was assumed that heat enters uniformly across the width of the metallic heater. This assumption is exact only when the metal thermal conductivity is close to zero. In general, the thermal conductivity of the metal heater can be up to three orders of magnitude higher than the underlying dielectric film. A complete system of metal line and the film can be solved for AC temperature rise. Figure 6.1 shows the heat flux profiles below the metal heater for such a structure. A uniform heat generation is prescribed within the metal heater. The structure is a copper heater on top of silicon dioxide. It is clear that the assumption of uniform heat flux breaks down near the edges. There is a small frequency dependence due to variation in thermal penetration depth within the metal line. This plot shows that the effect of thermal conduction within the heater should be considered for accurate 3ω measurements. The following section describes a semi-analytical solution to incorporate this effect.
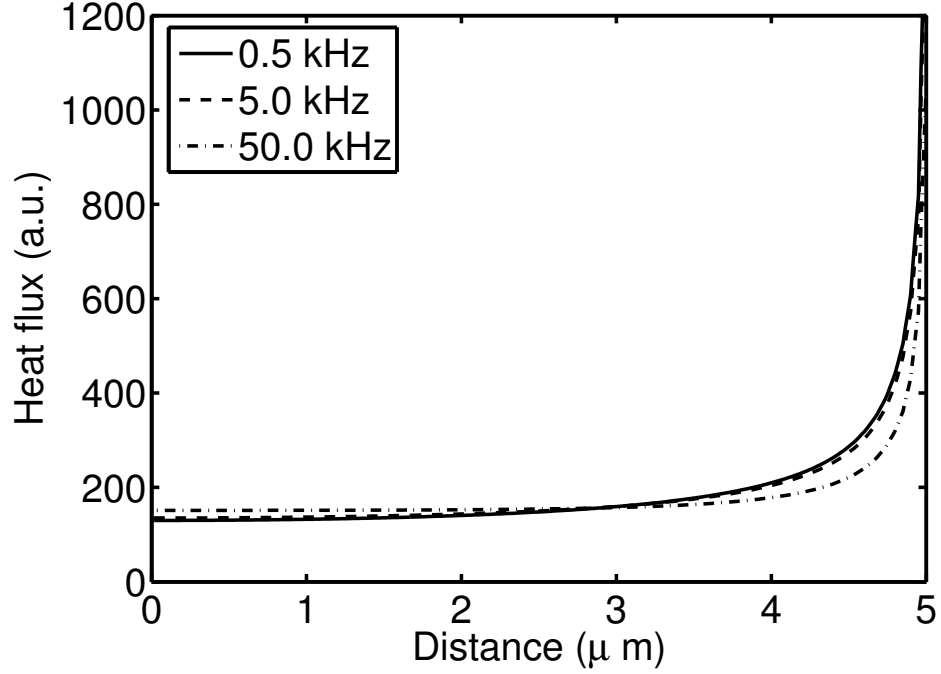
Figure 6.1: Heat flux variation below the heater line

6.2 Derivation of the semi-analytical solution

A schematic of the structure considered in the analysis is shown in Figure 6.2. The analytical development is described in detail for this single film structure. An arbitrary case of multilayer structure with anisotropic thermal conductivity can be solved in a similar manner. The two-dimensional transient heat conduction equation without any volumetric heat generation is given by

$$\frac{\partial T}{\partial t} = \alpha \left(\frac{\partial^2 T}{\partial x^2} + \frac{\partial^2 T}{\partial y^2} \right) \tag{6.1}$$

Since only the oscillating component of temperature is required, the above equation is transformed into frequency space by choosing

$$T(x, y, t) = F(x, y)e^{i\omega_h t} \tag{6.2}$$
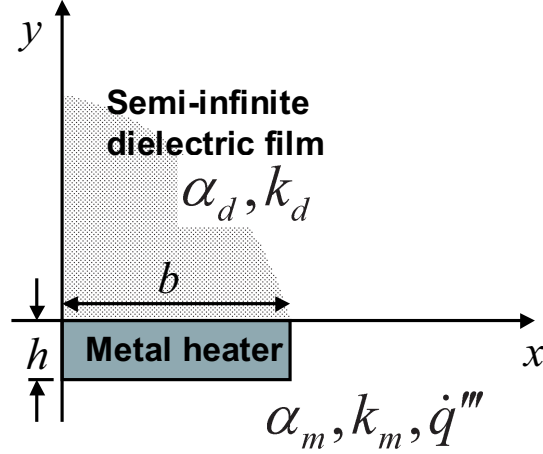
Figure 6.2: A schematic of the semi-infinite film case.

where $F(x, y)$ is a complex function and ω_h is the heating frequency. Equation (6.1) then reduces to

$$\left(\frac{\partial^2 F}{\partial x^2} + \frac{\partial^2 F}{\partial y^2} \right) = \left(\frac{i\omega_h}{\alpha} \right) F \tag{6.3}$$

Using separation of variables so that $F(x, y) = X(x)Y(y)$, the following equations arise for each eigenvalue λ

$$\frac{d^2 X}{dx^2} = -\lambda^2; \quad \frac{d^2 Y}{dy^2} = l^2 \text{ where } l = \sqrt{\lambda^2 + q^2} \text{ and } q = \sqrt{\frac{i\omega_h}{\alpha}} \tag{6.4}$$

6.2.1 Dielectric region solution

Consider Eq. (6.4) for the dielectric region. The general solutions for the x and y directions are given as

$$X(x) = A(\lambda_d) \cos \lambda_d x + B(\lambda_d) \sin \lambda_d x \tag{6.5}$$

$$Y(y) = C(\lambda_d) \exp\left[-l_d y\right] + D(\lambda_d) \exp\left[+l_d y\right] \tag{6.6}$$

where subscript d stands for dielectric. Symmetry condition at $x = 0$ and bounded behavior for $y \to \infty$ requires $B(\lambda_d)$ and $D(\lambda_d)$ to vanish respectively. The general solution will then be a superposition of solutions for each eigenvalue. Absorbing $C(\lambda_d)$

in $A(\lambda_d)$ results in

$$F_d(x, y) = \int_0^\infty A(\lambda_d) \cos \lambda_d x \exp\left[-l_d y\right] d\lambda_d \tag{6.7}$$

6.2.2 Metal region solution

For the metal region, the general solution for the x and y directions are given as (assuming heat generation is zero momentarily)

$$X(x) = A(\lambda_m) \cos \lambda_m x + B(\lambda_m) \sin \lambda_m x \tag{6.8}$$

$$Y(y) = C(\lambda_m) \exp\left[-l_m y\right] + D(\lambda_m) \exp\left[+l_m y\right] \tag{6.9}$$

Symmetry condition at $x = 0$ requires $B(\lambda_m)$ to vanish. Adiabatic condition at $x = b$ results in discrete eigenvalues:

$$\left.\frac{dX}{dx}\right|_{x=b} = -A(\lambda_m)\lambda_m \sin \lambda_m x = 0 \text{ implies } \lambda_m^{(n)} = \frac{n\pi}{b}; \ n = 0, 1, 2... \tag{6.10}$$

The general solution including heat generation can be written as

$$F_m(x, y) = \frac{\dot{q}'''}{k_m q_m^2} + \sum_{n=0}^\infty \left(C_n \exp\left[-l_m^{(n)} y\right] + D_n \exp\left[+l_m^{(n)} y\right]\right) \cos \lambda_m^{(n)} x \tag{6.11}$$

6.2.3 Other boundary conditions

Applying adiabatic boundary condition at $y = -h$ for $0 < x < b$, results in

$$-k_m \left.\frac{\partial F_m}{\partial y}\right|_{y=-h} = \sum_{n=0}^\infty k_m l_m^{(n)} \left(C_n \exp\left[+l_m^{(n)} h\right] - D_n \exp\left[-l_m^{(n)} h\right]\right) \cos \lambda_m^{(n)} x = 0 \tag{6.12}$$

Using Fourier series theory, a general relation can be found between the coefficients:

$$D_n = C_n \exp\left[+2l_m^{(n)} h\right] \tag{6.13}$$

Temperature and heat flux must be continuous at the interface for $0 < x < b$ and, for $b < x < \infty$, the heat flux should vanish. The heat flux condition on the dielectric surface at $y = 0$ for $0 < x < \infty$ is then

$$-\left[H(x) - H(x - b)\right] k_m \left.\frac{\partial F_m}{\partial y}\right|_{y=0} = -k_d \left.\frac{\partial F_d}{\partial y}\right|_{y=0} \tag{6.14}$$

where $H(x)$ is the Heaviside function. Substituting for the metal and dielectric solutions (Eqs. (6.7) and (6.11)) results in

$$\sum_{n=0}^{\infty} k_m l_m^{(n)} (C_n - D_n) [H(x) - H(x-b)] \cos \lambda_m^{(n)} x = \int_0^{\infty} k_d l_d A(\lambda_d) \cos \lambda_d x d\lambda_d \quad (6.15)$$

Using the following identity and the usual Fourier series/transform theory,

$$\int_0^b \cos \lambda_d x \cos \lambda_m^{(n)} x dx = \frac{(-1)^n \lambda_d \sin \lambda_d b}{(\lambda_d)^2 - (\lambda_m^{(n)})^2} \quad (6.16)$$

an expression for $A(\lambda_d)$ can be obtained in terms of C_n after using Eq. (6.13):

$$A(\lambda_d) = \sum_{n=0}^{\infty} \frac{(-1)^n 2 k_m l_m^{(n)} (1 - \exp[+2l_m^{(n)}h])}{\pi k_d l_d} \frac{\lambda_d \sin \lambda_d b}{(\lambda_d)^2 - (\lambda_m^{(n)})^2} C_n \quad (6.17)$$

Finally, the temperature matching condition at the interface leads to

$$(C_n + D_n) = \frac{(-1)^n (2 - \delta_{0,n})}{b} \int_0^{\infty} \frac{A(\lambda_d) \lambda_d \sin \lambda_d b}{(\lambda_d)^2 - (\lambda_m^{(n)})^2} d\lambda_d - \delta_{0,n} \frac{\dot{q}'''}{k_m q_m^2} \quad (6.18)$$

An infinite set of simultaneous equations for C_n arise when Eqs. (6.13) and (6.16) are used to eliminate D_n and $A(\lambda_d)$ respectively. The infinite set of simultaneous equations can be written in a matrix form:

$$[a] \{C\} = \{q\} \quad (6.19)$$

where $[a]$ is the square coefficient matrix, $\{C\}$ is the column vector of coefficients and $\{q\}$ is a column vector involving source terms. The terms in the matrices are

$$a_{ij} = \delta_{i,j}(1 + \exp[+2l_m^{(i)}h]) +$$
$$\int_0^{\infty} \frac{(-1)^{i+j+1} 2 k_m l_m^{(j)} (2 - \delta_{0,j})(1 - \exp[+2l_m^{(j)}h]) \lambda_d^2 \sin^2 \lambda_d b}{\pi k_d l_d b [(\lambda_d)^2 - (\lambda_m^{(i)})^2][(\lambda_d)^2 - (\lambda_m^{(j)})^2]} d\lambda_d \quad (6.20)$$

$$q_i = -\delta_{0,i} \frac{\dot{q}'''}{k_m q_m^2} \quad (6.21)$$

It is only necessary to retain sufficient number of terms to obtain accurate average temperature rise. About 10 to 20 equations generally give very accurate results.
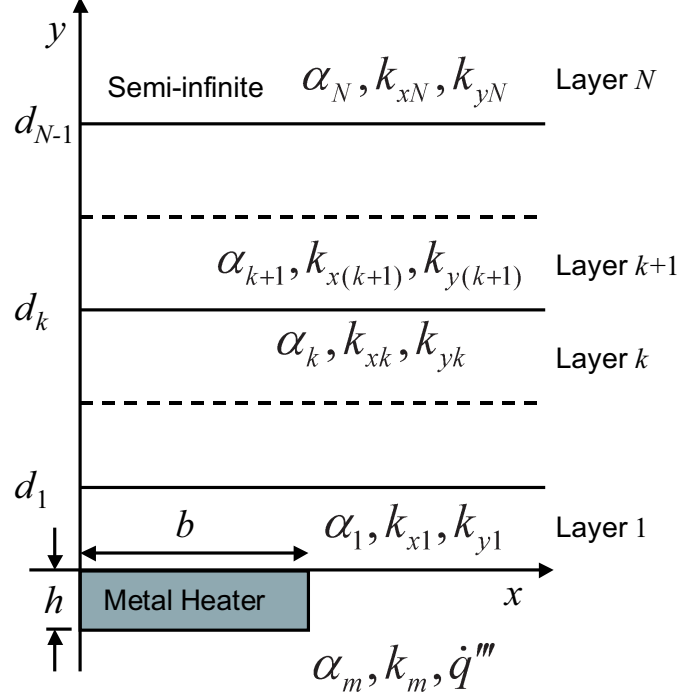
Figure 6.3: A schematic of the multilayer anisotropic stack.

A general solution for a multilayer structure with anisotropic thermal conductivities can also be derived by following the above described steps. This structure is shown in Figure 6.3 along with the nomenclature used in the solution. Here, k_{yk} is the cross-plane, and k_{xk} is the in-plane thermal conductivity of the kth layer. The solution again involves solving Eq. 6.19 with different expressions for the matrices. For convenience, all the relations are summarized below.

$$a_{ij} = \delta_{i,j}(1 + \exp\left[+2l_m^{(i)}h\right]) +$$
$$\int_0^\infty (-1)^{i+j+1}\left(\frac{1+R_1}{1-R_1}\right)\frac{2k_m l_m^{(j)}(2-\delta_{0,j})(1-\exp\left[+2l_m^{(j)}h\right])\lambda_d^2 \sin^2 \lambda_d b}{\pi k_{y1}l_1 b[(\lambda_d)^2 - (\lambda_m^{(i)})^2][(\lambda_d)^2 - (\lambda_m^{(j)})^2]}d\lambda_d \quad (6.22)$$

$$q_i = -\delta_{0,i}\frac{\dot{q}'''}{k_m q_m^2} \quad (6.23)$$

$$R_k = \left(\frac{(z_k - z_{k+1}) + R_{k+1}(z_k + z_{k+1})\exp\left[2l_{k+1}d_k\right]}{(z_k + z_{k+1})\exp\left[2l_k d_k\right] + R_{k+1}(z_k - z_{k+1})\exp\left[2l_{k+1}d_k\right]}\right)$$

$$R_N = 0; \quad l_k = \sqrt{k_{xyk}\lambda_d^2 + q_k^2}; \quad q_k = \sqrt{\frac{i\omega_h}{\alpha_k}};$$

$$k_{xyk} = \frac{k_{xk}}{k_{yk}}; \quad \alpha_k = \frac{k_{yk}}{(\rho c_P)_k}; \quad z_k = k_{yk}l_k; \quad k = 1, ..., N \tag{6.24}$$

Once Eq. 6.19 is solved with the above expressions for the matrix elements, the average complex temperature amplitude is given by

$$\Delta T_{avg} = C_o(1 + \exp[+2q_m h]) + \frac{\dot{q}'''}{k_m q_m^2} \tag{6.25}$$

6.3 Results and Discussion

The semi-analytical solution described in the previous section is solved in MATLAB. The simulations were performed for a 300 nm thick and 6 μm wide Aluminum metal line. The thermal conductivity and heat capacity of the metal line was fixed at 235 W/mK and 2.43×10^6 respectively. The heat capacity of the underlying film was fixed at 1.626×10^6 (corresponding to silicon dioxide), and the thermal conductivity was allowed to vary. Figure 6.4 compares the predictions made by earlier and present 3ω solutions. It is clear that the error is significant when the underlying film thermal conductivity k_f is low. Earlier 3ω solutions always over-predict the average temperature rise. A non-zero thermal conductivity of the metal line smooths out temperature variation in the metal line and results in a lower average temperature. This effect mainly depends on the lateral thermal conductivity (in-plane) of the metal line and film. In Cahill's original paper [15], the 3ω technique was applied only to semi-infinite substrates. An approximate expression was obtained for the real part of average temperature amplitude when $\sqrt{\omega_h b^2/\alpha_d} \ll 1$. Thermal conductivity can then be directly calculated using the slope between real part of temperature amplitude and $\ln\omega$. Figure 6.5 plots this slope for three different solutions. The solution that is corrected for metal heat capacity was derived by Borca-Tascuic et al. [11]. This figure shows that metal thermal conduction only adds a frequency independent correction to the real part of temperature amplitude for small $\sqrt{\omega_h b^2/\alpha_d}$. It can thus
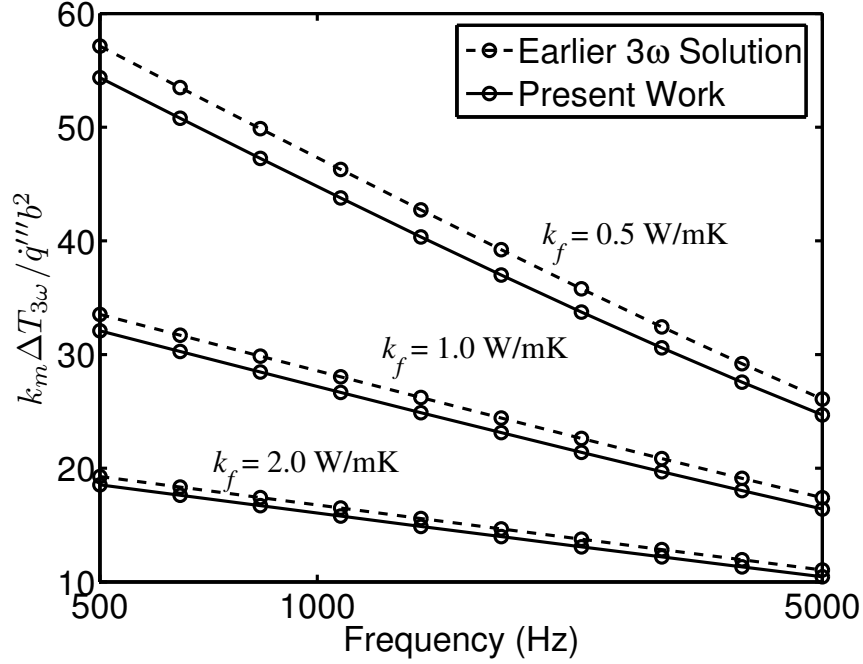
Figure 6.4: Comparison of temperature amplitude predictions between earlier and present 3ω solutions. The error is significant for low film thermal conductivity k_f.

be ignored when Cahill's original technique is used. For higher $\sqrt{\omega_h b^2/\alpha_d}$, the three solutions deviate, and when $\sqrt{\omega_h b^2/\alpha_d} \gg 1$, the heat capacity corrected and present work solution become coincident. This is due to the metal heat capacity domination at very large frequencies. The heat conduction is essentially one-dimensional at such frequencies. Effect of heat capacity was absent in Cahill's original solution.

From the foregoing discussion and results, it is clear that the effect of in-plane thermal conduction is important. Naturally, significant deviations should be expected when the 3ω method is used to measure anisotropy in the film thermal conductivity. A virtual experiment is performed to evaluate this effect. AC temperature rise as a function of frequency is obtained by solving the present solution for an isotropic film. These results are assumed to be the experimental results, and the earlier 3ω solution for an anisotropic film is used to fit to these measurements. Earlier solution is the one corrected for metal heat capacity that was derived by Borca-Tascuic et al. [11].
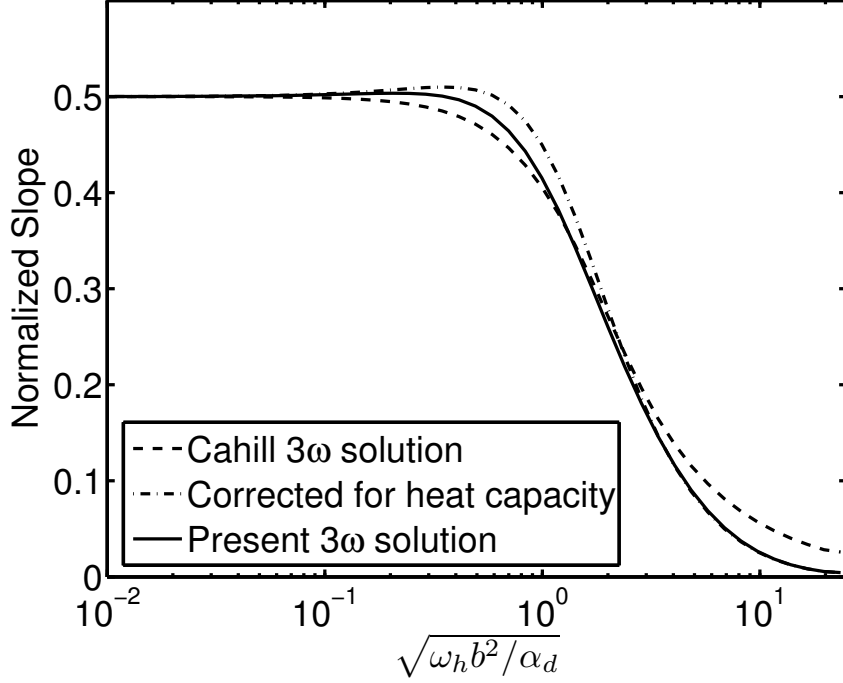
Figure 6.5: Comparison of temperature amplitude predictions between earlier and present 3ω solutions. The error is significant for low film thermal conductivity k_f.

Ideally, one should obtain $k_{xy} = 1$ after the fit. Figure 6.6 plots the obtained k_{xy} after the fit. Earlier 3ω solutions can falsely predict anisotropy even for a perfectly isotropic film. The error is more pronounced for low thermal conductivity films. Earlier solution can predict a k_x of 0.15 W/mK when in reality it is only 0.1 W/mK.

Figure 6.7 shows the error when a real anisotropic film is considered. Cross-plane thermal conductivity k_y is fixed at 0.5 W/mK for all the cases. As in the previous case, virtual experiments are performed and the earlier 3ω solution is used to obtain an estimate for anisotropy ratio. It is clear that earlier 3ω solution fails significantly at low in-plane thermal conductivities.
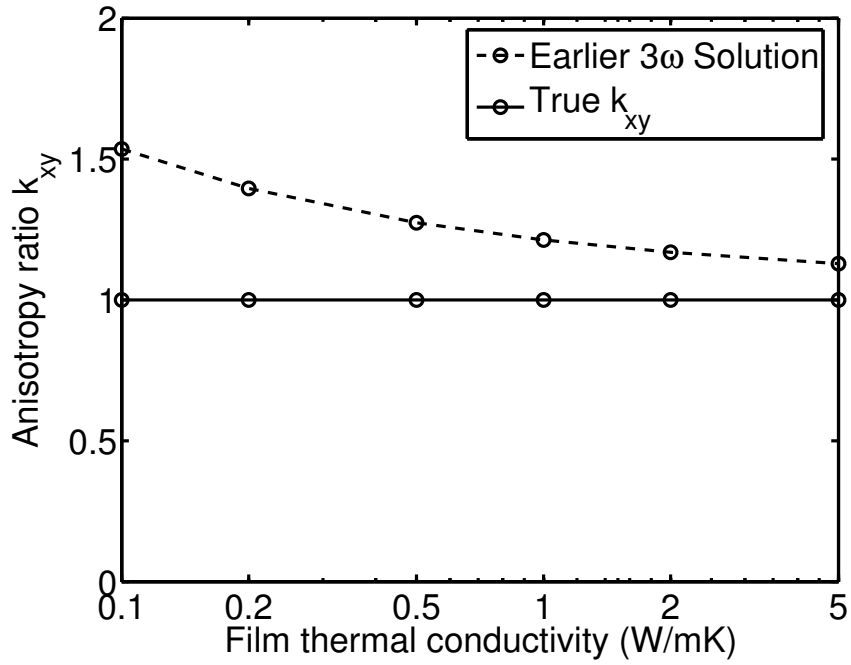
Figure 6.6: False anisotropy ratio predicted by earlier 3ω solution as the thermal conductivity of a perfectly isotropic film is varied.
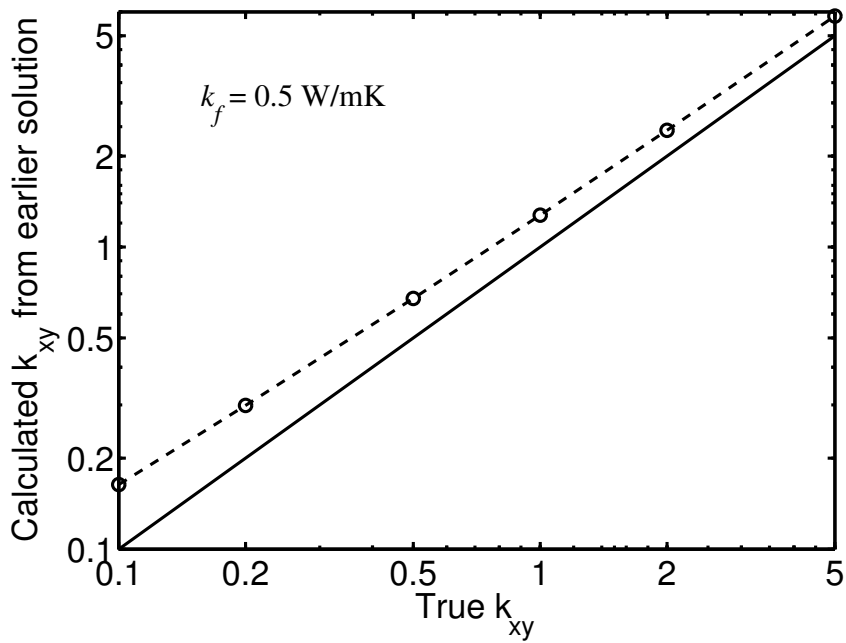
Figure 6.7: Comparison of original and earlier 3ω solution predictions for anisotropy ratio.

CHAPTER VII

CONCLUSION

This dissertation addresses the task of predicting temperature rise in an on-chip inter-connect stack. A detailed temperature map within the microprocessor interconnect stack is necessary to predict signal time delay and mean time to failure due to elec-tromigration. Thermal predictions become difficult due to complexity of the stack. Number of features is on the order of a billion, and as the dimensions shrink to below 100 nm range, electron size effects become important. This chapter discusses several conclusions that can be drawn from different analytical, numerical and experimental techniques developed as part of this work. Future directions are also discussed.

A finite element based compact thermal modeling methodology was developed to obtain temperature rise in interconnects due to Joule heating. This approach uses continuum based thermal modeling based on the Fourier's Law of heat conduction. Interconnects are made of metal and are highly conductive. Temperature drop across their cross-section can thus be ignored. The compact elements in this work include both metal and dielectric regions. This reduces the number of nodes, and results in shorter computational times and smaller memory requirements. In two-dimensional case studies performed on uniformly spaced interconnects, compact elements per-formed better than standard finite elements for the same number of elements. The error in compact model predictions was within 5 – 10 % of the detailed simulations. In some cases, an order of magnitude performance improvement was obtained us-ing compact elements. Similar errors were obtained in the case of three dimensional interconnects terminated by vias. In this structure, thermal conduction along the in-terconnect length is significant, and is included in the compact element. The method

was also applied on a long serpentine chain of about 500 interconnects and vias. The predictions compared well with experimentally measured temperature rise at several current densities.

The compact model case studies suggest that this technique can be valuable for interconnect temperature rise predictions. This approach requires thermal properties of metal and dielectric, and the variation of heat generation within the interconnect net. For macroscopic dimensions, thermal properties can be prescribed as bulk values and pose no difficulty for the compact modeling. Electron size effects become important when the dimensions are comparable to the mean free path. For long straight interconnects, an effective thermal conductivity can be defined for heat conduction along the interconnect. This can enter seamlessly within the compact model since only thermal conductivity along the interconnect is retained. For more complex structures that involve a cross-section change, effective thermal conductance can be defined between two locations. Such a model was developed for a constriction in a thin metallic film with perfectly specular scattering by solving the Boltzmann Transport Equation (BTE). This effective conductance can then be easily used in the compact modeling framework. Heat generation within the metal lines is determined mainly by the electrical properties, dimensions, and operating conditions. Detailed electrical circuit analysis is necessary to calculate average current density within the interconnects. Compact model can then use the heat generation obtained through such analysis.

A numerical solution of the BTE was developed to simulate electron transport in complex interconnect structures. A path integral formulation was used to solve the BTE deterministically. Several approximations were made to simplify the problem. These approximations, such as the free electron model, relaxation time approximation, and linear response, are justified for metals at low electric fields. A self-consistent solution of the BTE and Poission's equation for electric potential is not necessary, as

the BTE is decoupled from the Poisson's equation.

A constriction in a thin metallic film was investigated using the above described technique. This structure closely approximates a via effect. Significant reductions in effective conductance result as the constriction sizes become comparable to or smaller than the mean free path. This reduction is observed even with perfectly specular surfaces, and thus will persist even with innovations in microfabrication to obtain atomically smooth surfaces. An important utility of these simulations was also pointed out. A short metallic bridge between wider metal lines can be approximated as a composition of a constriction and the metal bridge. Effective conductance of such a structure is easily calculated by adding the traditional ohmic resistance of the metal bridge to the constriction resistance. The error with such additions was within 3 % for the cases considered. This suggests that reduced models of vias can be obtained and used in large scale simulations involving interconnects and vias.

Thermal characterization of thin metallic films in the size effect regime was performed by an existing Atomic Force Microscope (AFM) based application called Scanning Joule Expansion Microscopy (SJEM). A novel technique to measure thermal conductivity of thin metallic films was developed using SJEM. This involves characterizing a constriction in the thin metal film for AC Joule heating and using numerical modeling in the frequency space. The thermal conductivities of 43 nm and 131 nm gold films measured using this technique, were found to be 82 W/mK and 162 W/mK respectively at the smallest frequency investigated. Thermal conductivities were similar at other frequencies. These measurements are close to Wiedemann-Franz Law predictions but are significantly smaller than the bulk value of 318 W/mK due to electron size effects.

The above described thermal conductivity measurement technique has several advantages. It does not require complex microfabrication to obtain free-standing metal structures necessary for conventional techniques. Electron size effect is highly

dependent on the interface between metal and dielectric. A free-standing structure completely alters this interface and naturally will lead to different electron scattering characteristics. In addition, due to high resolutions possible with SJEM ($\sim$ 10 nm), it can potentially be used for interconnects whose width is in the sub-100 nm range. Although the technique was demonstrated on metal films, any current carrying and heat generating material can be characterized through this technique. These include doped silicon or other semiconductors.

The low-k dielectrics being developed for next generation microprocessors have much lower thermal conductivity than the traditional TEOS (TetraEthylOrthoSilicate) oxide. The 3ω technique is very popular for their thermal conductivity measurements. In this work, a new semi-analytical solution was derived to incorporate metal heater thermal conduction, not accounted for in the existing 3ω solutions. It was found that this effect is highly important in anisotropy measurements. For films of low thermal conductivity ($\sim$ 0.1 W/mK), existing solutions can falsely predict anisotropy even in a perfectly isotropic thin film. In addition, for a truly anisotropic film, existing solutions can result in errors as high as 50 % in their anisotropy ratio.

7.1   Future work

Several important directions can further be explored to enable accurate and efficient thermal predictions in an on-chip interconnect stack. One such area is the multi-scale modeling that involves simultaneous solution of both nanoscale and macroscale. BTE simulations at the nanoscale should be coupled with macroscopic electron transport. Such a simulation may bring out new effects that cannot be captured by the reduced models.

The compact elements developed in the present work require the interconnect to be located on the corner of the element. Further techniques should be developed to remove this restriction and enable automatic mesh generation. A general element

containing arbitrary metallic and dielectric regions is an ideal problem to investigate. This further leads to upscaling techniques, where a smaller region is first modeled accurately by detailed finite elements and later embedded in the larger system by using empirical shape functions. Another important effect is metal-dielectric interface resistance. This contact resistance should be incorporated within the compact elements. The compact model can also be extended to solve for 3D architectures where there can be several active device layers.

Temperature rise in interconnect structure is a coupled electrothermal problem. Electric circuit design models can be integrated with the thermal models in the present work. Only a detailed circuit analysis can provide the average heat generation rates within the interconnects. These heat generation models should account for size and skin effects.

The experimental technique to measure thermal conductivity of interconnects should be applied on sub-100 nm wide interconnects. Another important application is on tantalum barrier films. These films are usually 5 to 10 nm thick and detailed simulations maybe necessary to design optimal test structures. It is also interesting to see how the technique performs when electron transport is dominated by hopping between the metal islands. Further investigations can also be performed on doped semiconductors.

REFERENCES

[1] ADAMS, V. H., JOSHI, Y. K., and BLACKBURN, D. L., "Application of compact model methodologies to natural convection cooling of an array of electronic packages in a low profile enclosure," in *Advances in Electronic Packaging, Pt. 2*, (New York), pp. 1967–1974, ASME, 1997.

[2] AJAMI, A. H., PEDRAM, M., and BANERJEE, K., "Effects of non-uniform substrate temperature on the clock signal integrity in high performance designs," in *Proceedings of the IEEE 2001 Custom Integrated Circuits Conference*, (San Diego, CA, USA), pp. 233–236, IEEE, 2001.

[3] ARX, M. V., PAUL, O., and BALTES, H., "Process-dependent thin-film thermal conductivities for thermal cmos mems," *Journal of Microelectromechanical Systems*, vol. 9, pp. 136–145, 2000.

[4] ASHCROFT, N. W. and MERMIN, N. D., *Solid State Physics*. Holt: Rinehart and Winston, 1 ed., 1976.

[5] BANERJEE, K., MEHROTRA, A., SARASWAT, K. C., GOODSON, K. E., and WONG, S. S., "Quantitative projections of reliability and performance for low-k/Cu interconnect systems," in *Proceedings of the 38th IEEE Annual International Reliability Physics Symposium (IRPS)*, (San Jose, CA, USA), pp. 354–358, IEEE, 2000.

[6] BAR-COHEN, A., ELPERIN, T., and ELIASI, R., "θ_{jc} characterization of chip packages – justification, limitations, and future," *IEEE Transactions on Components, Hybrid, and Manufacturing Technology*, vol. 12, pp. 724–731, 1989.

[7] BEENAKER, C. W. J. and HOUTEN, H. V., *Quantum Transport in Semiconductor Nanostructures*, vol. 44 of *Solid State Physics: Advances in Research and Applications*, p. 1. New York: Academic Press, 1991.

[8] BILOTTI, A. A., "Static temperature distribution in IC chips with isothermal heat sources," *IEEE Transactions on Electron Devices*, vol. ED-21, pp. 217–226, 1974.

[9] BLACK, J. R., "Electromigration failure modes in aluminum metallization for semiconductor devices," *IEEE Transactions on Electron Devices*, vol. 57, pp. 1587–1594, 1969.

[10] BOIKO, B. T., PUGACHEV, A. T., and BRATSYCHIN, V. M., "Method for the determination of the thermophysical properties of evaporated thin films," *Thin Solid Films*, vol. 17, pp. 157–161, 1973.

[11] Borca-Tasciuc, T., Kumar, A. R., and Chen, G., "Data reduction in 3ω method for thin-film thermal conductivity determination," *Review of Scientific Instruments*, vol. 72, pp. 2139–2147, 2001.

[12] Boughton, R. T. and Feng, Z., "Monte carlo simulation of the dc size effect in thin films," *International Journal of Modern Physics C*, vol. 6, pp. 223–232, 1995.

[13] Boyalakuntla, D. S. and Murthy, J. Y., "Hierarchical compact models for simulation of electronic chip packages," *IEEE Transactions on Components and Packaging Technologies*, vol. 25, pp. 192–203, 2002.

[14] Bulashenko, O. M., Kochelap, O. V., and Kochelap, V. A., "Size effect on current fluctuations in thin metal films: Monte carlo approach," *Physical Review B*, vol. 45, pp. 14308–14314, 1992.

[15] Cahill, D. G., "Thermal conductivity measurement from 30 to 750 K: the 3ω method," *Review of Scientific Instruments*, vol. 61, pp. 802–808, 1990.

[16] Carcia, P. F. and Suna, A., "Properties of Au/Pd thin film layered structures," *Journal of Applied Physics*, vol. 54, pp. 2000–2005, 1983.

[17] Casu, M. R., Graziano, M., Masera, G., Piccinini, G., and Zamboni, M., "Coupled electro-thermal modeling and optimization of clock networks," *Microelectronics Journal*, vol. 34, pp. 1175–1185, 2003.

[18] Chen, D., Li, E., Rosenbaum, E., and Kang, S.-M., "Interconnect thermal modeling for accurate simulation of circuit timing and reliability," *IEEE Transactions on Computer-Aided Design of Integrated Circuits and Systems*, vol. 19, pp. 197–205, 2000.

[19] Chen, F. and Gardner, D., "Influence of line dimensions on the resistance of cu interconnections," *IEEE Electron Device Letters*, vol. 19, pp. 508–510, 1998.

[20] Chiang, T.-Y., Banerjee, K., and Saraswat, K. C., "Thermal analysis of electromigration test structures," *IEEE Electron Device Letters*, vol. 23, pp. 31–33, 2002.

[21] Chopra, K. L., *Thin Film Phenomena*. New York: McGraw-Hill, 1 ed., 1969.

[22] Dean, J. A., *Lange's Handbook of Chemistry*. New York: McGraw-Hill, 15 ed., 1999.

[23] deJong, M. J. M., "Transition from sharvin to drude resistance in high–mobility wires," *Physical Review B*, vol. 49, pp. 7778–7781, 1994.

[24] Dimmich, R., "Electronic transport properties of metallic multi-layer films," *Journal of Physics F: Metal Physics*, vol. 15, pp. 2477–2487, 1985.

[25] DINGLE, R. B., "The electrical conductivity of thin wires," *Proceedings of the Royal Society of London, Series A, Mathematical and Physical Sciences*, vol. 201, pp. 545–560, 1950.

[26] FENN, M., AKUETEY, G., and DONOVAN, P. E., "Electrical resistivity of cu and nb thin films," *Journal of Physics: Condensed Matter*, vol. 10, pp. 1707–1720, 1998.

[27] FUCHS, K., "The conductivity of thin metallic films according to the electron theory of metals," *Proceedings of Cambridge Philosophical Society*, vol. 34, pp. 100–108, 1938.

[28] GIACOLETTO, L. J., "Frequency– and time–domain analysis of skin effects," *IEEE Transactions on Magnetics*, vol. 32, pp. 220–229, 1996.

[29] GOODSON, K. E., FLIK, M. I., SU, L. T., and ANTONIADIS, D. A., "Prediction and measurement of the thermal conductivity of amorphous dielectric layers," *ASME Journal of Heat Transfer*, vol. 117, pp. 574–581, 1994.

[30] GRIFFIN, A. J. J., BROTZEN, F. R., and LOOS, P. J., "The effective transverse thermal conductivity of amorphous Si_3N_4 thin films," *Journal of Applied Physics*, vol. 76, pp. 4007–4011, 1994.

[31] HATTA, I., SASUGA, Y., KATO, R., and MAESONO, A., "Thermal diffusivity measurement of thin films by means of an ac calorimetric method," *Review of Scientific Instruments*, vol. 56, pp. 1643–1647, 1985.

[32] HO, C. Y., POWELL, R. W., and LILEY, P. E., "Thermal conductivity of the elements: A comprehensive review," *Journal of Physical and Chemical Reference Data*, vol. 3, Suppl. No. 1, p. 796, 1974.

[33] HO, P. S. and KWOK, T., "Electromigration in metals," *Reports on Progress in Physics*, vol. 52, pp. 301–348, 1988.

[34] HUANG, W., STAN, M. R., SKADRON, K., SANKARANARAYANAN, K., GHOSH, S., and VELUSAMY, S., "Effects of non-uniform substrate temperature on the clock signal integrity in high performance designs," in *Proceedings of the 41st Design Automation Conference*, (San Diego, CA, USA), pp. 878–883, Association for Computing Machinery, Inc. (ACM), 2004.

[35] HUNTER, W. R., "Self-consistent solutions for allowed interconnect current density part I: Implications for technology evolution," *IEEE Transactions on Electron Devices*, vol. 44, pp. 304–309, 1997.

[36] IGETA, M., BANERJEE, K., WU, G., HU, C., and MAJUMDAR, A., "Thermal characteristics of submicron vias studied by scanning joule expansion microscopy," *IEEE Electron Device Letters*, vol. 21, pp. 224–226, 2000.

[37] ITRS, *International Roadmap for Semiconductors*. USA: ITRS Working Group, 2004. http://public.itrs.net/.

[38] JACKSON, J. D., *Classical Electrodynamics*. New York: Wiley, 3 ed., 1998.

[39] JACOBONI, C. and REGGIANI, L., "The monte carlo method for the solution of charge transport in semiconductors with applications to covalent materials," *Reviews of Modern Physics*, vol. 55, pp. 645–705, 1983.

[40] JACQUOT, A., LENOIR, B., DAUSCHER, A., STOLZER, M., and MEUSEL, J., "Numerical simulation of the 3ω for measuring the thermal conductivity," *Journal of Applied Physics*, vol. 91, pp. 4733–4738, 2002.

[41] JANSEN, A. G. M., GELDER, A. P. V., and WYDER, P., "Point-contact spectroscopy in metals," *Journal of Physics C: Solid State Physics*, vol. 13, pp. 6073–6118, 1980.

[42] JU, Y. S. and GOODSON, K. E., "Process-dependent thermal transport properties of silicon-dioxide films deposited using low-pressure chemical vapor deposition," *Journal of Applied Physics*, vol. 85, pp. 7130–7134, 1999.

[43] KAPUR, P., CHANDRA, G., MCVITTIE, J. P., and SARASWAT, K. C., "Technology and reliability constrained future copper interconnects part II: Performance implications," *IEEE Transactions on Electron Devices*, vol. 49, pp. 598–604, 2002.

[44] KAPUR, P., MCVITTIE, J. P., and SARASWAT, K. C., "Technology and reliability constrained future copper interconnects part I: Performance implications," *IEEE Transactions on Electron Devices*, vol. 49, pp. 590–597, 2002.

[45] KELEMEN, F., "Pulse method for the measurement of the thermal conductivity of thin films," *Thin Solid Films*, vol. 36, pp. 199–203, 1976.

[46] KEMP, T., SRINIVAS, T. A. S., FETTIG, R., and RUPPEL, W., "Measurement of thermal diffusivity of thin films and foils using a laser scanning microscope," *Review of Scientific Instruments*, vol. 66, pp. 176–181, 1995.

[47] KLINE, S. J. and MCCLINTOCK, F. A., "Describing uncertainties in single-sample experiments," *Mechanical Engineering*, vol. 75, pp. 3–8, 1953.

[48] KUMAR, S. and VRADIS, G. C., "Thermal conductivity of thin metallic films," *ASME Journal of Heat Transfer*, vol. 116, pp. 28–34, 1994.

[49] LANGER, G., HARTMANN, J., and REICHLING, M., "Thermal conductivity of thin metallic films measured by photothermal profile analysis," *Review of Scientific Instruments*, vol. 68, pp. 1510–1513, 1997.

[50] LIU, H.-D., ZHAO, Y.-P., RAMANATH, G., MURARKA, S. P., and WANG, G.-C., "Thickness dependent electrical resistivity of ultrathin (< 40 nm) Cu films," *Thin Solid Films*, vol. 384, pp. 151–156, 2001.

[51] Lu, L., Yi, W., and Zhang, D. L., "3ω method for specific heat and thermal conductivity measurements," *Review of Scientific Instruments*, vol. 72, pp. 2996–3003, 2001.

[52] Lu, X., Shen, W. Z., and Chu, J. H., "Size effect on the thermal conductivity of nanowires," *Journal of Applied Physics*, vol. 91, pp. 1542–1552, 2002.

[53] Lugli, P. and Ferry, D. K., "Degeneracy in the ensemble monte carlo method for high-field transport in semiconductors," *IEEE Transactions on Electron Devices*, vol. ED–32, pp. 2431–2437, 1985.

[54] Luthi, B. and Wyder, P., "A monte-carlo calculation for a size effect problem," *Helvetica Physica Acta*, vol. 33, pp. 667–674, 1960.

[55] MacDonald, D. K. C. and Sarginson, K., "Size effect variation of the electrical conductivity of metals," *Proceedings of the Royal Society of London, Series A, Mathematical and Physical Sciences*, vol. 203, pp. 223–240, 1950.

[56] Majumdar, A., "Scanning thermal microscopy," *Annual Reviews in Materials Science*, vol. 29, pp. 505–585, 1999.

[57] Mase, G. T. and Mase, G. E., *Continuum Mechanics for Engineers*. Boca Raton, FL: CRC Press, 2 ed., 1999.

[58] Maxwell, J. C., *A Treatise on Electricity and Magnetism*. New York: Dover Press, 1 ed., 1891.

[59] Mayadas, A. F. and Shatzkes, M., "Electrical-resistivity model for polycrystalline films: the case of arbitrary reflection at external surfaces," *Physical Review B*, vol. 1, pp. 1382–1389, 1970.

[60] Namba, Y., "Resistivity and temperature coefficient of thin metal films with rough surface," *Japanese Journal of Applied Physics*, vol. 9, pp. 1326–1329, 1970.

[61] Nath, P. and Chopra, K. L., "Experimental determination of the thermal conductivity of thin films," *Thin Solid Films*, vol. 18, pp. 29–37, 1973.

[62] Nath, P. and Chopra, K. L., "Thermal conductivity of copper films," *Thin Solid Films*, vol. 20, pp. 53–62, 1974.

[63] Ney, M. M., "Striction and skin effects on the internal impedance value of flat conductors," *IEEE Transactions on Electromagnetic Compatibility*, vol. 33, pp. 321–327, 1991.

[64] Nikolic, B. and Allen, P. B., "Electron transport through a circular constriction," *Physical Review B*, vol. 60, pp. 3963–3969, 1999.

[65] PICHARD, C. R., OUARBYA, L., BOUHALA, Z., and TOSSER, A. J., "General expressions for the wiedemann-franz law in metallic layers," *Journal of Materials Science Letters*, vol. 3, pp. 725–727, 1984.

[66] PIPPARD, A. B., "The surface impedance of superconductors and normal metals at high frequencies. II. The anomalous skin effect in normal metals," *Proceedings of the Royal Society of London. Series A*, vol. 191, pp. 385–399, 1947.

[67] POMPE, G. and SCHMIDT, K., "Vapor-deposited lead films and their transport characteristics at low temperatures," *Physica Status Solidi. A*, vol. 31, pp. 37–46, 1975.

[68] PRICE, P. J., *Monte Carlo Calculation of Electron Transport in Solids*, vol. 14 of *Semiconductors and Semimetals*, pp. 249–308. New York: Academic Press, 1979.

[69] RAMAKRISHNA, K., GALL, M., JUSTISON, P., and KAWASAKI, H., "Prediction of maximum allowed rms currents for electromigration design guidelines," in *Proceedings of 7th International Workshop on Stress-Induced Phenomena in Metallization* (HO, P. S., BAKER, S. P., NAKAMURA, T., and VOLKERT, C. A., eds.), vol. 741, (Melville, NY), pp. 156–164, American Institute of Physics, 2004. AIP Conference Proceedings.

[70] REISS, G., VANCEA, J., and HOFFMANN, H., "Grain-boundary resistance in polycrystalline metals," *Physical Review Letters*, vol. 56, pp. 2100–2103, 1986.

[71] ROMANO, L. and DALLACASA, V., "Monte carlo simulation in fermi systems: Transport parameters," *Journal of Physics: Condensed Matter*, vol. 2, pp. 4717–4725, 1990.

[72] ROSTEN, H. I., LASANCE, C. J. M., and PARRY, J. D., "The world of thermal characterization according to DELPHI - part I: Background to DELPHI," *IEEE Transactions on Components Packaging and Manufacturing Technology Part A*, vol. 20, pp. 384–391, 1997.

[73] RUDD, R. E. and BROUGHTON, J. Q., "Concurrent coupling of length scales in solid state systems," *Physica Status Solidi. B*, vol. 217, pp. 251–291, 2000.

[74] SABRY, M.-N., "Higher order compact thermal models," in *Proceedings of the 10th International Workshop on Thermal Investigations of ICs And Systems (THERMINIC)*, (Sophia Antipolis, Cte d'Azur, France), pp. 273–280, TIMA Laboratory, 2004.

[75] SARVARI, R. and MEINDL, J. D., "On the study of anomalous skin effect for GSI interconnections," in *Proceedings of the 2003 IEEE International Interconnect Technology Conference*, (San Francisco, USA), pp. 42–44, IEEE, Piscataway, N.J., 2003.

[76] SCHAFFT, H. A., "Thermal analysis of electromigration test structures," *IEEE Transactions on Electron Devices*, vol. ED-34, pp. 664–672, 1987.

[77] SEGERLIND, L. J., *Applied Finite Element Analysis*. New York: Wiley, 2nd ed., 1984.

[78] SHARVIN, Y. V., "A possible method for studying fermi surfaces," *Soviet Physics JETP*, vol. 21, pp. 655–656, 1965.

[79] SHEN, Y.-L., "Analysis of Joule heating in multilevel interconnects," *Journal of Vacuum Science and Technology B*, vol. 17, pp. 2115–2121, 1999.

[80] SHOJAEI-ZADEH, S., ZHANG, S., LIU, W., YANG, Y., SADEGHIPOUR, S. M., and ASHEGHI, M., "Thermal characterization of thin film cu interconnects for the next generation of microelectronic devices," in *Proceedings of 2004 Inter Society Conference on Thermal Phenomena – ITHERM*, (Las Vegas, NV, USA), pp. 575–583, IEEE, Piscataway, N.J., 2004.

[81] SOFFER, S. B., "Statistical model for the size effect in electrical conduction," *Journal of Applied Physics*, vol. 38, pp. 1710–1715, 1967.

[82] SONDHEIMER, E. H., "The mean free path of electrons in metals," *Advances in Physics*, vol. 1, pp. 1–42, 1952.

[83] STAN, M. R., SKADRON, K., BARCELLA, M., HUANG, W., SANKARA-NARAYANAN, K., and VELUSAMY, S., "Hotspot: A dynamic compact thermal model at the processor-architecture level," *Microelectronics Journal*, vol. 34, pp. 1153–1165, 2003.

[84] STEWART, D. and NORRIS, P. M., "Size effects on the thermal conductivity of thin metallic wires: Microscale implications," *Microscale Thermophysical Engineering*, vol. 4, pp. 89–101, 2000.

[85] STREITER, R., WOLF, H., ZHU, Z., XIAO, X., and GESSNER, T., "Application of combined thermal and electrical simulation for optimization of deep submicron interconnection systems," *Microelectronic Engineering*, vol. 60, pp. 39–49, 2002.

[86] SURI, R., THAKOOR, A. P., and CHOPRA, K. L., "Electron transport properties of thin copper films. i.," *Journal of Applied Physics*, vol. 46, pp. 2574–2582, 1975.

[87] TENG, C.-C., CHENG, Y.-K., ROSENBAUM, E., and KANG, S.-M., "iTEM: A temperature-dependent electromigration reliability diagnosis tool," *IEEE Transactions on Computer-Aided Design of Integrated Circuits and Systems*, vol. 16, pp. 882–893, 1997.

[88] TREICHEL, H., "Low dielectric constant materials," *Journal of Electronic Materials*, vol. 30, pp. 290–298, 2001.

[89] VANCEA, J., HOFFMANN, H., and KASTNER, K., "Mean free path and effective density of conduction electrons in polycrystalline metal films," *Thin Solid Films*, vol. 121, pp. 201–216, 1984.

[90] VARESI, J. and MAJUMDAR, A., "Scanning joule expansion microscopy at nanometer scales," *Applied Physics Letters*, vol. 72, pp. 37–39, 1998.

[91] VOLKLEIN, F. and BALTES, H., "A microstructure for measurement of thermal conductivity of polysilicon thin films," *Journal of Microelectromechanical Systems*, vol. 1, pp. 193–196, 1992.

[92] VOLKLEIN, F. and KESSLER, E., "A method for the measurement of thermal conductivity, thermal diffusivity, and other transport coefficients of thin films," *Physica Status Solidi. A*, vol. 81, pp. 585–596, 1984.

[93] VOLKLEIN, F. and STARZ, T., "Thermal conductivity of thin films – experimental methods and theoretical interpretation," in *Proceedings of XVI International Conference on Thermoelectrics – XVI ICT '97*, (Dresden, Germany), pp. 711–718, IEEE, Piscataway, N.J., 1997.

[94] WARKUSZ, F., "Temperature effects in thin metal films," *Thin Solid Films*, vol. 148, pp. 343–353, 1987.

[95] WEXLER, G., "The size effect and the non-local boltzmann transport equation in orifice and disk geometry," *Proceedings of the Physical Society of London*, vol. 89, pp. 927–941, 1966.

[96] YAMANE, T., KATAYAMA, S.-I., and TODOKI, M., "Analysis of ac temperature wave during the measurement of thermal diffusivity of two-layered platelike samples," *Journal of Applied Physics*, vol. 80, pp. 2019–2026, 1996.

[97] YAMANE, T., MORI, Y., KATAYAMA, S.-I., and TODOKI, M., "Measurement of thermal diffusivities of thin metallic films using the ac calorimetric method," *Journal of Applied Physics*, vol. 82, pp. 1153–1156, 1997.

[98] YANG, Y. and ASHEGHI, M., "A novel technique for in–plane thermal conductivity measurements of electrically conductive interconnects and nanostructures," in *Proceedings of 2004 Inter Society Conference on Thermal Phenomena – ITHERM*, (Las Vegas, NV, USA), pp. 564–569, IEEE, Piscataway, N.J., 2004.

[99] YEH, E. C. C. and TU, K. N., "Numerical simulation of current crowding phenomena and their effects on electromigration in very large scale integration interconnects," *Journal of Applied Physics*, vol. 88, pp. 5680–5686, 2000.

[100] YOVANOVICH, M. M., CULHAM, J. R., and TEERTSTRA, P., "Hierarchical compact models for simulation of electronic chip packages," *IEEE Transactions on Components, Packaging and Manufacturing Technology, Part A*, vol. 21, pp. 168–176, 1998.

[101] ZHANG, X., XIE, H., FUJII, M., AGO, H., TAKAHASHI, K., IKUTA, T., ABE, H., and SHIMIZU, T., "Thermal and electrical conductivity of a suspended platinum nanofilm," *Applied Physics Letters*, vol. 86, pp. 171912 (1–3), 2005.

[102] ZIMAN, J. M., *Electrons and Phonons*. New York: Oxford University Press, 1 ed., 1960.

VITA

Siva P. Gurrum was born in 1978 in Proddatur, Andhra Pradesh, India. He received his B. Tech. degree in Mechanical Engineering from Indian Institute of Technology Madras, India, in 1999 and M. S. degree in Mechanical Engineering from University of Maryland, College Park, MD, in 2001. His doctoral research is concentrated on thermal transport in nanoscale metallic interconnects. Other interests include electronics cooling, phase change, computational heat transfer and fluid flow and quantum effects in energy transport.